Proteomics-based metabolic modelling reveals that fatty acid oxidation controls endothelial cell permeability.

Patella F; Schug ZT; Persi E; Neilson LJ; Erami Z; Avanzato D; Maione F; Hernandez-Fernaud JR; Mackay G; Zheng L; Reid S; Frezza C; Giraudo E; Fiorio Pla A; Anderson K; Ruppin E; Gottlieb E; Zanivan S..
Proteomics-based metabolic modelling reveals that fatty acid oxidation controls endothelial cell permeability.. MOLECULAR & CELLULAR PROTEOMICS. 14 (3) pp: 621-634.
DOI: 10.1074/mcp.M114.045575

Patella F; Schug ZT; Persi E; Neilson LJ; Erami Z; Avanzato D; Maione F; Hernandez-Fernaud JR; Mackay G; Zheng L; Reid S; Frezza C; Giraudo E; Fiorio Pla A; Anderson K; Ruppin E; Gottlieb E; Zanivan S.

Proteomics-based metabolic modelling reveals that fatty acid oxidation controls endothelial cell permeability.

MOLECULAR & CELLULAR PROTEOMICS

Vol.14 fascicolo 3

2015

pag. 621-634

DOI: 10.1074/mcp.M114.045575

Proteomics-based metabolic modelling reveals that fatty acid oxidation controls endothelial cell permeability

Francesca Patella[1], Zachary T Schug[2], Erez Persi[3,4], Lisa J Neilson[1], Zahra Erami[5], Daniele Avanzato[6], Federica Maione[7,8], Juan R Hernandez-Fernaud[1], Gillian Mackay[2], Liang Zheng[2], Steven Reid[1], Christian Frezza[9], Enrico Giraudo[7,8], Alessandra Fiorio Pla[6], Kurt Anderson[5], Eytan Ruppin[3,10], Eyal Gottlieb[2] and Sara Zanivan[1]

[1]Vascular Proteomics Lab, [2]Apoptosis and Tumour Metabolism Lab, [5]Tumour Cell Migration Lab, Cancer Research UK Beatson Institute, Switchback Road, G61 1BD, Glasgow, UK

[3]The Blavatnik School of Computer Science, Tel Aviv University, 69978 Tel Aviv, Israel

[4]School of Physics and Astronomy, Tel Aviv University, 69978 Tel Aviv, Israel

[6]Department of Life Sciences and Systems Biology, University of Torino, Via Accademia Albertina 13, 10123 Torino, Italy

[7] Laboratory of Transgenic Mouse Models, Candiolo Cancer Institute – FPO, IRCCS, Str prov 142 Km 3.95, 10060, Candiolo, Torino, Italy

[8] Department of Science and Drug Technology, University of Torino, School of Medicine, Via P. Giuria, 9 - 10125 Torino, Italy

[9] MRC Cancer Unit, Cambridge Biomedical Campus, University of Cambridge, Hutchison/MRC Research Centre, Box 197, CB2 0XZ, Cambridge, UK

[10]Sackler School of Medicine, and Department of Molecular Microbiology and Biotechnology, Faculty of Life Sciences, Tel-Aviv University, 69978 Tel Aviv, Israel

Corresponding Author:

Sara Zanivan, PhD

Switchback Road

Glasgow G61 1BD, UK

Tel: +44(0)141 330 3971

Email: s.zanivan@beatson.gla.ac.uk

Running Title: FAO maintains endothelial permeability

Abbreviations:

EC endothelial cell

FAO fatty acid oxidation

TCAc tricarboxylic acid cycle

FA fatty acid

iMAT integrative metabolic analysis tool

GSMM genome-scale metabolic network model

SILAC stable-isotope labeling with amino acids in cell culture

HUVEC human umbilical vein endothelial cells

ECM extracellular matrix

TEER trans-endothelial electrical resistance

DCA dichloroacetate

VEGF vascular endothelial growth factor

Summary

Endothelial cells (ECs) play a key role to maintain the functionality of blood vessels. Altered EC permeability causes severe impairment in vessel stability and is a hallmark of pathologies such as cancer and thrombosis. Integrating label-free quantitative proteomics data into genome-wide metabolic modeling, we built up a model which predicts the metabolic fluxes in ECs when cultured on a tridimensional matrix and organize into a vascular-like network. We discovered how fatty acid oxidation (FAO) increases when ECs are assembled into a fully formed network that can be disrupted by inhibiting CPT1A, the FAO rate-limiting enzyme. Acute CPT1A inhibition reduces cellular ATP levels and oxygen consumption, which are restored by replenishing the tricarboxylic acid cycle (TCAc). Remarkably, global phosphoproteomic changes measured upon acute CPT1A inhibition pinpointed altered calcium signaling. Indeed, CPT1A inhibition increases intracellular calcium oscillations. Finally, inhibiting CPT1A induces hyperpermeability in-vitro and leakage of blood vessel in-vivo, which were restored blocking calcium influx or replenishing the TCAc. FAO emerges as central regulator of endothelial functions and blood vessel stability and druggable pathway to control pathological vascular permeability.

Introduction

Endothelial cells (ECs) line the inner layer of the blood vessel wall and constitute a barrier between blood and surrounding tissue. As such, a tight regulation of EC permeability is crucial to maintain vessel functionality and avoid excessive extravasation of fluid and plasma proteins [1]. Increased endothelial permeability is typical in inflammatory states and a hallmark of diseases such thrombosis, atherosclerosis and cancer [2, 3]. Because of their unique localization, ECs are constantly exposed to oxygen and nutrients which fuel cell metabolism and whose levels vary in physiological and pathological conditions. Yet, how cell metabolism regulates endothelial permeability remains incompletely understood.

Previous studies have reported that EC cultures use glucose as predominant source of energy by producing lactate through glycolysis. However, also fatty acids and glutamine contribute to ATP and metabolic intermediate production [4-7]. Recent in-vivo studies have shown that glycolysis is necessary for EC proliferation and motility in physiological and pathological angiogenesis [4, 8]. Moreover the peroxisome proliferator-activated receptor gamma coactivator 1-α, which can activate oxidative phosphorylation, blocks EC sprouting in diabetes [9]. The intriguing information emerging from these studies is that key metabolic pathways, such as glycolysis and oxidative phosphorylation in the mitochondria, play an important role in ECs and that they are actively involved in the regulation of key cell functions.

Mitochondrial fatty acid oxidation (FAO) is the process that converts fatty acids (FAs) into acetyl-CoA, which fuels the tricarboxylic acid cycle (TCAc) and generates reducing factors for producing ATP via oxidative phosphorylation. Cells can incorporate FAs from the culture media or can generate FAs from the hydrolysis of triglycerides or through de novo synthesis. FAs, then, can access the mitochondria according to their length; while short and medium-chain FAs (up to 12 carbon atoms) diffuse through the mitochondrial membrane, long-chain FAs (with 13-21 carbon atoms) are actively transported by the carnitine O-palmitoyl transferase (CPT) proteins, which are rate limiting enzymes for this pathway [10]. Previous work suggested that FAO is poorly utilized by EC cultures [4], however, under certain stress conditions such as glucose deprivation, FAO becomes a major source of energy [7]. While it is striking to note how cells can adapt and remodel their metabolism, the role of key FAO enzymes in the control of EC functions is still largely unclear.

Due to the complexity of the cell metabolome, global-scale metabolomic studies for in depth and quantitative analysis of metabolic fluxes are still challenging and computational models have provided invaluable help to better understand cell metabolism. Among them, the integrative metabolic analysis tool (iMAT), which integrates gene expression data with genome-scale metabolic network model (GSMM), has been successfully used to predict enzyme metabolic flux in several model systems and diseases [11, 12]. Since gene expression and protein levels do not always correlate, and because enzymes levels do not necessarily reflect their enzymatic activity or the flux of the reaction that they are involved in, iMAT uses expression data as cue for the likelihood, but not final determinant, of enzyme activity. Modern mass spectrometry (MS) technology and robust approaches for protein quantification, such as stable-isotope labeling with amino acids in cell culture (SILAC) [13] and advanced label-free algorithms [14], allow global comparative proteomic analysis and accurate measurements of protein and post-translational modification levels [15]. We reasoned that the integration of quantitative MS-proteomic data into GSMM could contribute to the study of cell metabolism. Moreover, metabolic changes trigger activation of protein kinases [16, 17] to rapidly remodel the intracellular signaling and enable cells to adapt to these sudden alterations. Protein phosphorylation therefore plays an important role in regulating cell response to metabolic alteration and may hide information on cellular pathways and functions controlled by specific metabolic activities. MS-based proteomic approaches therefore offer an additional opportunity to investigate in an unbiased manner the interplay between cell metabolism and cell function [18].

We have previously shown [19] that when human primary ECs are cultured for one day on the three dimensional matrix matrigel and assemble into a complex network, a simplified model which recapitulates some aspects of vascular network assembly in-vivo [20] the levels of metabolic enzymes are profoundly regulated. This result suggested an interplay between cell metabolism and EC behavior. Here we investigate further this aspect. Integrating label-free quantitative MS-proteomics, predictive metabolic modeling and metabolomics we discovered increased FAO when ECs are assembled into a fully formed network. Moreover, by inhibiting CPT1 pharmacologically, we elucidated that FAO is a central regulator of EC permeability in-vitro and blood vessel stability in-vivo. Thus proteomics significantly contributes to the study of cell metabolism and here we identified FAO as a promising target for therapeutic intervention for the control of pathological vascular permeability.

Experimental Procedures

Cells, reagents and treatments

Human umbilical vein endothelial cells (HUVECs) isolated from 2-5 umbilical cords were pooled and cultured in EGM-2 (Lonza, Basel, Switzerland). For the SILAC labelling, cells were grown for 3 passages (P) in custom EGM-2 without arginine and lysine (Lonza) supplemented with L-arginine and L-lysine (SILAC light) (Sigma-Aldrich, St. Louis, MO, USA), $^{13}C_6$ L-arginine and D_4 L-lysine (SILAC medium) or $^{13}C_6{}^{15}N_4$ L-arginine (SILAC heavy) and $^{13}C_6{}^{15}N_2$ L-lysine (heavy lysine) (Cambridge Isotope Laboratories, Tewksbury, MA, USA). BOECs were kindly provided by Dr. Maartje van den Biggelaar and cultured in EGM-2 medium 10% FBS. Cells were used between P2 and P6.

If not otherwise stated, after 2 h etomoxir treatment (15µg/ml) cells were treated or not with pyruvate (500µM) for 30 min followed by dichloroacetate (5mM) for 30 min before cells were used in experiments.

Etomoxir, oxfenicine, dichloroacetate, pyruvate, thrombin, VEGF and mouse anti-vinculin antibody were from Sigma-Aldrich; anti-CPT1A antibody (15184-1-AP) was from Protein Tech group (Chicago, IL, USA); anti-β-tubulin was from Santa Cruz Biotechnology (Dallas, TX, USA), anti-phospho ACACA was from Cell Signaling (Danvers, MA, USA); anti-mouse IRDye 700CW and anti-rabbit IRDye 800CW used for western blot were from LI-COR Biosciences (Lincoln, NE, USA). Matrigel and Cell recovery solution were from BD biosciences (Franklin Lakes, NJ, USA).

Matrigel assay

HUVECs were seeded and cultured on solidified Matrigel in EGM-2 medium with the indicated stimuli and harvested for MS analysis using Cell recovery solution according to manufacturer's instructions and as previously described [19]. Pictures were taken with Axiovert microscope and the tubule length measured with ImageJ software.

Sample preparation for proteomic analysis

HUVECs were lysed in 2% SDS, 100mM Tris-HCl pH 7.4 buffer.

Proteome Matrigel: Proteins were precipitated and solubilized in 8M urea, 75mM NaCl and 50mM TrisHCl. After reduction with dithiothreitol and alkylation with iodoacetamide, proteins were digested with trypsin. *Proteome etomoxir*: Light, medium and heavy SILAC-labeled cell lysates (~70 µg/sample) were mixed in equal amount, trypsin digested by filter-aided sample preparation method and 50 µg of peptides fractionated into six fractions using on-tip strong anion exchange chromatography [21].

Phosphoproteome: Light, medium and heavy SILAC-labeled cell lysates (~3 mg/sample) were mixed in equal amount, digested by filter-aided sample preparation method [22] and enriched for phosphorylated peptides using strong cation exchange chromatography followed by titanium dioxide enrichment [23] for phosphorylated peptides as previously described [24].

Digested peptides were de-salted with Empore-C_{18} StageTips [25], eluted in 80% acetonitrile (ACN), 0.5% acetic acid and stored at -80°C until MS analysis.

Proteomic MS analysis

Tryptic peptides were separated on 20 cm fused silica emitter (New Objective, Woburn, MA, USA) packed in-house with the reverse phase ReproSil-Pur C_{18}-AQ, 1.9 µm resin (Dr. Maisch, GmbH, Ammerbuch-Entringen, Germany) and analyzed on a LTQ-Orbitrap Elite (Thermo Fisher Scientific) coupled on-line with a nano-HPLC (Easy nLC, Thermo Fisher Scientific).

Proteome Matrigel: for each sample, ~2µg of digested peptides were eluted from reverse phase column with a flow of 200 nl/min in 190 min gradient, from 5% to 30% ACN in 0.5% acetic acid. For each time point three replicates were performed and each replicate was run at the MS twice.

Proteome etomoxir: for each fraction, half of the peptides were loaded onto reverse phase column and eluted with a flow of 200 in 190 min gradient, from 5% to 30% ACN in 0.5% acetic acid. Triplicate experiments were performed swapping SILAC labeling conditions.

Phosphoproteome: for each experiment, 10 fractions enriched for phosphorylated peptides were analyzed at the MS. Two third of each sample was loaded onto reverse phase column and eluted with a flow of 200

nl/min in 90 min gradient, from 5% to 30% ACN in 0.5% acetic acid. The remaining 1/3 was pooled into two fractions which were analyzed at the MS. Triplicate experiments were performed swapping SILAC labeling conditions.

MS spectra were acquired in the Orbitrap analyzer at a resolution of 120000 at 400 m/z, and a target value of 10^6 charges. High collision dissociation fragmentation of the 10 most intense ions was performed using a target value of 40000 charges and acquired in the Orbitrap at resolution 15000 at 400 m/z. Data were acquired with Xcalibur software. MS data were processed using the MaxQuant software [26] and searched with Andromeda search engine [27] against the human UniProt database (release-2012 01, 81,213 entries). An initial maximal mass deviation of 7 ppm and 20 ppm was required to search for precursor and fragment ions, respectively. Trypsin with full enzyme specificity and peptides with a minimum length of 7 amino acids were selected. Two missed cleavages were allowed. Oxidation (Met) and N-acetylation were set as variable modifications, as well as phospho(STY) for the phosphoproteome analysis, while Carbamidomethylation (Cys) as fixed modification. False discovery rate (FDR) of 1% was used for peptides, proteins and phosphosites identification. For the phosphosites, a minimum Andromeda phosphopeptides score of 40 was required, as previously described [28].

Proteomic data analysis

Proteome Matrigel: Peptides and proteins were quantified according to the MaxLFQ algorithm of MaxQuant [14] version 1.4.1.0. Only proteins uniquely identified with minimum 1 unique peptide and quantified in at least three MS runs were used for the analysis.

Proteome etomoxir: The relative quantification of the phosphorylation sites against their labeled counterpart was performed by MaxQuant [14] version 1.5.0.36. Only proteins identified with minimum 1 unique peptide and quantified with a minimum of two ratio counts were used for the analysis. Proteins were considered upregulated if the SILAC ratio was higher than 0.3 ($\log_2$ scale), which was more than one standard deviation from the mean of the all calculated ratios, in a minimum of two replicates.

Phosphoproteome: The relative quantification of the phosphorylation sites against their labeled counterpart was performed by MaxQuant [14] version 1.4.1.6. Only class I sites (= sites accurately localized with

localization probability > 0.75 and score difference > 5) were used for the analysis. Phosphorylation sites were considered upregulated if the SILAC ratio was higher than 0.4 (log_2 scale), which was more than one standard deviation from the mean of the all calculated ratios, in a minimum of two replicates. For the NetworKIN analysis [29], for each phosphorylation site only the predicted kinase with highest score was considered and we required a minimum networkin score of 1.5. Motif-X analysis was performed using standard parameters, significance of 0.000001 and IPI Human Proteome as background [30]. Predicted kinase activity was calculated by means of significantly overrepresented (Fisher test, with 2% FDR) kinase motifs (used "Motifs" column of Table S3 which was generated with Perseus software, based on Human Protein Reference Database [31]) within the 83 upregulated sites upon etomoxir treatment. The 83 sites were queried against the entire phospho-dataset.

Computational analysis using genome-scale metabolic modeling

Integration of Proteomics Data: Metabolic genes for which absolute protein abundance levels (LFQ) were measured in experiments were mapped to the human genome-scale metabolic model (GSMM) [32]. The mean (over 3 replicas) of protein abundance levels in each time point (i.e., 4h, 22h) were used to infer ternary presentation of the abundance levels using 'quartile' partitioning. This allowed for integrating 50% of the measured data, such that proteins in the top 25% quartile were labelled 1 (highly abundant), proteins in the down 25% quartile were labelled "-1" (lowly abundant) and the rest were labelled "0" (moderately abundant), in each time point. Based on the GSMM gene-reaction rules, i.e., the logical dependence of each reaction on the activity of the genes associated with it, we infer the ternary state at the reaction level. This ternary representation was used as "cues" (soft constraints) to perform iMAT [11] in each time point. To assess the permissible flux range (i.e., minimal and maximal flux) of each reaction we performed flux-variability analysis (FVA) around the optimal solution that maximizes the agreement between the predicted fluxes and the proteomic measurements. Then, we sampled the solution space using ACHR algorithm and estimated the average flux of each reaction. Fold-changes between 22h and 4h were derived based on the average fluxes.

The pathway enrichment analysis based on fold change reaction flux between 4h and 22h matrigel (in Table S2) was performed using the one dimension (1D) annotation enrichment analysis available in the Perseus software [33].

CPT1A Knockout Analysis: To simulate the effect of CPT1A inhibition at 22h we simulated the metabolic state using iMAT twice: once when the reactions associated with CPT1A were active at their maximal flux, and once when they were inhibited, carrying no flux. FVA and sampling (ACHR) of the solution space were performed. Based on the average fluxes of the reactions we estimated the fold-change following CPT1A inhibition as: fluxes when CPT1A was inactive/fluxes when CPT1A was active.

Sample preparation for metabolomic analysis

HUVECs were seeded on a solidified matrigel (six well plate, 200 µl/9.6 cm^2) in EGM-2 medium. After 3h, 22h and 30h, cells were washed with PBS, and medium replaced with 1 ml EGM-2, 11mM $^{13}C_6$ Glucose and 100µM $^{12}C_{16}$ palmitic acid or 11mM $^{12}C_6$ Glucose and 100µM $^{13}C_{16}$ palmitic acid. After 6h incubation at 37°C metabolites were extracted as follow from triplicate samples:

Extracellular: 20 µl of supernatant were mixed with 980 µl of cold methanol:ACN:water (5 volumes:3 volumes:2 volumes) extraction buffer, mixed (using a thermo-mixer) for 10 min at 4°C and spun 10 min at 16,100g at 4°C. Of the cleared supernatant, 800 µl were stored at -80°C until MS analysis.

Intracellular: cells were quickly washed with cold PBS and metabolites extracted upon incubation with ~250 µl of cold extraction buffer for 5 min at 4°C. Metabolites were then collected and mixed (using a thermo-mixer) for 10 min at 4°C and spun 10 min at 16,100g at 4°C. Of the cleared supernatant, 200 µl were stored at -80°C until MS analysis.

Metabolomics MS analysis

Metabolites were analyzed on an Exactive Orbitrap mass spectrometer (Thermo Fisher Scientific) coupled online with a Accela HPLC system (Thermo Fisher Scientific). The HPLC setup consisted of a ZIC-pHILIC column (150 x 2.1mm, 5µm, SeQuant, Merck KGaA), with a ZIC-pHILIC guard column (SeQuant, 20 x 2.1mm) and an initial mobile phase of 20% 20mM ammonium carbonate pH 9.4 and 80% acetonitrile. Of the

metabolites extracted from the cells and supernatant, 5µl were injected and separated over a 30 min mobile phase gradient, decreasing the acetonitrile content to 20%, at a flow rate of 100 µl/min. The total analysis time was 38 minutes. All metabolites were detected across a mass range of 75-1000 m/z at a resolution of 25,000, at 200m/z, with electrospray ionization and polarity switching to enable both positive and negative ions to be determined in the same run. Lock masses were used and the mass accuracy obtained for all metabolites was below 5ppm. Data were acquired with Xcalibur software.

Metabolomics data analysis

The peak areas (= measured intensity) of different metabolites were determined using LCquan software (Thermo Fisher Scientific) where metabolites were identified by the exact mass of the singly charged ion and by known retention time on the HPLC column. Commercial standards of all metabolites detected had been analyzed previously on the same LC-MS system. The ^{13}C labelling patterns were determined by measuring peak areas for the accurate mass of each isotopologue of many metabolites. The measure intensities of the intracellular metabolites were normalized to the amount of unlabeled intracellular arginine and phenylalanine.

SiRNA

For matrigel and Ca^{2+} imaging experiments: the day before transfection, HUVECs were seeded in six-well plates at a concentration of $2x10^5$ cells/well. Transfection of the siRNA duplexes was performed with Oligofectamine according to the manufacturer's protocol (Invitrogen, Carlsbad, CA, USA). Briefly, cells were transfected with 375 pmol of non-targeting (Dharmacon- GE Healthcare) or luciferase-targeting siRNA as control, or pool or single Stealth Select RNAi for CPT1A: iCPT1A#1: CCACCAAGAUCUGGAUGGGUAUGGU; SiCPT1A#2: GGACCGGGAGGAAAUCAAACCAAUU (Invitrogen). After 48h since the transfection, cells were used for experiments. For the fibrin in-vitro angiogenesis assay and TEER, HUVECs were transfected using the Amaxa Kit (Lonza) according to manufacturer's instruction. After 48h from transfection, cells were used for experiments.

Western blot analysis

HUVECs were lysed in 2% SDS in 100mM Tris HCl pH 7.4. Proteins were separated on NuPAGE 4-12% Bis-Tris gel (Invitrogen) and transferred to PVDF membrane (Millipore). The blots were probed with

primary antibodies. Multi-color signals were detected after incubation with secondary antibodies using Odyssey CLx instrument (LI-COR Biosciences). Signals were quantified using Image Studio lite software (LI-COR Biosciences).

Cell proliferation and cell death

Cell proliferation and cell death were assessed using Click-iT EdU kit and Annexin V kit (Invitrogen) according to manufacturer's protocol. Briefly, HUVECs were seeded at a concentration of 160 cells/mm^2 in EGM-2 medium with the indicated concentration of stimuli. After 20 hours, cells were harvested (for EdU incorporation, EdU was added 1.5-2 hours before cell harvesting), stained following manufacturer's recommendations and analyzed at the FACS or by immunofluorescence (siCPT1A experiment).

3D Fibrin assay

Collagen-coated beads (Cytodex 3, Sigma- Aldrich) were covered with HUVECs, embedded into fibrin gel as previously described [34] and cultured for two days in EGM-2 medium in the presence of the indicated stimuli.

Fatty acid oxidation measurement

[1-^{14}C] palmitic acid (Perkin Elmer, Waltham, MA, USA) or palmitic acid (Sigma) was resuspended in α-cyclodextrin (Sigma, 20 mg/ml in 10 mM Tris pH 8) to obtain a 12 µCi/ml solution. HUVECs grown fully confluent in 35 mm dish were incubated with the indicated stimuli for the indicated time and then 1.2 µCi/ml [1-^{14}C] palmitic acid was added for 4h in the presence or absence of stimuli. For the siRNA study, transfected HUVECs were seeded the day before the assay then incubated with [1-^{14}C] palmitic acid for 4h. Afetr 4h, the lids of the cell culture plates were replaced with whatman paper and saturated with 5M NaOH. Addition of 200 µl perchloric acid triggered the release of CO_2 which was captured in the whatman paper and analyzed in a scintillation counter (MicroBeta TriLux, Perkin Elmer). For the acid soluble metabolites, 1ml of medium was recovered, incubated with 200 µl 4N KOH, 30 min at 60°C to hydrolyze the acyl-CoA esters and acidified with 300 µl 1M $NaC_2H_3O_2$ and 200 µl 3N H_2SO_4. After spinning, 300 µl of the supernatant were mixed with 5 ml of a 2:1 solution of chloroform:methanol to allow phase separation. The upper aqueous phase, where the acid soluble metabolites (ASM) coming from palmitic acid oxidation are

dissolved, was incubated with scintillation fluid and analyzed in a scintillation counter. The values obtained were normalized by cell number.

Oxygen consumption rate measurement

XF96 plates (Seahorse Bioscience, North Billerica, MA, US) were coated with gelatin and $2.5x10^4$ HUVECs were seeded in EGM-2 medium. The day after, the medium was replaced with unbuffered assay medium (Seahorse Bioscience) with 0.5% FBS and 5mM glucose, pH 7.4 and cells placed at 37°C in CO_2-free incubator for 1 h. Basal oxygen-consumption rate (OCR) was recorded using the XF^{e}96 analyzer. Pyruvate and dichloroacetate were added in subsequent injections. Each measurement cycle consisted of 3 min mixing and 3 min measuring. At the end of the experiment 1 μM antimycin A was added in order to measure mitochondria-independent oxygen consumption. Mitochondria-dependent OCR is plotted.

ATP, cell proliferation and cell death assays

ATP, cell proliferation and death were assessed using ATP determination kit, Click-iT EdU kit and Annexin V kit (Invitrogen) according to manufacturer instruction. For the ATP assay, HUVECs were harvested and counted, then lysed in H_2O (1ml/$1x10^6$ cells) and boiled for 10 min. After spinning, the supernatants were assessed with the ATP determination kit.

Calcium imaging

Confluent HUVECs were grown in EGM-2 medium on glass gelatin-coated coverslips for 4 days. Cells were next loaded (45 min at 37°C) with 2 μM Fura-2 AM (Invitrogen), for ratiometric cytosolic Ca^{2+} $[Ca^{2+}]i$ measurements as previously described [35]. During the experiments cells were continuously bathed with a microperfusion system. Fluorescence measurements were made using a Polychrome V spectrofluorometer (TILL Photonics, Munich BioRegio, Germany) attached to a Nikon TE-2000-S (Nikon Corporation, Melville, NY, USA) microscope and Metafluor Imaging System (Molecular Devices, Sunnyvale, CA, USA) for image acquisition using 3-second intervals. During experiments, cells were maintained in standard extracellular solution of the following composition: 145mM NaCl, 5mM KCl, 2mM $CaCl_2$, 1mM $MgCl_2$, 10mM N-(2-hydroxyethyl)-piperazine-N'-ethanesufonic acid (HEPES), 10mM glucose (NaOH to pH 7.35). Cells were continuously bathed with a microperfusion system. Each fluorescence trace (340/380 nm ratio)

represents one region of interest (ROI) corresponding to cells in the chosen image field. Appropriate controls were performed with vehicles (dH_2O). Number of oscillations was determined by IgorPro software (WaveMetrics Inc, Tigard, OR, USA) by multipeak fitting analysis function and expressed as number of oscillation/10 min. The oscillation number is expressed as mean ± SEM of at least 3 pooled experiments.

Permeability assays

In-vitro TEER: Cells were plated in EGM-2 on 12 mm gelatin-coated transwell, 0.4µm pore size polyester membrane, (Costar, NY USA) and grown tightly confluent. TEER was measured using a "chopstick" STX2 electrode connected to an EVOM2 voltohmmeter (World Precisions Instruments). TEER has been measured also in wells without cells and values have been used as background and subtracted to the values measured in the presence of cells. The normalized were used to calculate the % reported in the Figures.

In-vivo ear permeability: This assay was performed as previously described with minor modifications [36]. FVB/n wild type mice (The Jackson Laboratory) were pretreated with 4mg/Kg pyrilamine maleate salt (Sigma Aldrich) at least 30 minutes before Evans blue injection, in order to block histamine release. Next, 100µl/mouse of Evans blue (Sigma Aldrich) diluted 0.5% in saline solution was intravenously injected. After two hours, mice were randomized and subdivided into groups of 4 mice each. Different drugs were injected intradermally with the following amounts: a) 100ng, 200ng, 1µg and 2µg of etomoxir; b) 1µg, 2µg, 5µg and 10µg of oxfenicine; c) 100ng etomoxir combined with 500ng pyruvate and 5µg dichloroacetate; d) gadolinium 100µM was co-injected with 500ng of etomoxir; e) saline solution was used as negative control. Ten minutes after drug administration, the ears were excised and photographed with a stereomicroscope connected to a camera by means the Image ProPlus analyzer software. The amount of Evans blue extravasation through the vessels was quantified with ImageJ software. Mice were housed under the approval and the institutional guidelines governing the care of laboratory mice of the University of Torino Committee on Animal Research and in compliance with National and International laws and policies.

Statistical analysis

Unless indicated otherwise, p values have been calculated using a two-tailed unpaired t-test using GraphPad Prism software. $*p < 0.05$; $**p < 0.01$; $***p < 0.001$;$****p < 0.0001$.

The .raw MS files and search/identification files obtained with MaxQuant have been deposited in the ProteomeXchange Consortium (http://proteomecentral.proteomexchange.org/cgi/GetDataset) via the PRIDE partner repository with the dataset identifier PXD001186 (Username: reviewer00376@ebi.ac.uk; Password: FmscZ32o; to access visit http://tinyurl.com/m9hy5lv).

Results

ECs remodel their metabolism upon morphogenesis.

To identify metabolic pathways potentially involved in controlling EC functions, we used iMAT to integrate time-resolved proteomic data of human umbilical vein endothelial cells (HUVECs, referred to as ECs throughout the Results section) grown on matrigel with GSMM (Figure 1A). ECs were used as model because they are well-characterized primary endothelial cells, and relatively easy to isolate and culture. Using high-resolution MS and label-free quantification algorithm [14], we measured the proteome of ECs grown on matrigel for 4h (early matrigel), and 22h (late matrigel) (Table S1), because at these time points cells have a distinct phenotype. At 4h cells are spread, proliferative and have started forming a network, whereas at 22h cells are elongated, low proliferative and have assembled into a fully formed complex network (Figure 1A,B). Proteomic changes between these two time points pinpointed proteins involved in vessel maturation, including increasing levels of cell-cell adhesion proteins ve-cadherin (CDH5) and junction plakoglobin (JUP), the tyrosine kinase receptor TIE1, and the endothelial nitric oxide synthase (NOS3) [37, 38 , 39](Figure 1C). For each time point, 359 metabolic enzymes (according to RECON [32], Table S1) were quantified by MS of which 170 were defined as highly or lowly abundant and used to build up a model which predicts metabolic fluxes (Table S2). We reasoned that metabolic differences between 4h and 22h may hint at pathways relevant for the regulation of EC functions. Pathway enrichment analysis based on fold change reaction flux between early and late matrigel highlighted FAO in peroxisome, the organelle where very-long-chain FAs can be oxidized into short-chain FAs and released into the cytosol, as the most upregulated pathway when the network was fully assembled, and TCAc as the most downregulated (Table

S2). Detailed investigation of single reaction flux of FAs and glucose metabolism pinpointed increased transport into the mitochondria of long-chain FAs, such as the palmitoyl-CoA via CPT1 and CPT2, higher diffusion into the mitochondria of short-chain FAs, such as the octanoyl-CoA which can be generated by oxidation of very long fatty acids, and increased flux of acyl-CoA dehydrogenases (ACADM and ACADS)-catalyzed reactions of the FAO pathway (Figure 1D,E). Conversely, decreased flux was predicted for reactions of the glycolysis pathway catalyzed by hexokinase (HK), phosphofructokinase (PFK), aldolase (ALDO) and lactate dehydrogenase (LDH), and for the pyruvate dehydrogenase (PDH), which generates acetyl-CoA from pyruvate thus linking glycolysis to the TCAc (Figure 1D,E). To verify our model, we performed a MS stable isotope-based tracing metabolomic analysis using $^{13}C_{16}$-labeled palmitate and $^{13}C_{6}$-labeled glucose. This approach measures the metabolic activity of the cells by calculating the amount of ^{13}C-labeled palmitate and glucose that cells convert into other metabolites. After early time culture on matrigel, the ^{13}C-labeled palmitoyl-carnitine, whose formation is catalyzed by CPT1A from the $^{13}C_{16}$-labeled-palmitate, was barely detected by MS while consistently quantified when the network was fully formed after 22h and 30h. Similar results were observed for the ^{13}C-labeled aspartate which is generated from TCAc intermediates (Figure 1F and Figure S1A). Conversely, ECs in the fully formed network decreased ^{13}C-labeled glucose consumption for glycolysis, as shown by more than 50% reduction of ^{13}C-labeled secreted lactate and intermediates of glycolysis and TCAc (Figure 1G). To investigate that the above metabolic changes were specific for the matrigel system, and not an effect of general cell adhesion mechanism or adaptation of the cells to the cell culture, we used ^{14}C-labelled palmitate and measured FAO in ECs grown on culture dish for 4h and 22h. In contrast to the results obtained in the matrigel assay, ECs showed a significant reduction of FAO at 22h compared to 4h (Figure S1B). Moreover, to assess that changes in FAO were not just a reflection of the proliferative status of the cells, we measured FAO in highly and low proliferative cells (Figure S1C). This showed that low proliferating ECs had lower FAO compared to highly proliferative ones (Figure S1D). These results demonstrate the validity of our predictive metabolic model and indicate that, when assembled into a fully formed network, ECs enhance FAO while reducing glycolysis.

CPT1A inhibition impairs EC proliferation, network integrity and sprouting.

To investigate the functional role of FAO in ECs, we first exploited the predictive metabolic model and explored whether blocking FAO would alter metabolic fluxes. To this aim, we inhibited CPT1A as it is the rate limiting enzyme in FAO and its levels were increased after 24h of ECs culture on matrigel (Figure 1H). By inactivating CPT1A in the predictive metabolic model built up using the late matrigel proteomic data, a substantial decrease in cellular ATP levels was predicted (reactions 3789, 3791 and 3795 were amongst the most downregulated ones, Table S2). These results suggest that FAO is a key factor in ECs and, based on these observations, we further investigated the role of FAO in ECs by targeting CPT1A. By inhibiting CPT1A either pharmacologically with etomoxir, a well characterized drug which targets CPT1 [40], or siRNA specific for CPT1A (Figure S2A), FAO was substantially decreased (Figure 2A,B). Since 15 µg/ml etomoxir showed maximum FAO inhibition (Figure 2A), we used this concentration for the following experiments. A significant decrease in cell proliferation was measured after 24h treatment with etomoxir and when CPT1A was silenced with siRNA, but not after 4h etomoxir treatment (Figure 2C,D and Figure S2B). These changes had minor effects on cell death. While no effects were measured upon 24h inhibition of CPT1A with etomoxir (Figure 2E), a small but significant increase in cell death (by means of number of cells positive for both, propidium iodide and annexin V) was measured in cells where CPT1A was silenced for 48h (Figure 2F and Figure S2C). Next we tested the effects of CPT1A inhibition on EC morphogenesis. When we grew ECs on matrigel for 24h in the presence of etomoxir or when cells were silenced for CPT1A (Figure S2D), a significant reduction (30-40%) of the network integrity was measured (Figure 2G,H and Figure S2E,F). To exclude that this effect was exclusively due to a reduction in cell proliferation, we performed the matrigel assay in the presence of mitomycin C, a DNA cross-linker which inhibits cell proliferation [4] (Figure S2G). This experiment showed that etomoxir, but not mitomycin C treatment significantly reduced network integrity (Figure S2H). Significant defects were also observed using a three-dimension (3D) angiogenesis assay of ECs embedded into fibrin gel for two days. EC sprouting was significantly reduced in the presence of etomoxir (Figure 2I,J and Figure S2I,J). Hence, reduced CPT1A activity impairs key EC functions.

In ECs FAO supports TCAc and ATP production through oxidative phosphorylation

FAO produces intermediates for the TCAc, which is a central hub for energy production, and our metabolic model predicted a sizable contribution of CPT1A to maintain ATP levels. Therefore, we measured the effects of CPT1A inhibition on cellular ATP levels. Due to the limited number and accessibility of ECs when grown on matrigel, to investigate the role of FAO in ECs, we performed experiments using EC cultured in a monolayer. Acute (3h) etomoxir treatment of ECs reduced total ATP levels of ~10% (Figure 3A). This result is in line with the previous literature which shows that ~80% of ATP is derived from glycolysis and the remaining from glucose, glutamine and fatty acids oxidation [4]. When we replenished the TCAc of the etomoxir-treated cells with dichloroacetate (DCA), a drug that activates the pyruvate dehydrogenase A (PDHA1) by inhibiting the pyruvate dehydrogenase kinase (Figure 3B), and pyruvate, the substrate that PDHA1 uses to generate acetyl-CoA, the ATP levels were restored almost to the levels of control cells (Figure 3A). Consistently, inhibition of CPT1A induced a significant decrease in oxygen consumption rate (OCR) and OCR levels raised with the replenishment of the TCAc with DCA and pyruvate (Figure 3C,D). Similar results were obtained upon acute inhibition of FAO with oxfenicine, which is another known inhibitor of CPT1 [10, 40] (Figure S2K-M). Thus, CPT1A activity fuels TCAc and ATP production through oxidative phosphorylation.

Phosphoproteomics unveils that CPT1A inhibition in ECs affects calcium-dependent signaling

To further investigate CPT1A functions, we used unbiased global phosphoproteomics and assessed the impact of metabolic alterations induced by acute CPT1A inhibition on EC signaling. Using a triple-SILAC approach, we measured phosphoproteomic changes after 2h etomoxir treatment and replenishment of the TCAc with pyruvate and DCA (Figure 4A). In triplicate experiments more than nine thousand accurately localized (with a median localization probability [41] of 0.999) phosphorylation sites were quantified. Of those, 83, which belong to 62 proteins, increased phosphorylation levels upon etomoxir treatment compared to non-treated control cells (Tables S3-S4). Based on Uniprot annotation, the regulated phosphoproteins included metabolic enzymes, kinases, and proteins involved in the regulation of transcription, translation, protein trafficking and cytoskeleton. Additionally, we exploited the phosphoproteomic data to look for kinases responsible for the deregulated phospho-signaling. First we evaluated that the phosphoproteomic changes were the results of altered kinase activity and not total protein levels. By measuring the cell

proteome to a depth of almost 5000 proteins, only ten proteins increased levels upon etomoxir stimulation and this subset did not include any of the proteins with regulated phosphorylation sites (Figure 4A and Table S5). Thus, etomoxir-induced phosphorylations are mostly the result of altered phospho-signaling. Next we used NetworKIN [29], a platform which combines sequence specificity, such as known linear kinase motifs surrounding the regulated phosphorylation site, and cellular context, such as physical and functional protein-protein interactions, to identify the likely kinases responsible for the regulation of the 83 sites. This analysis predicted highest number of substrates (12) for the calcium-calmodulin dependent kinase II (CamKII) group (Figure 4B, Table S6). Linear kinase motif analysis with Motif-X strengthened this prediction and pinpointed the CamKII motif, which has an arginine in position -3 of the phosphorylated site (R--Sp), as significantly over-represented among the 83 sites (Figure 4C). Similarly, CamKII was predicted active when performing a kinase motif (according to known motifs in the HPRD database) enrichment analysis using the MaxQuant module Perseus (Figure S3A). This analysis further pinpointed highly significant enrichment for the AMP-activated protein kinase (AMPK). AMPK can be directly phosphorylated and activated by CamKII [17, 42], and NetworKIN predicted two AMPK substrates, of which one is the known Ser80 of ACACA [43](Figure S3B-D). We verified by western blot analysis that ACACA increases phosphorylation upon etomoxir treatment, and further showed that in the presence of gadolinium (Gd^{3+}), which inhibits extracellular Ca^{2+} entry [44], etomoxir-induced ACACA phosphorylation was reduced (Figure S3E). Finally, detailed literature- and database-based investigation of the etomoxir-regulated phosphorylation sites pinpointed several sites on proteins related to Ca^{2+} signaling, such as the Ca^{2+} sensor STIM1 [45], the sodium/hydrogen exchanger SLC9A1, the adherens junction protein CTNNA1, the phosphatidylinositol transfer protein PITPNM2 and the GTPase-activating protein ARGHAP17 (Figure 4D). Of note, some of the sites decreased phosphorylation levels upon pyruvate and DCA treatment (Figure 4D).

All together, these data indicate that inhibition of FAO with etomoxir activates Ca^{2+}/CamKII/AMPK pathway, and suggest that CPT1A activity is required to maintain Ca^{2+} homeostasis.

Acute CPT1A inhibition alters calcium homeostasis in ECs

Measuring single-cell cytoplasmic Ca^{2+} dynamics in ECs showed that inhibition of CPT1A with etomoxir induced a striking increase (>3 fold) of Ca^{2+} oscillation frequency within minutes (Figure 5A,B). Notably,

this alteration was fully inhibited by blocking extracellular Ca^{2+} entry with Gd^{3+} or replenishing the TCAc with pyruvate and DCA (Figure 5B and Figure S4A). Demonstrating that etomoxir-induced Ca^{2+} oscillations were dependent on CPT1A inhibition, ECs silenced for CPT1A did not increase Ca^{2+} oscillations frequency when treated with etomoxir (Figure S4B,C). Moreover, similar to etomoxir, ECs treated with oxfenicine increased cytosolic Ca^{2+} oscillations, and these decreased by replenishing the TCAc (Figure 5C,D). Together these results demonstrate that in ECs CPT1A activity maintains Ca^{2+} homeostasis.

CPT1A inhibition increases EC permeability

Calcium is a key regulator of endothelial permeability [46]. Therefore, to explore if the measured Ca^{2+} alteration induced by inhibiting CPT1A had an impact on EC functions, we measured the permeability of an EC monolayer by means of trans-endothelial electrical resistance (TEER), and compared it to known inducers of hyperpermeability, thrombin and vascular endothelial growth factor (VEGF). TEER of etomoxir-treated cells showed a prominent decrease (30-40%) of resistance (= increase permeability) compared to control cells (Figure 6A). Similarly, increased permeability was measured in ECs upon 24h treatment with etomoxir or when CPT1A was silenced with siRNA (Figure S4D,E and Figure S2D). This effect was around half of that induced by 1 unit/ml of thrombin (~60% decrease) and similar to 1nM VEGF treatment (~40% decrease) (Figure S4F,G). Confirming that the above effect was driven by Ca^{2+}, ECs treated with Gd^{3+} did not increase permeability when treated with etomoxir (Figure 6A). We further exploited the TEER assay to determine whether replenishing the TCAc of etomoxir-treated ECs, which we have shown to block aberrant Ca^{2+} oscillations (Figure 5A,B), would reduce hyperpermeability. Figure 6B shows that pyruvate and DCA treatment restored etomoxir-induced increased permeability to the levels of control cells. Similar results were obtained using blood outgrowth endothelial cells (BOECs), another model of human primary endothelial cell which is derived from peripheral blood [24, 47](Figure 6C), and when CPT1 activity was inhibited with oxfenicine (Figure 6D). Hence, impaired Ca^{2+} homeostasis in CPT1-inhibited cells induces hyperpermeability. Finally, we determined if the increased permeability was dependent on the contribution of FAO to oxidative phosphorylation. To this aim, we used oligomycin, a drug which inhibits oxidative phosphorylation by blocking the ATP synthase. Similar to CPT1A inhibition, ECs treated with oligomycin

had a significantly reduced TEER. Moreover, oligomycin blocked the recovery of the hyperpermeability induced by DCA and pyruvate in etomoxir-treated ECs (Figure 6E).

CPT1A inhibition increases blood vessel leakage in-vivo

To assess the relevance of our findings also in an in-vivo context, we investigated the effects of the acute inhibition of CPT1A on vascular permeability. To this aim we used an established Evans blue-based permeability assay of mature blood vessels [36] and measured the leakage of blood vessels in the mouse ear upon intradermal injection of vehicle, etomoxir or oxfenicine. We chose this system because it allows minimizing indirect heart effects that can be induced by systemic injection of the two drugs [40]. Both etomoxir and oxfenicine induced a dose-dependent increased leakage of Evans blue (Figure 7A,B and Figure S5A,B). Notably, the effects of etomoxir were significantly reduced when co-injected with Gd^{3+} and abrogated with pyruvate and DCA (Figure 7C-F and Figure S5C,D). Mirroring the results observed in-vitro, pharmacological inhibition of CPT1A impairs vascular barrier function and this process is dependent on Ca^{2+} and TCAc activity (Figure 7G).

Discussion

In this work we built up the first predictive model of metabolic fluxes based on high-resolution quantitative proteomic data which unveiled that HUVECs increase FAO and decrease glycolysis when assembled into a fully formed network. While it has been reported that loss of the rate-limiting enzyme for glycolysis, PFKFB3, impairs EC proliferation and migration [4], so far there has been no evidence of endothelial functions altered by blockage of the FAO rate-limiting enzyme CPT1A. By means of established drugs that target CPT1A, gene silencing and global phosphoproteomics, we demonstrate that FAO sustains oxidative phosphorylation and maintains Ca^{2+} homeostasis, and that this is required to maintain adequate permeability of ECs in-vitro and established mouse blood vessels in-vivo.

iMAT is a powerful computational tool to predict human cellular metabolic fluxes integrating GSMM with gene expression data [11, 12]; here we show that this analysis can be successfully extended to the use of protein levels accurately measured by MS-proteomics. We have validated some of the predictions identified in our model, such as increased CPT1A activity and decreased funneling of glucose into glycolysis in

HUVECs assembled into a fully formed network. Moreover, we provide the full list of predicted metabolic reaction fluxes, as resource of other metabolic processes potentially involved in regulating EC behavior to be further investigated.

It has been previously shown that ECs preferentially use glucose as energy source, have modest mitochondria content, and generate only a small amount of energy through mitochondrial metabolism [4, 48]. Accordingly, in our MS metabolomic analysis we have identified only a limited subset of metabolites generated from ^{13}C-labelled palmitate. However, these were reliably quantified and led to discover that ECs increase FAO in conditions other than energetic stress [7]. While future work is needed to address if changes occurring when ECs are assembled into a fully-formed network in-vitro occur also during the maturation process of newly formed blood vessels in-vivo, our work demonstrates that FAO plays a key role in ECs because acute and prolonged CPT1A inhibition impairs several cellular functions. To identify the role of FAO in ECs, we focused on the effects of acute pharmacological inhibition of CPT1A. This approach allows dynamic manipulation and measurement of cell metabolism and signaling, and identifies initial events that lead to the altered EC phenotypes upon prolonged CPT1A inhibition. Of note, etomoxir and oxfenicine are used in clinics or preclinical trials [10], thus extending the relevance of our study to clinical context.

Phosphorylations are dynamic and reversible regulators of protein functions and we reasoned that phosphoproteomics would be excellent to investigate the signaling altered upon short-time FAO inhibition and provide hints on the functional role of CPT1A. This approach pinpointed alterations of the Ca^{2+}/CamKII/AMPK pathway. Calcium is a master regulator of cellular signaling and functions, and abnormal Ca^{2+} homeostasis can determine pathological states [49]. In the vascular context, Ca^{2+} homeostasis is crucial to maintain the barrier function of the blood vessels, and increased intracellular Ca^{2+} in ECs increases cell permeability [46]. For these reasons, we focused our attention on Ca^{2+} and demonstrate that CPT1A activity maintains Ca^{2+} homeostasis and EC permeability. Furthermore, we show that this occurs through the function of CPT1A to fuel TCAc and oxidative phosphorylation (Figure 7G). Thus, our work provides the first link between FAO and Ca^{2+} signaling. However, the detailed mechanism has still to be elucidated. Intriguingly, mitochondria regulate Ca^{2+} homeostasis by buffering cytosolic Ca^{2+} [50] and ECs can store up to 25% of the total cellular Ca^{2+} in the mitochondria [51]. It is therefore tempting to hypothesize

that the altered mitochondrial activity (reduced ATP levels and OCR) induced by FAO inhibition may affect the capability of the mitochondria to buffer Ca^{2+} and that this activates Ca^{2+}-signaling. Another interesting question to be addressed in the future is if the Ca^{2+}/CamKII/AMPK pathway is a functional driver of EC and vascular hyperpermeability observed upon CPT1A inhibition. In support of this hypothesis, it has been previously shown that increased EC permeability in response to thrombin [52] and VEGF [42] is induced through Ca^{2+}/CamKII/AMPK pathway. Moreover, when we compared etomoxir- with thrombin-driven phospho-signaling, which we have recently measured using a similar MS-proteomic approach [24], we observed that more than 50% of the phosphosites upregulated by etomoxir increased phosphorylation levels also upon thrombin stimulation (Table S3). These included proteins involved in Ca^{2+} signaling, such as STIM1 [45], SLC9A1 and ACACA. Finally, our dataset is a potential resource for the identification of other kinases (Figure 4B) and detailed molecular mechanisms (Table S3) that determine the phenotype of FAO-inhibited ECs.

In conclusion, our work highlights the power of using MS-proteomics and metabolic modeling to better understand cell metabolism and unravel its interplay with cell behavior. Here we revealed a central role for CPT1A in ECs. Finally, our results imply that inducing mitochondrial metabolism, including FAO, for example using available drugs such as DCA, could be a promising strategy to act directly on ECs and counteract permeability defects observed in diseases such as cancer, thrombosis and atherosclerosis, and trigger vascular normalization. This study opens therefore new exciting perspectives for the study of FAO in ECs in pathophysiological conditions.

References

1. Goddard, L.M., and Iruela-Arispe, M.L. (2013). Cellular and molecular regulation of vascular permeability. Thromb Haemost *109*, 407-415.
2. Borissoff, J.I., Spronk, H.M., Heeneman, S., and ten Cate, H. (2009). Is thrombin a key player in the 'coagulation-atherogenesis' maze? Cardiovasc Res *82*, 392-403.
3. Jain, R.K. (2005). Normalization of tumor vasculature: an emerging concept in antiangiogenic therapy. Science (New York, N.Y *307*, 58-62.
4. De Bock, K., Georgiadou, M., Schoors, S., Kuchnio, A., Wong, B.W., Cantelmo, A.R., Quaegebeur, A., Ghesquiere, B., Cauwenberghs, S., Eelen, G., et al. (2013). Role of PFKFB3-driven glycolysis in vessel sprouting. Cell *154*, 651-663.

5. Spolarics, Z., Lang, C.H., Bagby, G.J., and Spitzer, J.J. (1991). Glutamine and fatty acid oxidation are the main sources of energy for Kupffer and endothelial cells. Am J Physiol *261*, G185-190.
6. Leighton, B., Curi, R., Hussein, A., and Newsholme, E.A. (1987). Maximum activities of some key enzymes of glycolysis, glutaminolysis, Krebs cycle and fatty acid utilization in bovine pulmonary endothelial cells. FEBS Lett *225*, 93-96.
7. Dagher, Z., Ruderman, N., Tornheim, K., and Ido, Y. (2001). Acute regulation of fatty acid oxidation and amp-activated protein kinase in human umbilical vein endothelial cells. Circulation research *88*, 1276-1282.
8. Schoors, S., De Bock, K., Cantelmo, A.R., Georgiadou, M., Ghesquiere, B., Cauwenberghs, S., Kuchnio, A., Wong, B.W., Quaegebeur, A., Goveia, J., et al. (2014). Partial and transient reduction of glycolysis by PFKFB3 blockade reduces pathological angiogenesis. Cell Metab *19*, 37-48.
9. Sawada, N., Jiang, A., Takizawa, F., Safdar, A., Manika, A., Tesmenitsky, Y., Kang, K.T., Bischoff, J., Kalwa, H., Sartoretto, J.L., et al. (2014). Endothelial PGC-1alpha mediates vascular dysfunction in diabetes. Cell Metab *19*, 246-258.
10. Carracedo, A., Cantley, L.C., and Pandolfi, P.P. (2013). Cancer metabolism: fatty acid oxidation in the limelight. Nat Rev Cancer *13*, 227-232.
11. Shlomi, T., Cabili, M.N., Herrgard, M.J., Palsson, B.O., and Ruppin, E. (2008). Network-based prediction of human tissue-specific metabolism. Nat Biotechnol *26*, 1003-1010.
12. Jerby, L., and Ruppin, E. (2012). Predicting drug targets and biomarkers of cancer via genome-scale metabolic modeling. Clin Cancer Res *18*, 5572-5584.
13. Ong, S.E., Blagoev, B., Kratchmarova, I., Kristensen, D.B., Steen, H., Pandey, A., and Mann, M. (2002). Stable isotope labeling by amino acids in cell culture, SILAC, as a simple and accurate approach to expression proteomics. Mol Cell Proteomics *1*, 376-386.
14. Cox, J., Hein, M.Y., Luber, C.A., Paron, I., Nagaraj, N., and Mann, M. (2014). MaxLFQ allows accurate proteome-wide label-free quantification by delayed normalization and maximal peptide ratio extraction. Mol Cell Proteomics.
15. Lamond, A.I., Uhlen, M., Horning, S., Makarov, A., Robinson, C.V., Serrano, L., Hartl, F.U., Baumeister, W., Werenskiold, A.K., Andersen, J.S., et al. (2012). Advancing cell biology through proteomics in space and time (PROSPECTS). Mol Cell Proteomics *11*, O112 017731.
16. Sengupta, S., Peterson, T.R., and Sabatini, D.M. (2010). Regulation of the mTOR complex 1 pathway by nutrients, growth factors, and stress. Mol Cell *40*, 310-322.
17. Hardie, D.G. (2011). AMP-activated protein kinase: an energy sensor that regulates all aspects of cell function. Genes Dev *25*, 1895-1908.
18. Reid, S., Hernandez-Fernaud, J.R., and Zanivan, S. (2014). In vivo quantitative proteomics for the study of oncometabolism. Methods Enzymol *543*, 235-259.
19. Zanivan, S., Maione, F., Hein, M.Y., Hernandez-Fernaud, J.R., Ostasiewicz, P., Giraudo, E., and Mann, M. (2013). SILAC-based proteomics of human primary endothelial cell morphogenesis unveils tumor angiogenic markers. Mol Cell Proteomics *12*, 3599-3611.
20. Arnaoutova, I., George, J., Kleinman, H.K., and Benton, G. (2009). The endothelial cell tube formation assay on basement membrane turns 20: state of the science and the art. Angiogenesis *12*, 267-274.
21. Wisniewski, J.R., Zougman, A., and Mann, M. (2009). Combination of FASP and StageTip-based fractionation allows in-depth analysis of the hippocampal membrane proteome. J Proteome Res *8*, 5674-5678.
22. Wisniewski, J.R., Zougman, A., Nagaraj, N., and Mann, M. (2009). Universal sample preparation method for proteome analysis. Nature methods *6*, 359-362.
23. Larsen, M.R., Thingholm, T.E., Jensen, O.N., Roepstorff, P., and Jorgensen, T.J. (2005). Highly selective enrichment of phosphorylated peptides from peptide mixtures using titanium dioxide microcolumns. Mol Cell Proteomics *4*, 873-886.
24. van den Biggelaar, M., Hernandez-Fernaud, J.R., van den Eshof, B.L., Neilson, L.J., Meijer, A.B., Mertens, K., and Zanivan, S. (2014). Quantitative phosphoproteomics unveils temporal dynamics of thrombin signaling in human endothelial cells. Blood *123*, e22-36.
25. Rappsilber, J., Ishihama, Y., and Mann, M. (2003). Stop and go extraction tips for matrix-assisted laser desorption/ionization, nanoelectrospray, and LC/MS sample pretreatment in proteomics. Analytical chemistry *75*, 663-670.

26. Cox, J., and Mann, M. (2008). MaxQuant enables high peptide identification rates, individualized p.p.b.-range mass accuracies and proteome-wide protein quantification. Nat Biotechnol *26*, 1367-1372.
27. Cox, J., Neuhauser, N., Michalski, A., Scheltema, R.A., Olsen, J.V., and Mann, M. (2011). Andromeda - a peptide search engine integrated into the MaxQuant environment. J Proteome Res.
28. Sharma, K., D'Souza, R.C., Tyanova, S., Schaab, C., Wisniewski, J.R., Cox, J., and Mann, M. (2014). Ultradeep human phosphoproteome reveals a distinct regulatory nature of tyr and ser/thr-based signaling. Cell Rep *8*, 1583-1594.
29. Horn, H., Schoof, E.M., Kim, J., Robin, X., Miller, M.L., Diella, F., Palma, A., Cesareni, G., Jensen, L.J., and Linding, R. (2014). KinomeXplorer: an integrated platform for kinome biology studies. Nature methods *11*, 603-604.
30. Schwartz, D., and Gygi, S.P. (2005). An iterative statistical approach to the identification of protein phosphorylation motifs from large-scale data sets. Nat Biotechnol *23*, 1391-1398.
31. Keshava Prasad, T.S., Goel, R., Kandasamy, K., Keerthikumar, S., Kumar, S., Mathivanan, S., Telikicherla, D., Raju, R., Shafreen, B., Venugopal, A., et al. (2009). Human Protein Reference Database--2009 update. Nucleic Acids Res *37*, D767-772.
32. Duarte, N.C., Becker, S.A., Jamshidi, N., Thiele, I., Mo, M.L., Vo, T.D., Srivas, R., and Palsson, B.O. (2007). Global reconstruction of the human metabolic network based on genomic and bibliomic data. Proc Natl Acad Sci U S A *104*, 1777-1782.
33. Cox, J., and Mann, M. (2012). 1D and 2D annotation enrichment: a statistical method integrating quantitative proteomics with complementary high-throughput data. BMC Bioinformatics *13 Suppl 16*, S12.
34. Nakatsu, M.N., and Hughes, C.C. (2008). An optimized three-dimensional in vitro model for the analysis of angiogenesis. Methods Enzymol *443*, 65-82.
35. Fiorio Pla, A., Ong, H.L., Cheng, K.T., Brossa, A., Bussolati, B., Lockwich, T., Paria, B., Munaron, L., and Ambudkar, I.S. (2012). TRPV4 mediates tumor-derived endothelial cell migration via arachidonic acid-activated actin remodeling. Oncogene *31*, 200-212.
36. Sun, Z., Li, X., Massena, S., Kutschera, S., Padhan, N., Gualandi, L., Sundvold-Gjerstad, V., Gustafsson, K., Choy, W.W., Zang, G., et al. (2012). VEGFR2 induces c-Src signaling and vascular permeability in vivo via the adaptor protein TSAd. J Exp Med *209*, 1363-1377.
37. Dejana, E., Tournier-Lasserve, E., and Weinstein, B.M. (2009). The control of vascular integrity by endothelial cell junctions: molecular basis and pathological implications. Dev Cell *16*, 209-221.
38. Kashiwagi, S., Tsukada, K., Xu, L., Miyazaki, J., Kozin, S.V., Tyrrell, J.A., Sessa, W.C., Gerweck, L.E., Jain, R.K., and Fukumura, D. (2008). Perivascular nitric oxide gradients normalize tumor vasculature. Nat Med *14*, 255-257.
39. Sato, T.N., Tozawa, Y., Deutsch, U., Wolburg-Buchholz, K., Fujiwara, Y., Gendron-Maguire, M., Gridley, T., Wolburg, H., Risau, W., and Qin, Y. (1995). Distinct roles of the receptor tyrosine kinases Tie-1 and Tie-2 in blood vessel formation. Nature *376*, 70-74.
40. Rupp, H., Zarain-Herzberg, A., and Maisch, B. (2002). The use of partial fatty acid oxidation inhibitors for metabolic therapy of angina pectoris and heart failure. Herz *27*, 621-636.
41. Olsen, J.V., Blagoev, B., Gnad, F., Macek, B., Kumar, C., Mortensen, P., and Mann, M. (2006). Global, in vivo, and site-specific phosphorylation dynamics in signaling networks. Cell *127*, 635-648.
42. Stahmann, N., Woods, A., Spengler, K., Heslegrave, A., Bauer, R., Krause, S., Viollet, B., Carling, D., and Heller, R. (2010). Activation of AMP-activated protein kinase by vascular endothelial growth factor mediates endothelial angiogenesis independently of nitric-oxide synthase. J Biol Chem *285*, 10638-10652.
43. Ha, J., Daniel, S., Broyles, S.S., and Kim, K.H. (1994). Critical phosphorylation sites for acetyl-CoA carboxylase activity. J Biol Chem *269*, 22162-22168.
44. Shinde, A.V., Motiani, R.K., Zhang, X., Abdullaev, I.F., Adam, A.P., Gonzalez-Cobos, J.C., Zhang, W., Matrougui, K., Vincent, P.A., and Trebak, M. (2013). STIM1 controls endothelial barrier function independently of Orai1 and Ca2+ entry. Sci Signal *6*, ra18.
45. Soboloff, J., Rothberg, B.S., Madesh, M., and Gill, D.L. (2012). STIM proteins: dynamic calcium signal transducers. Nat Rev Mol Cell Biol *13*, 549-565.
46. Tiruppathi, C., Minshall, R.D., Paria, B.C., Vogel, S.M., and Malik, A.B. (2002). Role of Ca2+ signaling in the regulation of endothelial permeability. Vascul Pharmacol *39*, 173-185.

47. Martin-Ramirez, J., Hofman, M., van den Biggelaar, M., Hebbel, R.P., and Voorberg, J. (2012). Establishment of outgrowth endothelial cells from peripheral blood. Nat Protoc *7*, 1709-1715.
48. Groschner, L.N., Waldeck-Weiermair, M., Malli, R., and Graier, W.F. (2012). Endothelial mitochondria--less respiration, more integration. Pflugers Arch *464*, 63-76.
49. Berridge, M.J., Bootman, M.D., and Roderick, H.L. (2003). Calcium signalling: dynamics, homeostasis and remodelling. Nat Rev Mol Cell Biol *4*, 517-529.
50. Rizzuto, R., De Stefani, D., Raffaello, A., and Mammucari, C. (2012). Mitochondria as sensors and regulators of calcium signalling. Nat Rev Mol Cell Biol *13*, 566-578.
51. Wood, P.G., and Gillespie, J.I. (1998). Evidence for mitochondrial Ca(2+)-induced Ca2+ release in permeabilised endothelial cells. Biochem Biophys Res Commun *246*, 543-548.
52. Stahmann, N., Woods, A., Carling, D., and Heller, R. (2006). Thrombin activates AMP-activated protein kinase in endothelial cells via a pathway involving Ca2+/calmodulin-dependent protein kinase kinase beta. Mol Cell Biol *26*, 5933-5945.

Acknowledgements

We thank the BAIR facility at the Beatson, the nurses at the Southern General Hospital in Glasgow for the collection of the umbilical cords and Guido Serini for critically reading the manuscript. This work was supported by Cancer Research UK.

Figure legends

Figure 1. ECs remodel their metabolism when assembled into a fully formed vascular network.

(**A**) Workflow showing the model used to study EC morphogenesis, and how high-resolution proteomics has been integrated into the genome scale metabolic model using integrative metabolic analysis tool (iMAT). (**B**) HUVECs decrease proliferation when grown for 24h on matrigel compared to 3h, assessed by EdU incorporation (= % of cells in S phase of the cell cycle). (**C**) Logarithmized LFQ intensity ratio (22h/4h) measured for the cell-cell junction proteins ve-cadherin (CDH5) and plakoglobin (JUP), the tyrosine kinase receptor TIE1, and the endothelial nitric oxide synthase (NOS3), which were found more abundant in HUVECs cultured on matrigel for 22h compared to 4h. Bars represent mean of the LFQ intensity ratio ± SD ($n \geq 3$) as reported in Table S1. (**D**) Predicted flux changes upon morphogenesis for fatty acid oxidation (FAO) and glycolysis reactions. X axis = enzymes that catalyze the reaction. HK = hexokinase; PFK = phosphofructokinase; ALDO = aldolase; LDH = lactate dehydrogenase; PDH = pyruvate dehydrogenase; CPT = carnitine O-palmitoyltransferase; ACADM/S = medium(M)/short(S)-chain specific acyl-CoA

dehydrogenase, mitochondrial; Diff = diffusion octanoyl-CoA. (**E**) Schematic representation of cell metabolism with highlighted the pathways in (D). OxPhos = oxidative phosphorylation. In brackets = reaction ID as in Table S2. (**F**,**G**) Tracing experiment where ECs were cultured for 3h or 22h on matrigel followed by spike-in of $^{13}C_6$-labeled palmitate (F) or $^{13}C_{16}$ glucose (G) and 6h culture. Labeled (%) = % of labeled metabolite (peak area labeled) of the total amount (peak area labeled + peak area unlabeled). Peak area represents the amount of ^{13}C-labeled palmitoyl carnitine or lactate as measured by the mass spectrometer. For the palmitoyl carnitine the labeled (%) could not be measured because the unlabeled palmitoyl-carnitine was not detected by MS. For the lactate, peak area representation allows evaluating the extent of the glycolysis fuelled by extracellular ^{13}C-labeled glucose. Δ Peak area = Extracellular palmitate uptake, which was measured as amount of ^{13}C-labelled palmitate left in the medium at the end of the experiment minus the total amount of ^{13}C-labelled palmitate that was initially spiked-in. Bars = mean ± SD (n=3). (**H**) CPT1A levels (logarithmized LFQ intensity normalized by the average LFQ intensity measured at 4h) in HUVECs cultured on matrigel for 4h or 22h. Bars = Mean ± SD (n=6).

Figure 2. FAO regulates HUVEC functions.

(**A**,**B**) Reduced FAO upon etomoxir treatment (Eto, A) or CPT1A silencing with pool siRNA (siCPT1A, B) in HUVECs measured as ^{14}C-labelled acid soluble metabolites produced from ^{14}C-labeled palmitic acid. CCPM = corrected count per minute. CCPM is expressed as percentage compared to the vehicle-treated cells (Ctl = 100%); siCtl = non-targeting siRNA. (**C**,**D**) Cell proliferation upon etomoxir treatment for the indicated time (C) or CPT1A silencing (bars represent mean ± SD) (D), measured as percentage of cells incorporating EdU. EdU^+ cells are expressed as percentage compared to the control cells (Ctl = 100%). (**E**,**F**) Propidium Iodide (PI) and annexin V (AV) staining of cells grown in the presence of etomoxir for 24h (E) or silenced for CPT1A (F) was measured by FACS. Starv = cells starved overnight in EBM-2. (**G**,**H**) Reduced integrity of the network formed by cells after 24h culture on matrigel in the presence of etomoxir (G) or when silenced for CPT1A (H). (**I**,**J**) Reduced sprouting in 3D-fibrin angiogenesis assay (48h) performed with cells in the presence of etomoxir (I) or silenced for CPT1A (J). P-value according to Mann-Whitney test (n>20 cell-coated beads).

Figure 3. FAO fuels the TCA cycle to generate energy.

(**A**) Decreased total cellular ATP levels induced by 3h etomoxir treatment raised upon pyruvate and DCA treatment, as measured by luciferase activity. Luciferase activity is expressed as percentage compared to the control (Ctl = 100%); bars represent mean ± SEM (n=9). P-value according to Mann-Whitney test. P = pyruvate; DCA = dichloroacetate. (**B**) Decreased phosphorylation levels of Ser293 and Ser300 (when phosphorylated by the pyruvate dehydrogenase kinase, PDHA1 activity is inhibited), as measured by MS in the SILAC phosphoproteomic analysis of HUVECs treated with etomoxir (Table S3). The SILAC ratio was calculated between cells treated with etomoxir and vehicle-treated cells (Ctl). A-C represents three replicate experiments. (**C**) Seahorse measurements of oxygen consumprion rate (OCR) show that etomoxir induces decrease OCR compared to control (Ctl) cells. Replenishment of the TCAc with pyruvate and DCA increases OCR in both, Ctl and etomoxir-treated cells. Arrows indicate the measurements represented in panel (D). Oligo = oligomycin 1µM. Bars represent mean ± SEM (n=20). (**D**) Quantifcation of (C). Bars represent mean ± SEM (n=20). P-value according to Mann-Whitney test.

Figure 4. Phosphoproteomics reveals altered Ca^{2+} signaling upon acute inhibition of CPT1A with etomoxir.

(**A**) Workflow of the SILAC proteomic and phosphoproteomic analysis of HUVECs treated with vehicle (Ctl), etomoxir (Eto) or etomoxir followed by pyruvate (P) and dichloroacetate (DCA) treatment (Eto-P-DCA). Results refer to three SILAC experiments, Exp 1-3, where the SILAC labeling conditions were swapped. (**B**) Predicted active kinases upon etomoxir treatment (NetwroKIN analysis). Numbers in brackets indicate the number of predicted substrates shown in Table S6. (**C**) Linear motifs identified by Motif-X analysis. (**D**) Etomoxir-upregulated phosphorylation sites on proteins involved in Ca^{2+} signaling (literature-based). Bars represent mean ± SD (n≥2).

Figure 5. Acute CPT1A inhibition induces increased Ca^{2+} oscillation freaquency.

(**A**) Representative plot of increased Ca^{2+} oscillation frequency in HUVECs upon etomoxir treatment. Each line represents a single cell. (**B**) Increased frequency of Ca^{2+} oscillations in HUVECs upon etomoxir treatment is restored in the presence of pyruvate and DCA or 100µM gadolinium (Gd^{3+}). (**C**) Representative plot of increased Ca^{2+} oscillation frequency in HUVECs upon oxfenicine treatment. Each line represents a

single cell. (**D**) Increased frequency of Ca^{2+} oscillations in HUVECs upon oxfenicine treatment is restored in the presence of pyruvate and DCA. Bars represent mean ± SEM (n>150). P-value according to Mann-Whitney test.

Figure 6. Acute CPT1A inhibition induces EC hyperpermeability.

(**A**) Decreased trans-endothelial resistance (TEER) (= increased EC permeability) in HUVECs induced by etomoxir is inhibited blocking Ca^{2+} entry pre-treating cells (10 min) with 100µM gadolinium (Gd^{3+}). (**B,C**) Decreased TEER in HUVECs (B) and BOECs (C), induced by etomoxir raises upon pyruvate (P) and dichloroacetate (DCA) treatment. (**D**) Decreased TEER in HUVECs treated with oxfenicine raised upon P and DCA treatment. (**E**) Oligomycin treatment (1µM) decreases TEER in HUVECs and abrogates the effects of P and DCA treatment in etomoxir-treated cells. Bars represent mean ± SEM (n=3).

Figure 7. Acute CPT1A inhibition increases blood vessel leakage.

(**A,B**) Quantification of Evans blue extravasation from the vasculature of the mouse ear following acute etomoxir (A) and oxfenicine (B) treatment at the indicated doses. The permeability was measured as amount of leaked blue/constant area (μm^2). (**C**) Quantification of Evans blue extravasation in (D), (E) and (F). (**D-F**) Representative images showing Evans blue extravasation from the mouse ear vasculature upon acute etomoxir treatment (5 µg) (D), which is inhibited in the presence of pyruvate and DCA (Eto-P-DCA) (E) and gadolinium (Gd^{3+}) (F). (**G**) Schematic overview of FAO function in ECs. Blue arrow indicates that the finding is supported by experiments; red dashed arrow indicates that the mechanisms have still to be determined (hypotheses are discussed in the Discussion). Bars represent mean ± SEM (n≥3).

Patella et al. Figure 1

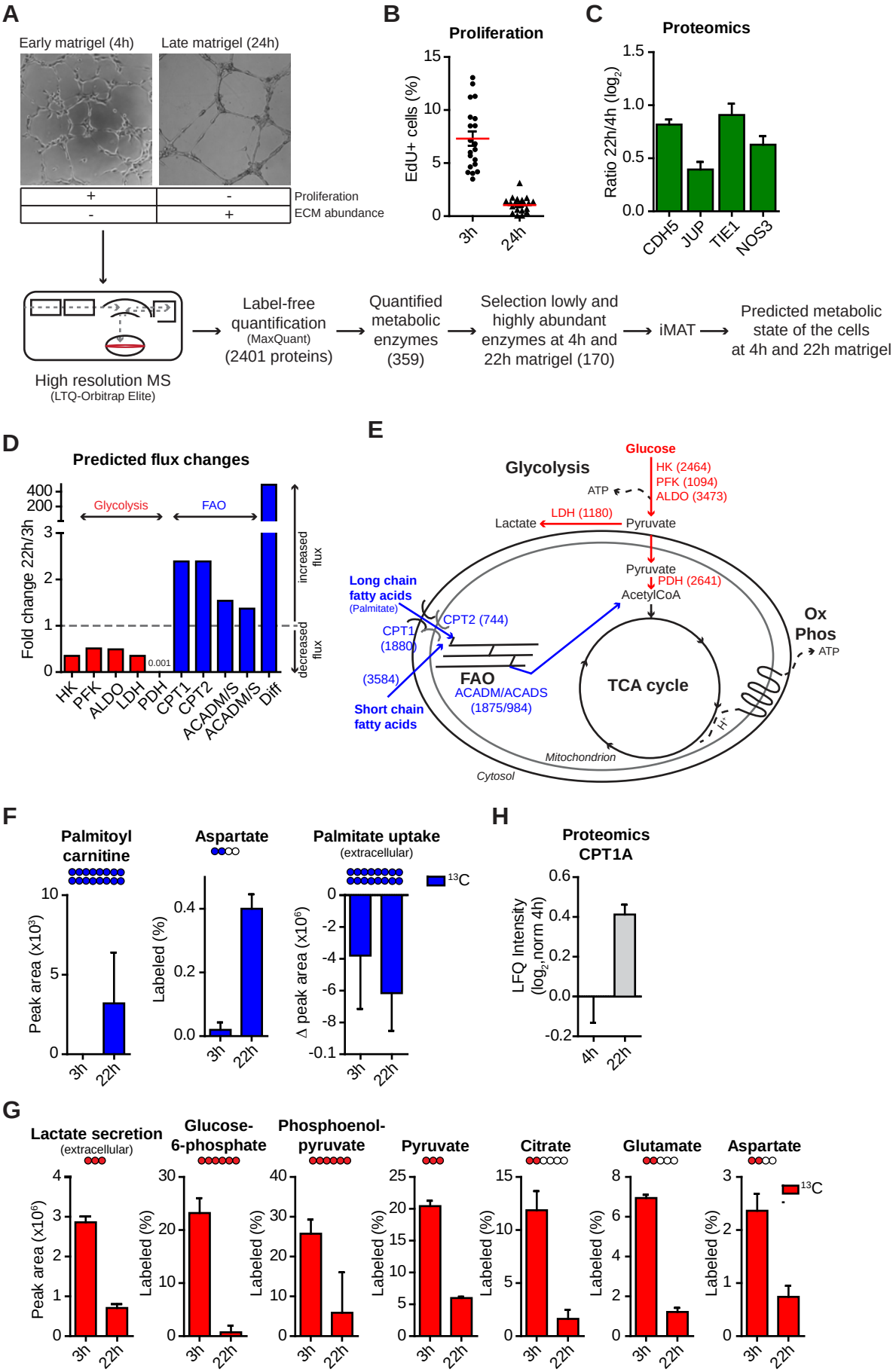

Patella et al. Figure 2

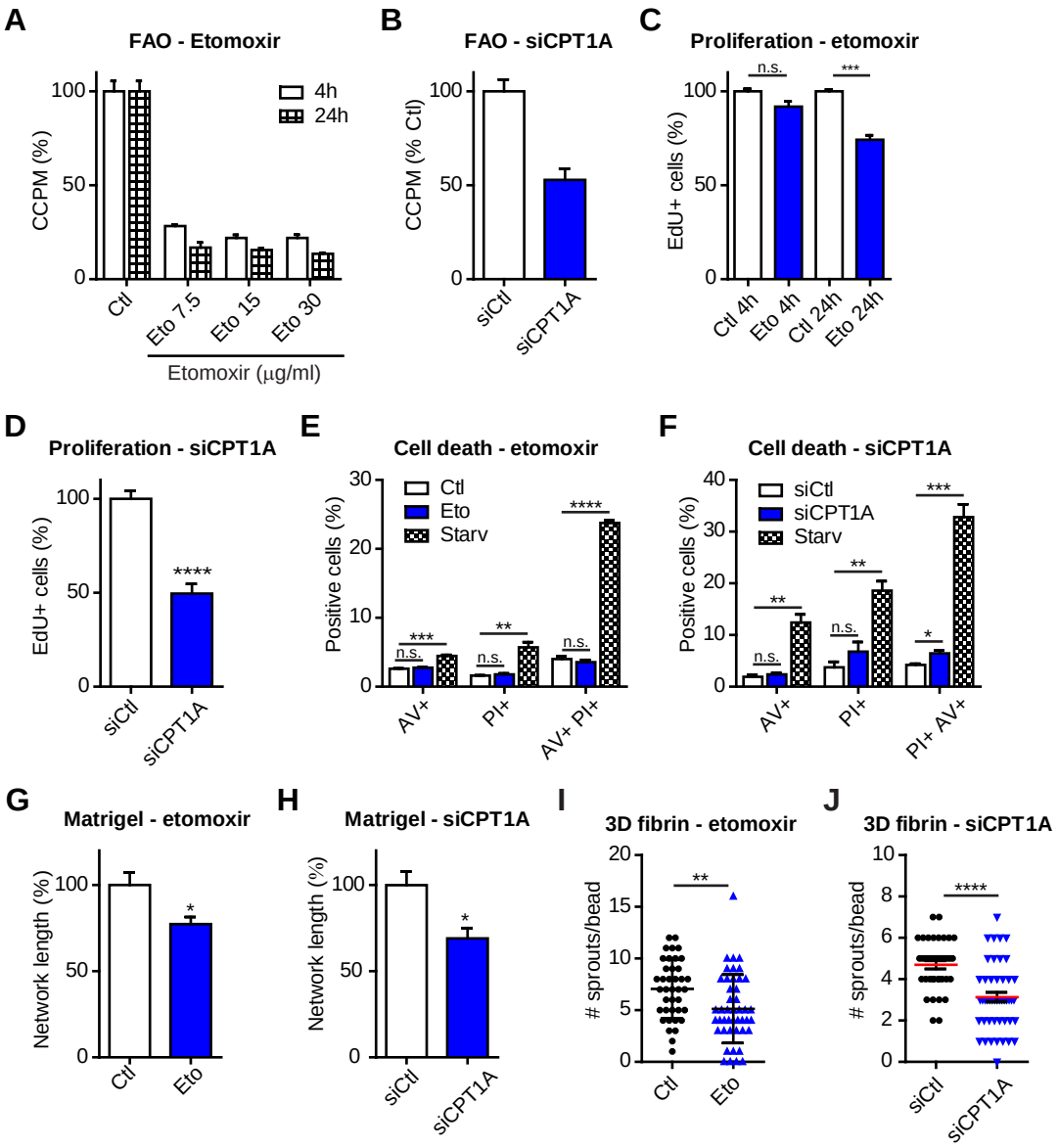

Patella et al. Figure 3

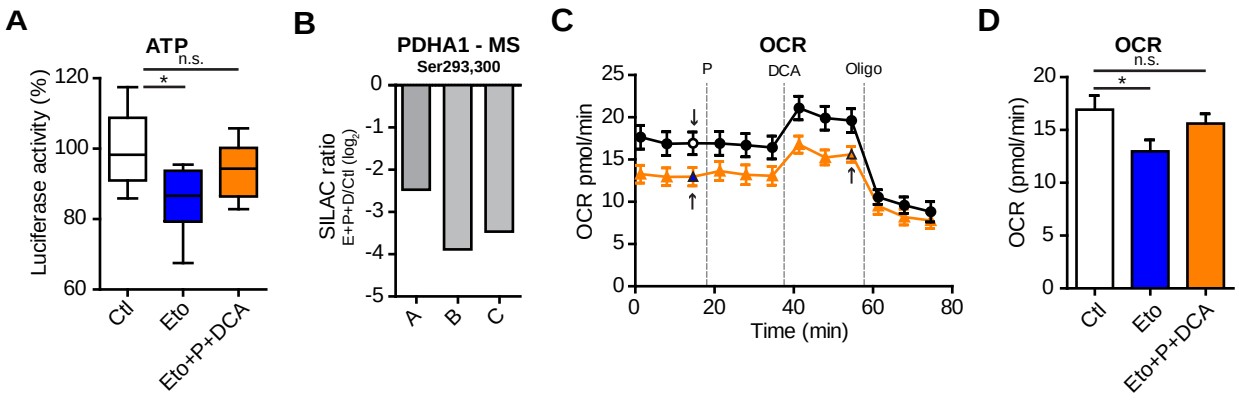

Patella et al. Figure 4

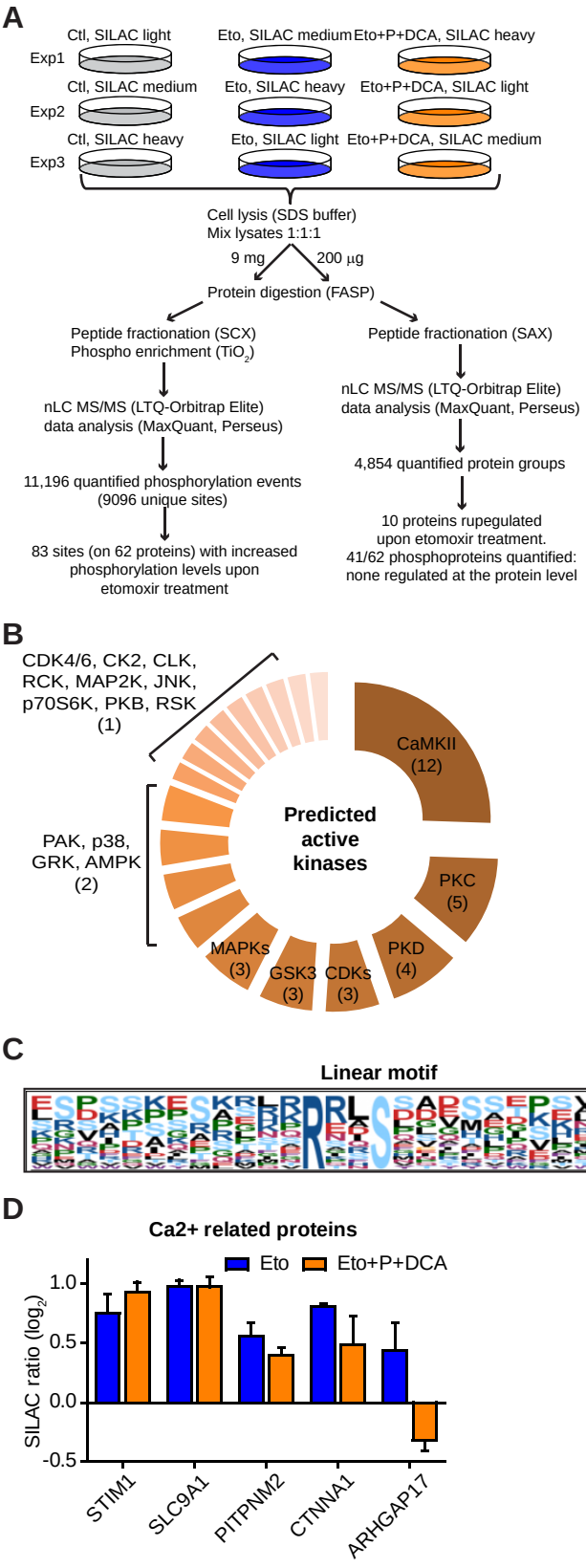

Patella et al. Figure 5

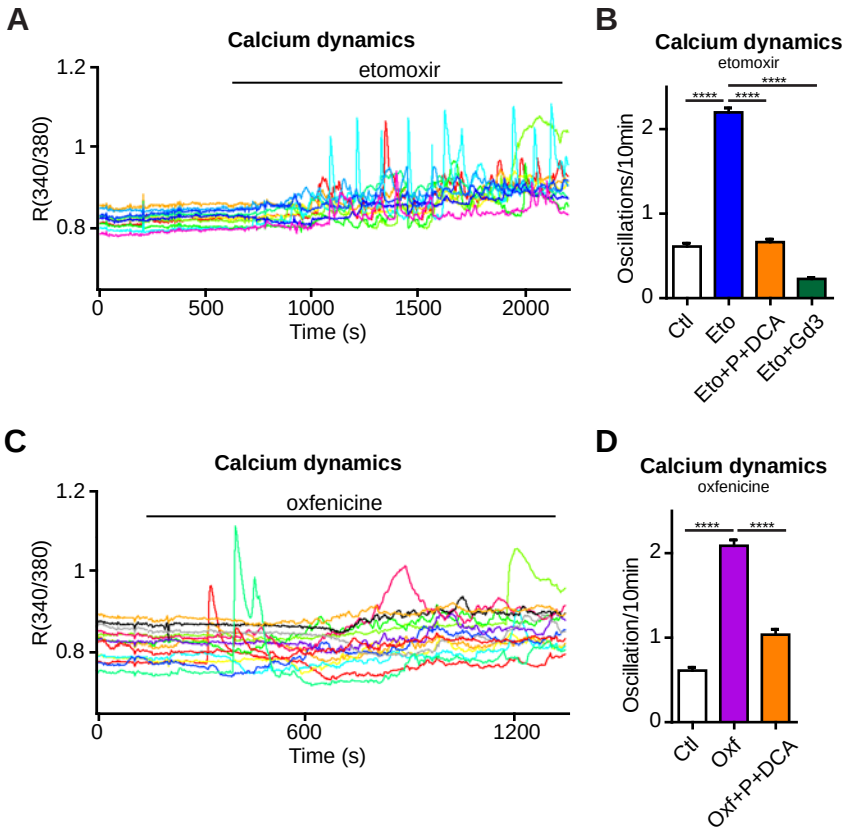

Patella et al. Figure 6

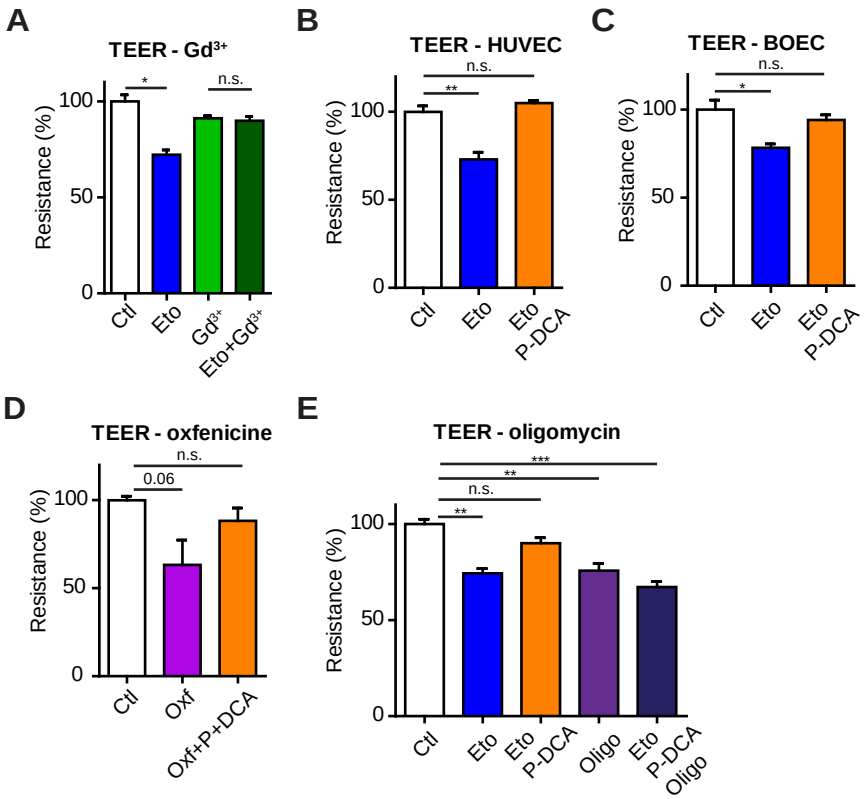

Patella et al. Figure 7

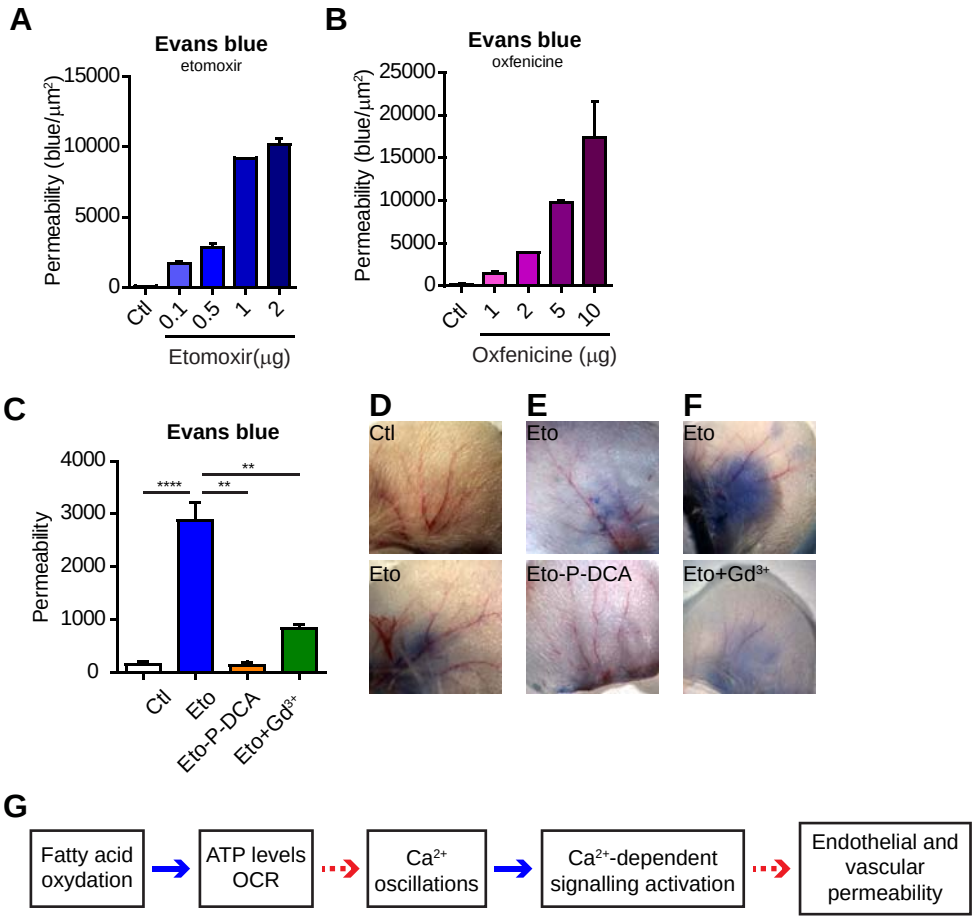

Supplemental Figures and Tables

Table S1. LFQ-based proteome quantification of HUVECs cultured on matrigel for 4h and 22h.

Table S2. Metabolic reactions flux predicted by iMAT after integration of the proteomic data (HUVECs on matrigel for 4h and 22h, Table S1) into GSMM and upon inactivation of CPT1A integrating proteomic data of HUVECs upon morphogenesis (Matrigel 22h, Table S1) into GSMM.

22h vs 4h matrigel: Full list of reactions in the GSMM showing: reaction index (ID) (column A), the metabolic pathway which the reaction belongs to (column B), reaction name (column C), reaction stoichiometric formula (column D), predicted fluxes following ACHR sampling (column E for 4h, and column F for 22h), fold-change between 22h and 4h (column G), and the gene-reaction rules (column H) where genes are indicated by their Entrez ID.

CPT1A inactivation: The full list of reactions in the GSMM is provided. Columns A-D are as above. The predicted average fluxes when CPT1A associated reactions are forced to be active (at their maximal flux as estimated by flux-variability analysis) are given in columns E and when they are inhibited (zero flux) are given in columns F. The fold-changes (flux when CPT1A is inhibited/flux when CPT1A is active) are shown in column G.

Table S3. SILAC phosphoproteome of HUVECs acutely treated with etomoxir and when TCA cycle is replenished with pyruvate and DCA. The table reports the class I phosphorylation sites (with localization probability > 0.75 and score difference > 5) and predicted kinase activity (based on kinase motifs reported in the HPRD database) upon etomoxir treatment.

Phosphoproteome: contains the relative quantification (SILAC ratio) of each phosphorylation sites whether it was quantified in singly, doubly or multiply phosphorylated peptides. This quantitative information is indicated in the "Multiplicity" column as _1, _2, _3 respectively.

Eto up-regulated sites: contains the 83 phosphosites with increased phosphorylation levels upon etomoxir treatment.

M = SILAC medium-labeled; L = SILAC light-labeled; H = SILAC heavy-labeled.

A-C = three replicate experiments.

Table S4. Annotated MS/MS spectra of the phosphorylation sites upregulated upon etomoxir treatment.

Annotated spectra as reported in the Viewer module of MaxQuant.

Table S5. SILAC proteome of HUVECs acutely treated with etomoxir and when TCA cycle is replenished with pyruvate and DCA.

SILAC-based relative quantification of identified protein groups in triplicate experiments. Ratios are reported as $\log_2$ values.

Table S6. NetworKIN output

Figure S1. HUVECs increase FAO when assembled into a fully formed network.

(**A**) Three time point results of tracing experiment where ECs were grown for 3h, 22h (results as in Figure 1) or 30h on matrigel followed by spike-in of $^{13}C_{16}$-labelled palmitate followed by additional 6h in culture. Y axis = Labeled (%) = % of labeled metabolite of the total amount (labeled + unlabeled). Δ Peak area = palmitate uptake based on the quantification of the extracellular palmitate. Tracing experiment was performed also at 30h to increase the robustness of the data obtained at 22h. Indeed, due to the low flux rate of FAO in ECs, only few labeled-metabolites could be measured by MS. (**B**) Measured FAO, by means of $^{14}CO_2$ produced from ^{14}C-labeled palmitic acid, in HUVECs grown on gelatin-coated dish for 4h and 22h. CCPM = corrected count per minute. CCPM is expressed as percentage compared to the 4h adhesion cells (4h = 100%). Bars represent mean +/- SEM (n=5). (**C**) Proliferation of HUVECs grown on culture dish for 24h or 8 days (8d) at confluence (medium was changed every second day). Percentage of cells incorporating EdU during 2h was measured. EdU^+ cells are expressed as percentage compared to the control cells (Ctl = 100%). (**D**) Measured FAO, by means of $^{14}CO_2$ produced from ^{14}C-labeled palmitic acid, in HUVECs grown on culture dish for 24h or 8 days (8d) at confluence. CCPM is expressed as percentage compared to cells grown for 24h (24h = 100%). Bars = Mean +/- SEM (n=4).

Figure S2. Effects of CPT1A inhibition in HUVECs.

(**A**) Efficiency of CPT1A silencing (72h after transfection) in HUVECs transfected with a pool of siRNA specific for CPT1A (siCPT1A). Bars represent the mean of five experiments (including those used to measure the FAO in Figure 2A) +/- SD. The efficiency is measured as % of remaining protein compared to cells transfected with a non-targeting siRNAs (siCtl = 100%) as measured by western blot and quantified using Licor software. On the right a representative western blot. Vinculin was used as loading control. (**B-D**) Western blot which shows the efficient silencing of CPT1A (48h after transfection) compared to siCtl, using two independent siRNA (#1 and #2) or a pool of siRNA. Cells silenced with the siRNA were used for the EdU incorporation experiment in Figure 2D (B), cell death analysis in Figure 2F (C), and matrigel assay in panel (E,F) and Figure 2G and TEER in Figure S4E (D). β-tubulin and vinculin were used as loading control. (**E**) Representative bright field images which show the reduced integrity of the HUVEC network formed in the presence of etomoxir or when silenced for CPT1A compared to their respective controls. (**F**) Reduced network length measured when HUVECs were cultured on matrigel for 24h in the presence of etomoxir or when silenced for CPT1A compared to their respective controls. The network length is expressed as percentage compared to the siCtl cells (siCtl = 100%). P-values according to two-tailed paired t-test (n>3). (**G**) HUVEC proliferation upon mitomycin C treatment at the indicated concentrations (bars represent single measurement) measured by means of 2h EdU incorporation. (**H**) Reduced integrity of the network formed by HUVECs after 24h culture on matrigel in the presence of etomoxir. The network was not disrupted in the presence of mitomycin C. (**I**) Western blot which shows the efficient silencing of CPT1A (48h after transfection), compared to siCtl, using two independent siRNA (#1 and #2) or a pool of siRNA. Silenced cells were used for the three dimension (3D)-fibrin assay in panel (J) and Figure 2J. β-tubulin was used as loading control. (**J**) Reduced number of sprouting HUVECs during 3D-fibrin angiogenesis assay performed with HUVECs transfected with siCtl or two independent siRNA for siCPT1A. The number of sprouts was measured after two days culture in fibrin gel. P-value according to Mann-Whitney test (n>20 cell-coated beads). (**K**) Oxfenicine treatment for 7h at the indicated concentrations reduces FAO in HUVECs, measured as ^{14}C-labelled acid soluble metabolites produced from ^{14}C-labeled palmitic acid. CCPM = corrected count per minute. Ctl = vehicle-treated cells. CCPM is expressed as percentage compared to the vehicle-treated cells (Ctl = 100%). Bars = Mean +/- SEM (n=6). (**L**) Decreased total cellular ATP levels induced by 3h treatment with oxfenicine at the indicated concentrations, measured by luciferase activity. Luciferase activity

is expressed as percentage compared to the vehicle-treated cells (Ctl = 100%). Whiskers plot, min to max. P-value according to Mann-Whitney test (n≥10). (**M**) Decreased oxygen consumption rate (OCR) induced by 3h treatment with 2.5mM oxfenicine (Oxf). Bars = Mean +/- SEM. P-value according to Mann-Whitney test (n>100).

Figure S3. Etomoxir induces phosphorylation of the AMPK substrate ACACA

(**A**) Kinases predicted to be active upon etomoxir treatment, based on kinase motif enrichment analysis done with Perseus (Fisher exact test, 2% FDR). (**B**) Increased phosphorylation levels of Ser80 of the acetyl-CoA carboxylase (ACACA) induced by etomoxir (Eto), and pyruvate (P) and dichloroacetate (DCA) treatments, as measured by MS in the SILAC phosphoproteomic analysis of HUVECs treated with etomoxir (Table S3). The SILAC ratio was calculated between cells treated with the indicated drug and vehicle-treated cells (Ctl). (**C**) Three dimensional (3D) visualization of a representative MS spectrum of SILAC triplet used for the quantification of the phosphorylated Ser80 of ACACA in HUVECs treated with the indicated stimuli. (**D**) Annotated MS/MS spectrum (from the Viewer module of MaxQuant) obtained from the fragmentation of the peptide shown in (C). (**E**) Western blot showing that increased levels of ACACA phosphorylation at Ser80 upon etomoxir treatment are reduced when cells are treated with 10µM Gd^{3+}. Vinculin was used as loading control. The panel at the bottom shows the quantification of the western blot using Licor software.

Figure S4. Effects of CPT1A inhibition on Ca^{2+} oscillation frequency and TEER.

(**A**) Increased Ca^{2+} oscillations in HUVECs upon etomoxir treatment are inhibited when cells are pre-treated with Gd^{3+}, which blocks extracellular Ca^{2+} entry. Each line represents a single cell. (**B**) Western blot which shows the efficient silencing of CPT1A (48h after transfection), compared to siCtl, using two independent siRNA (#1 and #2) or a pool of siRNA. Actin was used as loading control. Cells were used for the experiment in (C). (**C**) Calcium oscillations measured in HUVECs siCtl or siCPT1A treated or not with etomoxir. Bars show mean +/ SEM (n>100 cells). (**D, E**) Decreased trans-endothelial resistance (TEER) (= increased EC permeability) in HUVECs induced by 24h treatment with etomoxir (D) or silencing CPT1A (72h after transfection) (E). Bars represent mean ± SEM (n=3). (**F, G**) Decreased TEER in HUVECs treated

for 15min with 1 unit/ml of thrombin (F) or with 1nM $VEGF_{165}$ for the indicate time (G). Bars represent mean ± SEM (n=3).

Figure S5. Effects of CPT1A inhibition on blood vessel leakage in-vivo.

(**A,B**) Representative images (see Figure 7 A,B) showing dose-dependent Evans blue extravasation from the vasculature of the mouse ear following acute etomoxir (A)and oxfenicine (B) treatment. (**C**) Representative images showing Evans blue extravasation from the vasculature of the mouse ear injected with gadolinium (Gd^{3+}) only or with etomoxir in the presence or absence of Gd^{3+}. (**D**) Quantification of (C). The permeability was measured as amount of leaked blue/constant area (μm^2). For Figure 7, the permeability measured for the gadolinium treatment only (average of 4 mice) was subtracted to the permeability measured upon treatment with etomoxir + gadolinium. Bars represent mean +/- SEM (n=3). P-values according to two-tailed unpaired t-test.

Patella et al. Figure S5

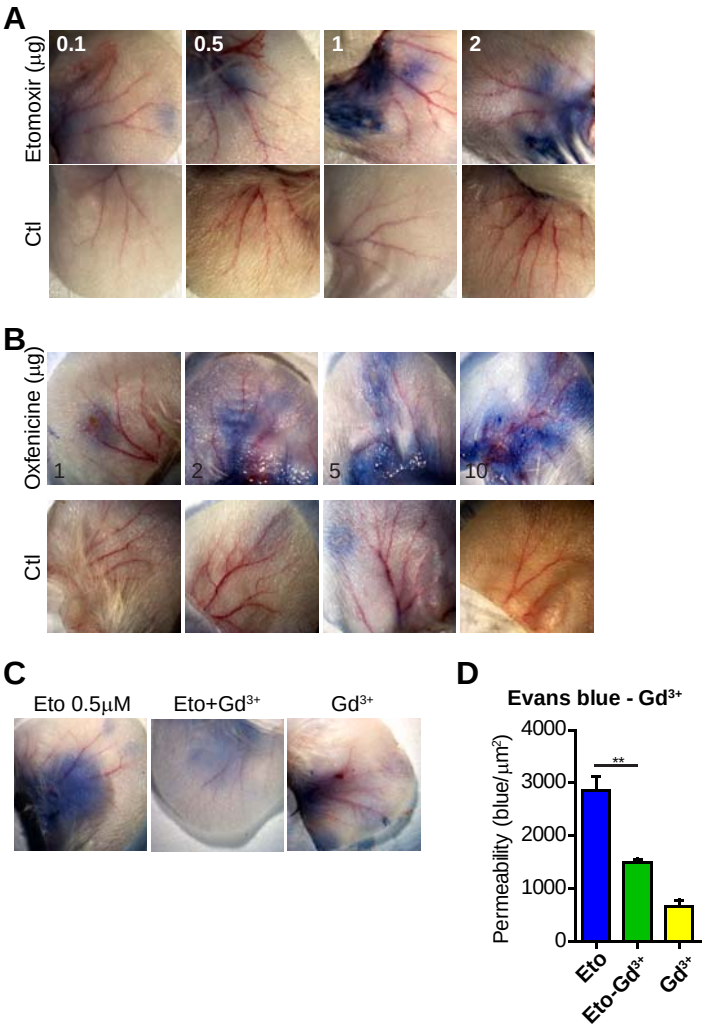

Patella et al. Figure S4

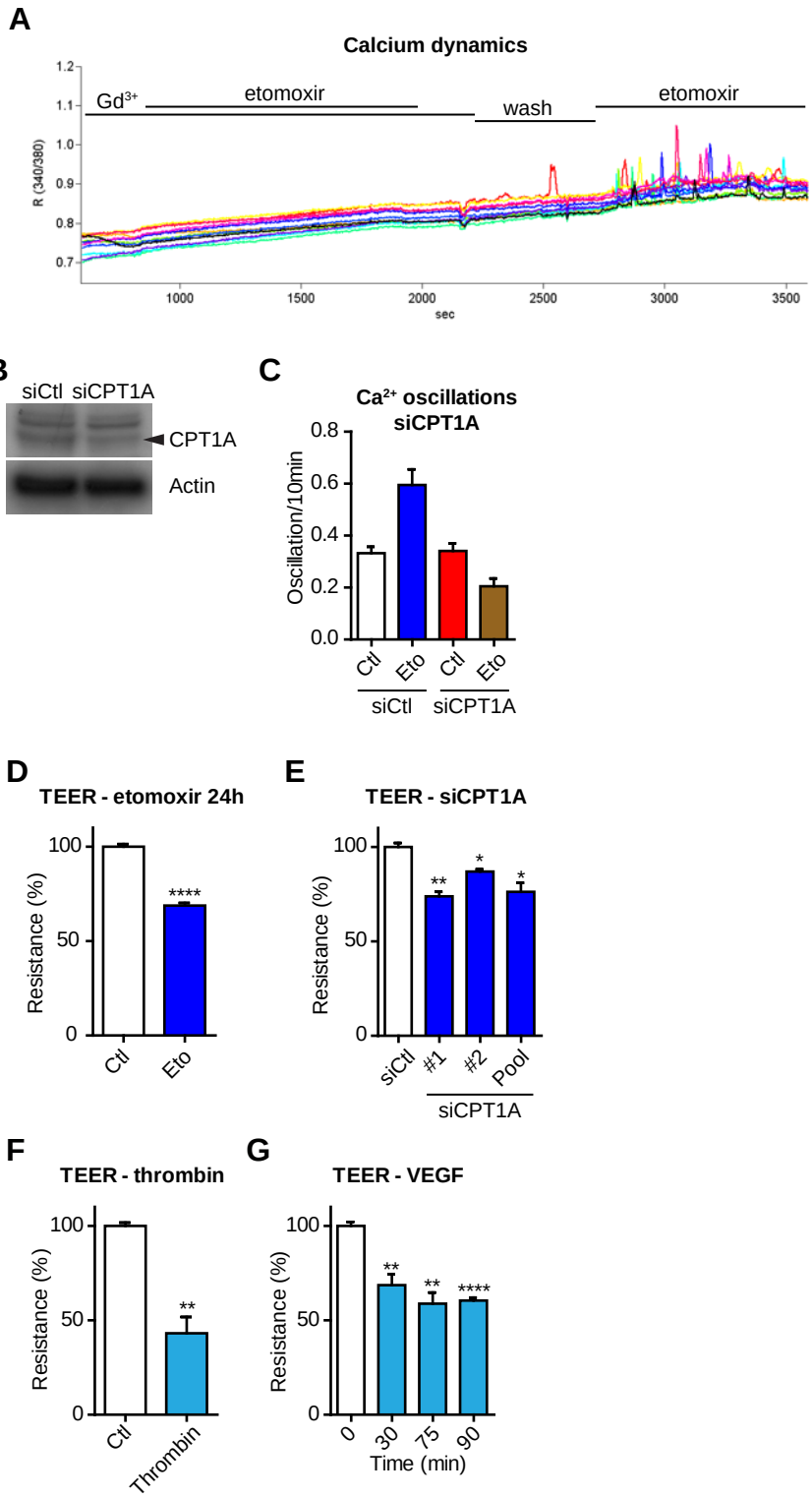

Patella et al. Figure S3

A

Predicted active kinases

Kinase motif	Enrichment score	Predicted substrates
AMP-activated protein kinase	4.4798	9
PKC epsilon kinase	3.2534	13
PAK2 kinase	3.1677	12
Calmodulin-dependent protein kinase II	1.7718	30

B

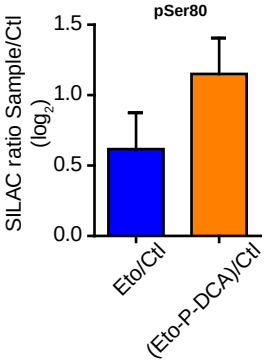

C

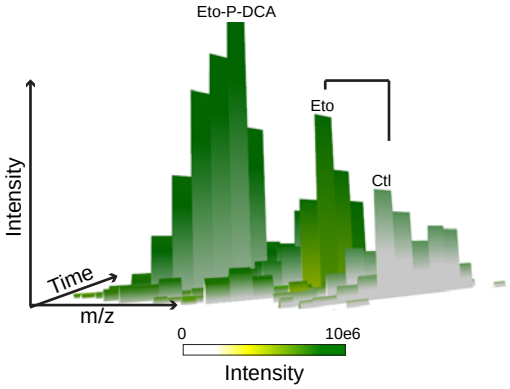

D

MS/MS annotated spectra for phosphorylated Ser80 of ACACA

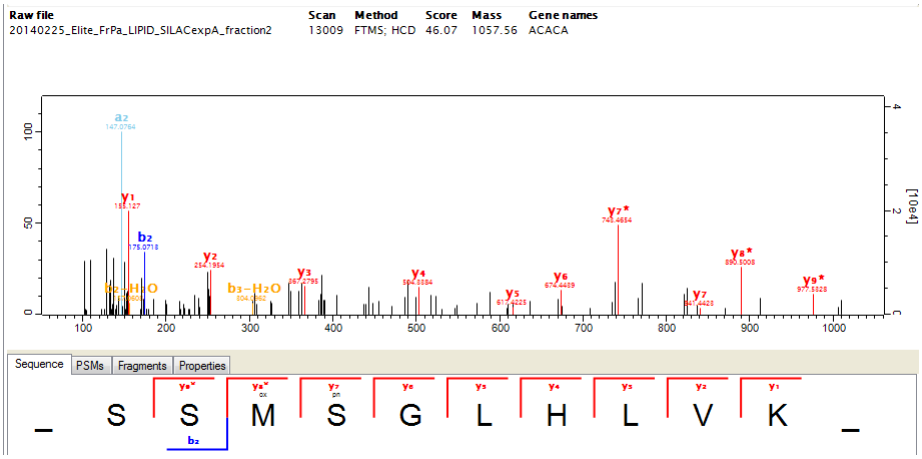

E

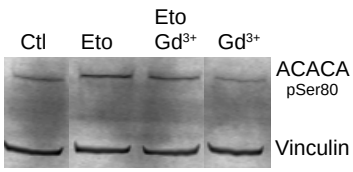

WB quantification

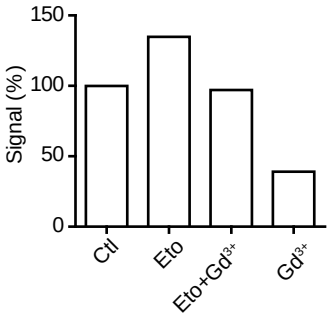

Patella et al. Figure S2

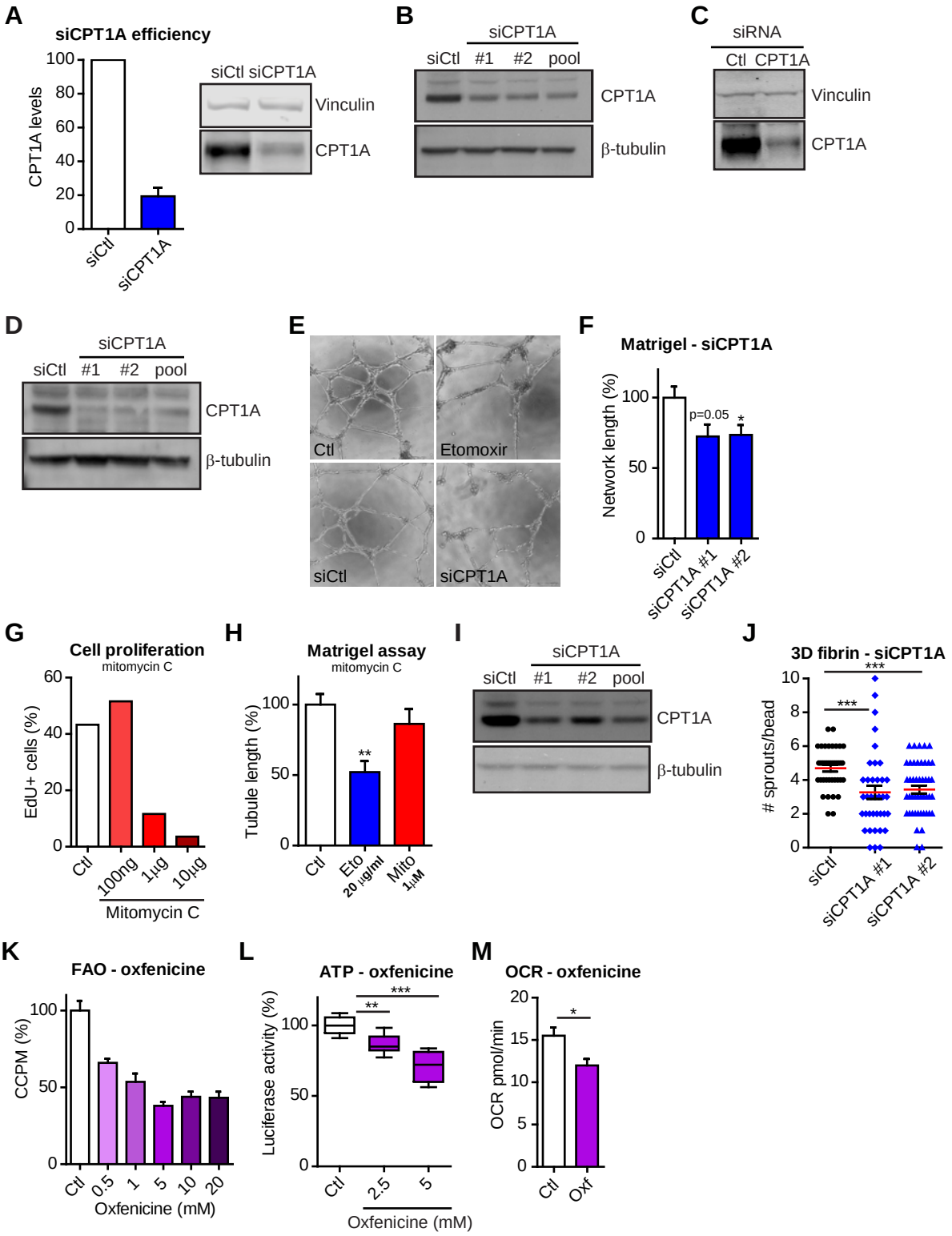

Patella et al. Figure S1

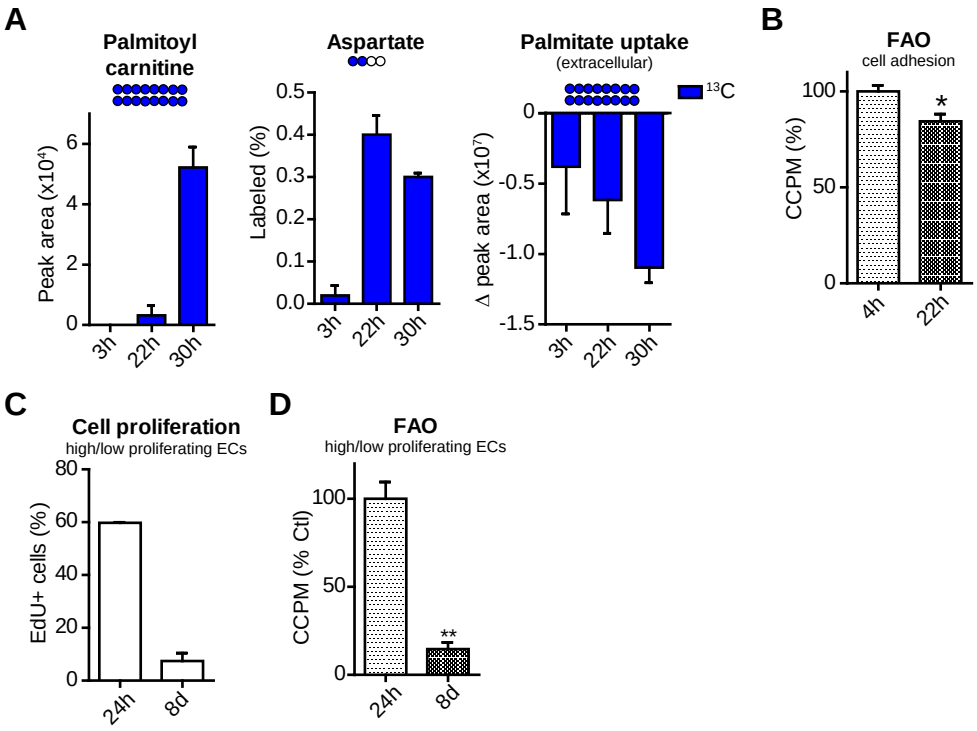

Proteomics-based metabolic modelling reveals that fatty acid oxidation controls endothelial cell permeability

Francesca Patella[1], Zachary T Schug[2], Erez Persi[3,4], Lisa J Neilson[1], Zahra Erami[5], Daniele Avanzato[6], Federica Maione[7,8], Juan R Hernandez-Fernaud[1], Gillian Mackay[2], Liang Zheng[2], Steven Reid[1], Christian Frezza[9], Enrico Giraudo[7,8], Alessandra Fiorio Pla[6], Kurt Anderson[5], Eytan Ruppin[3,10], Eyal Gottlieb[2] and Sara Zanivan[1]

[1]Vascular Proteomics Lab, [2]Apoptosis and Tumour Metabolism Lab, [5]Tumour Cell Migration Lab, Cancer Research UK Beatson Institute, Switchback Road, G61 1BD, Glasgow, UK

[3]The Blavatnik School of Computer Science, Tel Aviv University, 69978 Tel Aviv, Israel

[4]School of Physics and Astronomy, Tel Aviv University, 69978 Tel Aviv, Israel

[6]Department of Life Sciences and Systems Biology, University of Torino, Via Accademia Albertina 13, 10123 Torino, Italy

[7] Laboratory of Transgenic Mouse Models, Candiolo Cancer Institute – FPO, IRCCS, Str prov 142 Km 3.95, 10060, Candiolo, Torino, Italy

[8] Department of Science and Drug Technology, University of Torino, School of Medicine, Via P. Giuria, 9 - 10125 Torino, Italy

[9] MRC Cancer Unit, Cambridge Biomedical Campus, University of Cambridge, Hutchison/MRC Research Centre, Box 197, CB2 0XZ, Cambridge, UK

[10]Sackler School of Medicine, and Department of Molecular Microbiology and Biotechnology, Faculty of Life Sciences, Tel-Aviv University, 69978 Tel Aviv, Israel

Corresponding Author:

Sara Zanivan, PhD

Switchback Road

Glasgow G61 1BD, UK

Tel: +44(0)141 330 3971

Email: s.zanivan@beatson.gla.ac.uk

Running Title: FAO maintains endothelial permeability

Abbreviations:

EC endothelial cell

FAO fatty acid oxidation

TCAc tricarboxylic acid cycle

FA fatty acid

iMAT integrative metabolic analysis tool

GSMM genome-scale metabolic network model

SILAC stable-isotope labeling with amino acids in cell culture

HUVEC human umbilical vein endothelial cells

ECM extracellular matrix

TEER trans-endothelial electrical resistance

DCA dichloroacetate

VEGF vascular endothelial growth factor

Summary

Endothelial cells (ECs) play a key role to maintain the functionality of blood vessels. Altered EC permeability causes severe impairment in vessel stability and is a hallmark of pathologies such as cancer and thrombosis. Integrating label-free quantitative proteomics data into genome-wide metabolic modeling, we built up a model which predicts the metabolic fluxes in ECs when cultured on a tridimensional matrix and organize into a vascular-like network. We discovered how fatty acid oxidation (FAO) increases when ECs are assembled into a fully formed network that can be disrupted by inhibiting CPT1A, the FAO rate-limiting enzyme. Acute CPT1A inhibition reduces cellular ATP levels and oxygen consumption, which are restored by replenishing the tricarboxylic acid cycle (TCAc). Remarkably, global phosphoproteomic changes measured upon acute CPT1A inhibition pinpointed altered calcium signaling. Indeed, CPT1A inhibition increases intracellular calcium oscillations. Finally, inhibiting CPT1A induces hyperpermeability in-vitro and leakage of blood vessel in-vivo, which were restored blocking calcium influx or replenishing the TCAc. FAO emerges as central regulator of endothelial functions and blood vessel stability and druggable pathway to control pathological vascular permeability.

Introduction

Endothelial cells (ECs) line the inner layer of the blood vessel wall and constitute a barrier between blood and surrounding tissue. As such, a tight regulation of EC permeability is crucial to maintain vessel functionality and avoid excessive extravasation of fluid and plasma proteins [1]. Increased endothelial permeability is typical in inflammatory states and a hallmark of diseases such thrombosis, atherosclerosis and cancer [2, 3]. Because of their unique localization, ECs are constantly exposed to oxygen and nutrients which fuel cell metabolism and whose levels vary in physiological and pathological conditions. Yet, how cell metabolism regulates endothelial permeability remains incompletely understood.

Previous studies have reported that EC cultures use glucose as predominant source of energy by producing lactate through glycolysis. However, also fatty acids and glutamine contribute to ATP and metabolic intermediate production [4-7]. Recent in-vivo studies have shown that glycolysis is necessary for EC proliferation and motility in physiological and pathological angiogenesis [4, 8]. Moreover the peroxisome proliferator-activated receptor gamma coactivator 1-α, which can activate oxidative phosphorylation, blocks EC sprouting in diabetes [9]. The intriguing information emerging from these studies is that key metabolic pathways, such as glycolysis and oxidative phosphorylation in the mitochondria, play an important role in ECs and that they are actively involved in the regulation of key cell functions.

Mitochondrial fatty acid oxidation (FAO) is the process that converts fatty acids (FAs) into acetyl-CoA, which fuels the tricarboxylic acid cycle (TCAc) and generates reducing factors for producing ATP via oxidative phosphorylation. Cells can incorporate FAs from the culture media or can generate FAs from the hydrolysis of triglycerides or through de novo synthesis. FAs, then, can access the mitochondria according to their length; while short and medium-chain FAs (up to 12 carbon atoms) diffuse through the mitochondrial membrane, long-chain FAs (with 13-21 carbon atoms) are actively transported by the carnitine O-palmitoyl transferase (CPT) proteins, which are rate limiting enzymes for this pathway [10]. Previous work suggested that FAO is poorly utilized by EC cultures [4], however, under certain stress conditions such as glucose deprivation, FAO becomes a major source of energy [7]. While it is striking to note how cells can adapt and remodel their metabolism, the role of key FAO enzymes in the control of EC functions is still largely unclear.

Due to the complexity of the cell metabolome, global-scale metabolomic studies for in depth and quantitative analysis of metabolic fluxes are still challenging and computational models have provided invaluable help to better understand cell metabolism. Among them, the integrative metabolic analysis tool (iMAT), which integrates gene expression data with genome-scale metabolic network model (GSMM), has been successfully used to predict enzyme metabolic flux in several model systems and diseases [11, 12]. Since gene expression and protein levels do not always correlate, and because enzymes levels do not necessarily reflect their enzymatic activity or the flux of the reaction that they are involved in, iMAT uses expression data as cue for the likelihood, but not final determinant, of enzyme activity. Modern mass spectrometry (MS) technology and robust approaches for protein quantification, such as stable-isotope labeling with amino acids in cell culture (SILAC) [13] and advanced label-free algorithms [14], allow global comparative proteomic analysis and accurate measurements of protein and post-translational modification levels [15]. We reasoned that the integration of quantitative MS-proteomic data into GSMM could contribute to the study of cell metabolism. Moreover, metabolic changes trigger activation of protein kinases [16, 17] to rapidly remodel the intracellular signaling and enable cells to adapt to these sudden alterations. Protein phosphorylation therefore plays an important role in regulating cell response to metabolic alteration and may hide information on cellular pathways and functions controlled by specific metabolic activities. MS-based proteomic approaches therefore offer an additional opportunity to investigate in an unbiased manner the interplay between cell metabolism and cell function [18].

We have previously shown [19] that when human primary ECs are cultured for one day on the three dimensional matrix matrigel and assemble into a complex network, a simplified model which recapitulates some aspects of vascular network assembly in-vivo [20] the levels of metabolic enzymes are profoundly regulated. This result suggested an interplay between cell metabolism and EC behavior. Here we investigate further this aspect. Integrating label-free quantitative MS-proteomics, predictive metabolic modeling and metabolomics we discovered increased FAO when ECs are assembled into a fully formed network. Moreover, by inhibiting CPT1 pharmacologically, we elucidated that FAO is a central regulator of EC permeability in-vitro and blood vessel stability in-vivo. Thus proteomics significantly contributes to the study of cell metabolism and here we identified FAO as a promising target for therapeutic intervention for the control of pathological vascular permeability.

Experimental Procedures

Cells, reagents and treatments

Human umbilical vein endothelial cells (HUVECs) isolated from 2-5 umbilical cords were pooled and cultured in EGM-2 (Lonza, Basel, Switzerland). For the SILAC labelling, cells were grown for 3 passages (P) in custom EGM-2 without arginine and lysine (Lonza) supplemented with L-arginine and L-lysine (SILAC light) (Sigma-Aldrich, St. Louis, MO, USA), $^{13}C_6$ L-arginine and D_4 L-lysine (SILAC medium) or $^{13}C_6{}^{15}N_4$ L-arginine (SILAC heavy) and $^{13}C_6{}^{15}N_2$ L-lysine (heavy lysine) (Cambridge Isotope Laboratories, Tewksbury, MA, USA). BOECs were kindly provided by Dr. Maartje van den Biggelaar and cultured in EGM-2 medium 10% FBS. Cells were used between P2 and P6.

If not otherwise stated, after 2 h etomoxir treatment (15µg/ml) cells were treated or not with pyruvate (500µM) for 30 min followed by dichloroacetate (5mM) for 30 min before cells were used in experiments.

Etomoxir, oxfenicine, dichloroacetate, pyruvate, thrombin, VEGF and mouse anti-vinculin antibody were from Sigma-Aldrich; anti-CPT1A antibody (15184-1-AP) was from Protein Tech group (Chicago, IL, USA); anti-β-tubulin was from Santa Cruz Biotechnology (Dallas, TX, USA), anti-phospho ACACA was from Cell Signaling (Danvers, MA, USA); anti-mouse IRDye 700CW and anti-rabbit IRDye 800CW used for western blot were from LI-COR Biosciences (Lincoln, NE, USA). Matrigel and Cell recovery solution were from BD biosciences (Franklin Lakes, NJ, USA).

Matrigel assay

HUVECs were seeded and cultured on solidified Matrigel in EGM-2 medium with the indicated stimuli and harvested for MS analysis using Cell recovery solution according to manufacturer's instructions and as previously described [19]. Pictures were taken with Axiovert microscope and the tubule length measured with ImageJ software.

Sample preparation for proteomic analysis

HUVECs were lysed in 2% SDS, 100mM Tris-HCl pH 7.4 buffer.

Proteome Matrigel: Proteins were precipitated and solubilized in 8M urea, 75mM NaCl and 50mM TrisHCl. After reduction with dithiothreitol and alkylation with iodoacetamide, proteins were digested with trypsin. *Proteome etomoxir*: Light, medium and heavy SILAC-labeled cell lysates (~70 µg/sample) were mixed in equal amount, trypsin digested by filter-aided sample preparation method and 50 µg of peptides fractionated into six fractions using on-tip strong anion exchange chromatography [21].

Phosphoproteome: Light, medium and heavy SILAC-labeled cell lysates (~3 mg/sample) were mixed in equal amount, digested by filter-aided sample preparation method [22] and enriched for phosphorylated peptides using strong cation exchange chromatography followed by titanium dioxide enrichment [23] for phosphorylated peptides as previously described [24].

Digested peptides were de-salted with Empore-C_{18} StageTips [25], eluted in 80% acetonitrile (ACN), 0.5% acetic acid and stored at -80°C until MS analysis.

Proteomic MS analysis

Tryptic peptides were separated on 20 cm fused silica emitter (New Objective, Woburn, MA, USA) packed in-house with the reverse phase ReproSil-Pur C_{18}-AQ, 1.9 µm resin (Dr. Maisch, GmbH, Ammerbuch-Entringen, Germany) and analyzed on a LTQ-Orbitrap Elite (Thermo Fisher Scientific) coupled on-line with a nano-HPLC (Easy nLC, Thermo Fisher Scientific).

Proteome Matrigel: for each sample, ~2µg of digested peptides were eluted from reverse phase column with a flow of 200 nl/min in 190 min gradient, from 5% to 30% ACN in 0.5% acetic acid. For each time point three replicates were performed and each replicate was run at the MS twice.

Proteome etomoxir: for each fraction, half of the peptides were loaded onto reverse phase column and eluted with a flow of 200 in 190 min gradient, from 5% to 30% ACN in 0.5% acetic acid. Triplicate experiments were performed swapping SILAC labeling conditions.

Phosphoproteome: for each experiment, 10 fractions enriched for phosphorylated peptides were analyzed at the MS. Two third of each sample was loaded onto reverse phase column and eluted with a flow of 200

nl/min in 90 min gradient, from 5% to 30% ACN in 0.5% acetic acid. The remaining 1/3 was pooled into two fractions which were analyzed at the MS. Triplicate experiments were performed swapping SILAC labeling conditions.

MS spectra were acquired in the Orbitrap analyzer at a resolution of 120000 at 400 m/z, and a target value of 10^6 charges. High collision dissociation fragmentation of the 10 most intense ions was performed using a target value of 40000 charges and acquired in the Orbitrap at resolution 15000 at 400 m/z. Data were acquired with Xcalibur software. MS data were processed using the MaxQuant software [26] and searched with Andromeda search engine [27] against the human UniProt database (release-2012 01, 81,213 entries). An initial maximal mass deviation of 7 ppm and 20 ppm was required to search for precursor and fragment ions, respectively. Trypsin with full enzyme specificity and peptides with a minimum length of 7 amino acids were selected. Two missed cleavages were allowed. Oxidation (Met) and N-acetylation were set as variable modifications, as well as phospho(STY) for the phosphoproteome analysis, while Carbamidomethylation (Cys) as fixed modification. False discovery rate (FDR) of 1% was used for peptides, proteins and phosphosites identification. For the phosphosites, a minimum Andromeda phosphopeptides score of 40 was required, as previously described [28].

Proteomic data analysis

Proteome Matrigel: Peptides and proteins were quantified according to the MaxLFQ algorithm of MaxQuant [14] version 1.4.1.0. Only proteins uniquely identified with minimum 1 unique peptide and quantified in at least three MS runs were used for the analysis.

Proteome etomoxir: The relative quantification of the phosphorylation sites against their labeled counterpart was performed by MaxQuant [14] version 1.5.0.36. Only proteins identified with minimum 1 unique peptide and quantified with a minimum of two ratio counts were used for the analysis. Proteins were considered upregulated if the SILAC ratio was higher than 0.3 ($\log_2$ scale), which was more than one standard deviation from the mean of the all calculated ratios, in a minimum of two replicates.

Phosphoproteome: The relative quantification of the phosphorylation sites against their labeled counterpart was performed by MaxQuant [14] version 1.4.1.6. Only class I sites (= sites accurately localized with

localization probability > 0.75 and score difference > 5) were used for the analysis. Phosphorylation sites were considered upregulated if the SILAC ratio was higher than 0.4 (log_2 scale), which was more than one standard deviation from the mean of the all calculated ratios, in a minimum of two replicates. For the NetworKIN analysis [29], for each phosphorylation site only the predicted kinase with highest score was considered and we required a minimum networkin score of 1.5. Motif-X analysis was performed using standard parameters, significance of 0.000001 and IPI Human Proteome as background [30]. Predicted kinase activity was calculated by means of significantly overrepresented (Fisher test, with 2% FDR) kinase motifs (used "Motifs" column of Table S3 which was generated with Perseus software, based on Human Protein Reference Database [31]) within the 83 upregulated sites upon etomoxir treatment. The 83 sites were queried against the entire phospho-dataset.

Computational analysis using genome-scale metabolic modeling

Integration of Proteomics Data: Metabolic genes for which absolute protein abundance levels (LFQ) were measured in experiments were mapped to the human genome-scale metabolic model (GSMM) [32]. The mean (over 3 replicas) of protein abundance levels in each time point (i.e., 4h, 22h) were used to infer ternary presentation of the abundance levels using 'quartile' partitioning. This allowed for integrating 50% of the measured data, such that proteins in the top 25% quartile were labelled 1 (highly abundant), proteins in the down 25% quartile were labelled "-1" (lowly abundant) and the rest were labelled "0" (moderately abundant), in each time point. Based on the GSMM gene-reaction rules, i.e., the logical dependence of each reaction on the activity of the genes associated with it, we infer the ternary state at the reaction level. This ternary representation was used as "cues" (soft constraints) to perform iMAT [11] in each time point. To assess the permissible flux range (i.e., minimal and maximal flux) of each reaction we performed flux-variability analysis (FVA) around the optimal solution that maximizes the agreement between the predicted fluxes and the proteomic measurements. Then, we sampled the solution space using ACHR algorithm and estimated the average flux of each reaction. Fold-changes between 22h and 4h were derived based on the average fluxes.

The pathway enrichment analysis based on fold change reaction flux between 4h and 22h matrigel (in Table S2) was performed using the one dimension (1D) annotation enrichment analysis available in the Perseus software [33].

CPT1A Knockout Analysis: To simulate the effect of CPT1A inhibition at 22h we simulated the metabolic state using iMAT twice: once when the reactions associated with CPT1A were active at their maximal flux, and once when they were inhibited, carrying no flux. FVA and sampling (ACHR) of the solution space were performed. Based on the average fluxes of the reactions we estimated the fold-change following CPT1A inhibition as: fluxes when CPT1A was inactive/fluxes when CPT1A was active.

Sample preparation for metabolomic analysis

HUVECs were seeded on a solidified matrigel (six well plate, 200 µl/9.6 cm^2) in EGM-2 medium. After 3h, 22h and 30h, cells were washed with PBS, and medium replaced with 1 ml EGM-2, 11mM $^{13}C_6$ Glucose and 100µM $^{12}C_{16}$ palmitic acid or 11mM $^{12}C_6$ Glucose and 100µM $^{13}C_{16}$ palmitic acid. After 6h incubation at 37°C metabolites were extracted as follow from triplicate samples:

Extracellular: 20 µl of supernatant were mixed with 980 µl of cold methanol:ACN:water (5 volumes:3 volumes:2 volumes) extraction buffer, mixed (using a thermo-mixer) for 10 min at 4°C and spun 10 min at 16,100g at 4°C. Of the cleared supernatant, 800 µl were stored at -80°C until MS analysis.

Intracellular: cells were quickly washed with cold PBS and metabolites extracted upon incubation with ~250 µl of cold extraction buffer for 5 min at 4°C. Metabolites were then collected and mixed (using a thermo-mixer) for 10 min at 4°C and spun 10 min at 16,100g at 4°C. Of the cleared supernatant, 200 µl were stored at -80°C until MS analysis.

Metabolomics MS analysis

Metabolites were analyzed on an Exactive Orbitrap mass spectrometer (Thermo Fisher Scientific) coupled online with a Accela HPLC system (Thermo Fisher Scientific). The HPLC setup consisted of a ZIC-pHILIC column (150 x 2.1mm, 5µm, SeQuant, Merck KGaA), with a ZIC-pHILIC guard column (SeQuant, 20 x 2.1mm) and an initial mobile phase of 20% 20mM ammonium carbonate pH 9.4 and 80% acetonitrile. Of the

metabolites extracted from the cells and supernatant, 5µl were injected and separated over a 30 min mobile phase gradient, decreasing the acetonitrile content to 20%, at a flow rate of 100 µl/min. The total analysis time was 38 minutes. All metabolites were detected across a mass range of 75-1000 m/z at a resolution of 25,000, at 200m/z, with electrospray ionization and polarity switching to enable both positive and negative ions to be determined in the same run. Lock masses were used and the mass accuracy obtained for all metabolites was below 5ppm. Data were acquired with Xcalibur software.

Metabolomics data analysis

The peak areas (= measured intensity) of different metabolites were determined using LCquan software (Thermo Fisher Scientific) where metabolites were identified by the exact mass of the singly charged ion and by known retention time on the HPLC column. Commercial standards of all metabolites detected had been analyzed previously on the same LC-MS system. The ^{13}C labelling patterns were determined by measuring peak areas for the accurate mass of each isotopologue of many metabolites. The measure intensities of the intracellular metabolites were normalized to the amount of unlabeled intracellular arginine and phenylalanine.

SiRNA

For matrigel and Ca^{2+} imaging experiments: the day before transfection, HUVECs were seeded in six-well plates at a concentration of $2x10^5$ cells/well. Transfection of the siRNA duplexes was performed with Oligofectamine according to the manufacturer's protocol (Invitrogen, Carlsbad, CA, USA). Briefly, cells were transfected with 375 pmol of non-targeting (Dharmacon- GE Healthcare) or luciferase-targeting siRNA as control, or pool or single Stealth Select RNAi for CPT1A: iCPT1A#1: CCACCAAGAUCUGGAUGGGUAUGGU; SiCPT1A#2: GGACCGGGAGGAAAUCAAACCAAUU (Invitrogen). After 48h since the transfection, cells were used for experiments. For the fibrin in-vitro angiogenesis assay and TEER, HUVECs were transfected using the Amaxa Kit (Lonza) according to manufacturer's instruction. After 48h from transfection, cells were used for experiments.

Western blot analysis

HUVECs were lysed in 2% SDS in 100mM Tris HCl pH 7.4. Proteins were separated on NuPAGE 4-12% Bis-Tris gel (Invitrogen) and transferred to PVDF membrane (Millipore). The blots were probed with

primary antibodies. Multi-color signals were detected after incubation with secondary antibodies using Odyssey CLx instrument (LI-COR Biosciences). Signals were quantified using Image Studio lite software (LI-COR Biosciences).

Cell proliferation and cell death

Cell proliferation and cell death were assessed using Click-iT EdU kit and Annexin V kit (Invitrogen) according to manufacturer's protocol. Briefly, HUVECs were seeded at a concentration of 160 cells/mm^2 in EGM-2 medium with the indicated concentration of stimuli. After 20 hours, cells were harvested (for EdU incorporation, EdU was added 1.5-2 hours before cell harvesting), stained following manufacturer's recommendations and analyzed at the FACS or by immunofluorescence (siCPT1A experiment).

3D Fibrin assay

Collagen-coated beads (Cytodex 3, Sigma- Aldrich) were covered with HUVECs, embedded into fibrin gel as previously described [34] and cultured for two days in EGM-2 medium in the presence of the indicated stimuli.

Fatty acid oxidation measurement

[1-^{14}C] palmitic acid (Perkin Elmer, Waltham, MA, USA) or palmitic acid (Sigma) was resuspended in α-cyclodextrin (Sigma, 20 mg/ml in 10 mM Tris pH 8) to obtain a 12 µCi/ml solution. HUVECs grown fully confluent in 35 mm dish were incubated with the indicated stimuli for the indicated time and then 1.2 µCi/ml [1-^{14}C] palmitic acid was added for 4h in the presence or absence of stimuli. For the siRNA study, transfected HUVECs were seeded the day before the assay then incubated with [1-^{14}C] palmitic acid for 4h. Afetr 4h, the lids of the cell culture plates were replaced with whatman paper and saturated with 5M NaOH. Addition of 200 µl perchloric acid triggered the release of CO_2 which was captured in the whatman paper and analyzed in a scintillation counter (MicroBeta TriLux, Perkin Elmer). For the acid soluble metabolites, 1ml of medium was recovered, incubated with 200 µl 4N KOH, 30 min at 60°C to hydrolyze the acyl-CoA esters and acidified with 300 µl 1M $NaC_2H_3O_2$ and 200 µl 3N H_2SO_4. After spinning, 300 µl of the supernatant were mixed with 5 ml of a 2:1 solution of chloroform:methanol to allow phase separation. The upper aqueous phase, where the acid soluble metabolites (ASM) coming from palmitic acid oxidation are

dissolved, was incubated with scintillation fluid and analyzed in a scintillation counter. The values obtained were normalized by cell number.

Oxygen consumption rate measurement

XF96 plates (Seahorse Bioscience, North Billerica, MA, US) were coated with gelatin and $2.5x10^4$ HUVECs were seeded in EGM-2 medium. The day after, the medium was replaced with unbuffered assay medium (Seahorse Bioscience) with 0.5% FBS and 5mM glucose, pH 7.4 and cells placed at 37°C in CO_2-free incubator for 1 h. Basal oxygen-consumption rate (OCR) was recorded using the XF^{e}96 analyzer. Pyruvate and dichloroacetate were added in subsequent injections. Each measurement cycle consisted of 3 min mixing and 3 min measuring. At the end of the experiment 1 μM antimycin A was added in order to measure mitochondria-independent oxygen consumption. Mitochondria-dependent OCR is plotted.

ATP, cell proliferation and cell death assays

ATP, cell proliferation and death were assessed using ATP determination kit, Click-iT EdU kit and Annexin V kit (Invitrogen) according to manufacturer instruction. For the ATP assay, HUVECs were harvested and counted, then lysed in H_2O (1ml/$1x10^6$ cells) and boiled for 10 min. After spinning, the supernatants were assessed with the ATP determination kit.

Calcium imaging

Confluent HUVECs were grown in EGM-2 medium on glass gelatin-coated coverslips for 4 days. Cells were next loaded (45 min at 37°C) with 2 μM Fura-2 AM (Invitrogen), for ratiometric cytosolic Ca^{2+} $[Ca^{2+}]i$ measurements as previously described [35]. During the experiments cells were continuously bathed with a microperfusion system. Fluorescence measurements were made using a Polychrome V spectrofluorometer (TILL Photonics, Munich BioRegio, Germany) attached to a Nikon TE-2000-S (Nikon Corporation, Melville, NY, USA) microscope and Metafluor Imaging System (Molecular Devices, Sunnyvale, CA, USA) for image acquisition using 3-second intervals. During experiments, cells were maintained in standard extracellular solution of the following composition: 145mM NaCl, 5mM KCl, 2mM $CaCl_2$, 1mM $MgCl_2$, 10mM N-(2-hydroxyethyl)-piperazine-N'-ethanesufonic acid (HEPES), 10mM glucose (NaOH to pH 7.35). Cells were continuously bathed with a microperfusion system. Each fluorescence trace (340/380 nm ratio)

represents one region of interest (ROI) corresponding to cells in the chosen image field. Appropriate controls were performed with vehicles (dH_2O). Number of oscillations was determined by IgorPro software (WaveMetrics Inc, Tigard, OR, USA) by multipeak fitting analysis function and expressed as number of oscillation/10 min. The oscillation number is expressed as mean ± SEM of at least 3 pooled experiments.

Permeability assays

In-vitro TEER: Cells were plated in EGM-2 on 12 mm gelatin-coated transwell, 0.4µm pore size polyester membrane, (Costar, NY USA) and grown tightly confluent. TEER was measured using a "chopstick" STX2 electrode connected to an EVOM2 voltohmmeter (World Precisions Instruments). TEER has been measured also in wells without cells and values have been used as background and subtracted to the values measured in the presence of cells. The normalized were used to calculate the % reported in the Figures.

In-vivo ear permeability: This assay was performed as previously described with minor modifications [36]. FVB/n wild type mice (The Jackson Laboratory) were pretreated with 4mg/Kg pyrilamine maleate salt (Sigma Aldrich) at least 30 minutes before Evans blue injection, in order to block histamine release. Next, 100µl/mouse of Evans blue (Sigma Aldrich) diluted 0.5% in saline solution was intravenously injected. After two hours, mice were randomized and subdivided into groups of 4 mice each. Different drugs were injected intradermally with the following amounts: a) 100ng, 200ng, 1µg and 2µg of etomoxir; b) 1µg, 2µg, 5µg and 10µg of oxfenicine; c) 100ng etomoxir combined with 500ng pyruvate and 5µg dichloroacetate; d) gadolinium 100µM was co-injected with 500ng of etomoxir; e) saline solution was used as negative control. Ten minutes after drug administration, the ears were excised and photographed with a stereomicroscope connected to a camera by means the Image ProPlus analyzer software. The amount of Evans blue extravasation through the vessels was quantified with ImageJ software. Mice were housed under the approval and the institutional guidelines governing the care of laboratory mice of the University of Torino Committee on Animal Research and in compliance with National and International laws and policies.

Statistical analysis

Unless indicated otherwise, p values have been calculated using a two-tailed unpaired t-test using GraphPad Prism software. $*p < 0.05$; $**p < 0.01$; $***p < 0.001$;$****p < 0.0001$.

The .raw MS files and search/identification files obtained with MaxQuant have been deposited in the ProteomeXchange Consortium (http://proteomecentral.proteomexchange.org/cgi/GetDataset) via the PRIDE partner repository with the dataset identifier PXD001186 (Username: reviewer00376@ebi.ac.uk; Password: FmscZ32o; to access visit http://tinyurl.com/m9hy5lv).

Results

ECs remodel their metabolism upon morphogenesis.

To identify metabolic pathways potentially involved in controlling EC functions, we used iMAT to integrate time-resolved proteomic data of human umbilical vein endothelial cells (HUVECs, referred to as ECs throughout the Results section) grown on matrigel with GSMM (Figure 1A). ECs were used as model because they are well-characterized primary endothelial cells, and relatively easy to isolate and culture. Using high-resolution MS and label-free quantification algorithm [14], we measured the proteome of ECs grown on matrigel for 4h (early matrigel), and 22h (late matrigel) (Table S1), because at these time points cells have a distinct phenotype. At 4h cells are spread, proliferative and have started forming a network, whereas at 22h cells are elongated, low proliferative and have assembled into a fully formed complex network (Figure 1A,B). Proteomic changes between these two time points pinpointed proteins involved in vessel maturation, including increasing levels of cell-cell adhesion proteins ve-cadherin (CDH5) and junction plakoglobin (JUP), the tyrosine kinase receptor TIE1, and the endothelial nitric oxide synthase (NOS3) [37, 38 , 39](Figure 1C). For each time point, 359 metabolic enzymes (according to RECON [32], Table S1) were quantified by MS of which 170 were defined as highly or lowly abundant and used to build up a model which predicts metabolic fluxes (Table S2). We reasoned that metabolic differences between 4h and 22h may hint at pathways relevant for the regulation of EC functions. Pathway enrichment analysis based on fold change reaction flux between early and late matrigel highlighted FAO in peroxisome, the organelle where very-long-chain FAs can be oxidized into short-chain FAs and released into the cytosol, as the most upregulated pathway when the network was fully assembled, and TCAc as the most downregulated (Table

S2). Detailed investigation of single reaction flux of FAs and glucose metabolism pinpointed increased transport into the mitochondria of long-chain FAs, such as the palmitoyl-CoA via CPT1 and CPT2, higher diffusion into the mitochondria of short-chain FAs, such as the octanoyl-CoA which can be generated by oxidation of very long fatty acids, and increased flux of acyl-CoA dehydrogenases (ACADM and ACADS)-catalyzed reactions of the FAO pathway (Figure 1D,E). Conversely, decreased flux was predicted for reactions of the glycolysis pathway catalyzed by hexokinase (HK), phosphofructokinase (PFK), aldolase (ALDO) and lactate dehydrogenase (LDH), and for the pyruvate dehydrogenase (PDH), which generates acetyl-CoA from pyruvate thus linking glycolysis to the TCAc (Figure 1D,E). To verify our model, we performed a MS stable isotope-based tracing metabolomic analysis using $^{13}C_{16}$-labeled palmitate and $^{13}C_{6}$-labeled glucose. This approach measures the metabolic activity of the cells by calculating the amount of ^{13}C-labeled palmitate and glucose that cells convert into other metabolites. After early time culture on matrigel, the ^{13}C-labeled palmitoyl-carnitine, whose formation is catalyzed by CPT1A from the $^{13}C_{16}$-labeled-palmitate, was barely detected by MS while consistently quantified when the network was fully formed after 22h and 30h. Similar results were observed for the ^{13}C-labeled aspartate which is generated from TCAc intermediates (Figure 1F and Figure S1A). Conversely, ECs in the fully formed network decreased ^{13}C-labeled glucose consumption for glycolysis, as shown by more than 50% reduction of ^{13}C-labeled secreted lactate and intermediates of glycolysis and TCAc (Figure 1G). To investigate that the above metabolic changes were specific for the matrigel system, and not an effect of general cell adhesion mechanism or adaptation of the cells to the cell culture, we used ^{14}C-labelled palmitate and measured FAO in ECs grown on culture dish for 4h and 22h. In contrast to the results obtained in the matrigel assay, ECs showed a significant reduction of FAO at 22h compared to 4h (Figure S1B). Moreover, to assess that changes in FAO were not just a reflection of the proliferative status of the cells, we measured FAO in highly and low proliferative cells (Figure S1C). This showed that low proliferating ECs had lower FAO compared to highly proliferative ones (Figure S1D). These results demonstrate the validity of our predictive metabolic model and indicate that, when assembled into a fully formed network, ECs enhance FAO while reducing glycolysis.

CPT1A inhibition impairs EC proliferation, network integrity and sprouting.

To investigate the functional role of FAO in ECs, we first exploited the predictive metabolic model and explored whether blocking FAO would alter metabolic fluxes. To this aim, we inhibited CPT1A as it is the rate limiting enzyme in FAO and its levels were increased after 24h of ECs culture on matrigel (Figure 1H). By inactivating CPT1A in the predictive metabolic model built up using the late matrigel proteomic data, a substantial decrease in cellular ATP levels was predicted (reactions 3789, 3791 and 3795 were amongst the most downregulated ones, Table S2). These results suggest that FAO is a key factor in ECs and, based on these observations, we further investigated the role of FAO in ECs by targeting CPT1A. By inhibiting CPT1A either pharmacologically with etomoxir, a well characterized drug which targets CPT1 [40], or siRNA specific for CPT1A (Figure S2A), FAO was substantially decreased (Figure 2A,B). Since 15 µg/ml etomoxir showed maximum FAO inhibition (Figure 2A), we used this concentration for the following experiments. A significant decrease in cell proliferation was measured after 24h treatment with etomoxir and when CPT1A was silenced with siRNA, but not after 4h etomoxir treatment (Figure 2C,D and Figure S2B). These changes had minor effects on cell death. While no effects were measured upon 24h inhibition of CPT1A with etomoxir (Figure 2E), a small but significant increase in cell death (by means of number of cells positive for both, propidium iodide and annexin V) was measured in cells where CPT1A was silenced for 48h (Figure 2F and Figure S2C). Next we tested the effects of CPT1A inhibition on EC morphogenesis. When we grew ECs on matrigel for 24h in the presence of etomoxir or when cells were silenced for CPT1A (Figure S2D), a significant reduction (30-40%) of the network integrity was measured (Figure 2G,H and Figure S2E,F). To exclude that this effect was exclusively due to a reduction in cell proliferation, we performed the matrigel assay in the presence of mitomycin C, a DNA cross-linker which inhibits cell proliferation [4] (Figure S2G). This experiment showed that etomoxir, but not mitomycin C treatment significantly reduced network integrity (Figure S2H). Significant defects were also observed using a three-dimension (3D) angiogenesis assay of ECs embedded into fibrin gel for two days. EC sprouting was significantly reduced in the presence of etomoxir (Figure 2I,J and Figure S2I,J). Hence, reduced CPT1A activity impairs key EC functions.

In ECs FAO supports TCAc and ATP production through oxidative phosphorylation

FAO produces intermediates for the TCAc, which is a central hub for energy production, and our metabolic model predicted a sizable contribution of CPT1A to maintain ATP levels. Therefore, we measured the effects of CPT1A inhibition on cellular ATP levels. Due to the limited number and accessibility of ECs when grown on matrigel, to investigate the role of FAO in ECs, we performed experiments using EC cultured in a monolayer. Acute (3h) etomoxir treatment of ECs reduced total ATP levels of ~10% (Figure 3A). This result is in line with the previous literature which shows that ~80% of ATP is derived from glycolysis and the remaining from glucose, glutamine and fatty acids oxidation [4]. When we replenished the TCAc of the etomoxir-treated cells with dichloroacetate (DCA), a drug that activates the pyruvate dehydrogenase A (PDHA1) by inhibiting the pyruvate dehydrogenase kinase (Figure 3B), and pyruvate, the substrate that PDHA1 uses to generate acetyl-CoA, the ATP levels were restored almost to the levels of control cells (Figure 3A). Consistently, inhibition of CPT1A induced a significant decrease in oxygen consumption rate (OCR) and OCR levels raised with the replenishment of the TCAc with DCA and pyruvate (Figure 3C,D). Similar results were obtained upon acute inhibition of FAO with oxfenicine, which is another known inhibitor of CPT1 [10, 40] (Figure S2K-M). Thus, CPT1A activity fuels TCAc and ATP production through oxidative phosphorylation.

Phosphoproteomics unveils that CPT1A inhibition in ECs affects calcium-dependent signaling

To further investigate CPT1A functions, we used unbiased global phosphoproteomics and assessed the impact of metabolic alterations induced by acute CPT1A inhibition on EC signaling. Using a triple-SILAC approach, we measured phosphoproteomic changes after 2h etomoxir treatment and replenishment of the TCAc with pyruvate and DCA (Figure 4A). In triplicate experiments more than nine thousand accurately localized (with a median localization probability [41] of 0.999) phosphorylation sites were quantified. Of those, 83, which belong to 62 proteins, increased phosphorylation levels upon etomoxir treatment compared to non-treated control cells (Tables S3-S4). Based on Uniprot annotation, the regulated phosphoproteins included metabolic enzymes, kinases, and proteins involved in the regulation of transcription, translation, protein trafficking and cytoskeleton. Additionally, we exploited the phosphoproteomic data to look for kinases responsible for the deregulated phospho-signaling. First we evaluated that the phosphoproteomic changes were the results of altered kinase activity and not total protein levels. By measuring the cell

proteome to a depth of almost 5000 proteins, only ten proteins increased levels upon etomoxir stimulation and this subset did not include any of the proteins with regulated phosphorylation sites (Figure 4A and Table S5). Thus, etomoxir-induced phosphorylations are mostly the result of altered phospho-signaling. Next we used NetworKIN [29], a platform which combines sequence specificity, such as known linear kinase motifs surrounding the regulated phosphorylation site, and cellular context, such as physical and functional protein-protein interactions, to identify the likely kinases responsible for the regulation of the 83 sites. This analysis predicted highest number of substrates (12) for the calcium-calmodulin dependent kinase II (CamKII) group (Figure 4B, Table S6). Linear kinase motif analysis with Motif-X strengthened this prediction and pinpointed the CamKII motif, which has an arginine in position -3 of the phosphorylated site (R--Sp), as significantly over-represented among the 83 sites (Figure 4C). Similarly, CamKII was predicted active when performing a kinase motif (according to known motifs in the HPRD database) enrichment analysis using the MaxQuant module Perseus (Figure S3A). This analysis further pinpointed highly significant enrichment for the AMP-activated protein kinase (AMPK). AMPK can be directly phosphorylated and activated by CamKII [17, 42], and NetworKIN predicted two AMPK substrates, of which one is the known Ser80 of ACACA [43](Figure S3B-D). We verified by western blot analysis that ACACA increases phosphorylation upon etomoxir treatment, and further showed that in the presence of gadolinium (Gd^{3+}), which inhibits extracellular Ca^{2+} entry [44], etomoxir-induced ACACA phosphorylation was reduced (Figure S3E). Finally, detailed literature- and database-based investigation of the etomoxir-regulated phosphorylation sites pinpointed several sites on proteins related to Ca^{2+} signaling, such as the Ca^{2+} sensor STIM1 [45], the sodium/hydrogen exchanger SLC9A1, the adherens junction protein CTNNA1, the phosphatidylinositol transfer protein PITPNM2 and the GTPase-activating protein ARGHAP17 (Figure 4D). Of note, some of the sites decreased phosphorylation levels upon pyruvate and DCA treatment (Figure 4D).

All together, these data indicate that inhibition of FAO with etomoxir activates Ca^{2+}/CamKII/AMPK pathway, and suggest that CPT1A activity is required to maintain Ca^{2+} homeostasis.

Acute CPT1A inhibition alters calcium homeostasis in ECs

Measuring single-cell cytoplasmic Ca^{2+} dynamics in ECs showed that inhibition of CPT1A with etomoxir induced a striking increase (>3 fold) of Ca^{2+} oscillation frequency within minutes (Figure 5A,B). Notably,

this alteration was fully inhibited by blocking extracellular Ca^{2+} entry with Gd^{3+} or replenishing the TCAc with pyruvate and DCA (Figure 5B and Figure S4A). Demonstrating that etomoxir-induced Ca^{2+} oscillations were dependent on CPT1A inhibition, ECs silenced for CPT1A did not increase Ca^{2+} oscillations frequency when treated with etomoxir (Figure S4B,C). Moreover, similar to etomoxir, ECs treated with oxfenicine increased cytosolic Ca^{2+} oscillations, and these decreased by replenishing the TCAc (Figure 5C,D). Together these results demonstrate that in ECs CPT1A activity maintains Ca^{2+} homeostasis.

CPT1A inhibition increases EC permeability

Calcium is a key regulator of endothelial permeability [46]. Therefore, to explore if the measured Ca^{2+} alteration induced by inhibiting CPT1A had an impact on EC functions, we measured the permeability of an EC monolayer by means of trans-endothelial electrical resistance (TEER), and compared it to known inducers of hyperpermeability, thrombin and vascular endothelial growth factor (VEGF). TEER of etomoxir-treated cells showed a prominent decrease (30-40%) of resistance (= increase permeability) compared to control cells (Figure 6A). Similarly, increased permeability was measured in ECs upon 24h treatment with etomoxir or when CPT1A was silenced with siRNA (Figure S4D,E and Figure S2D). This effect was around half of that induced by 1 unit/ml of thrombin (~60% decrease) and similar to 1nM VEGF treatment (~40% decrease) (Figure S4F,G). Confirming that the above effect was driven by Ca^{2+}, ECs treated with Gd^{3+} did not increase permeability when treated with etomoxir (Figure 6A). We further exploited the TEER assay to determine whether replenishing the TCAc of etomoxir-treated ECs, which we have shown to block aberrant Ca^{2+} oscillations (Figure 5A,B), would reduce hyperpermeability. Figure 6B shows that pyruvate and DCA treatment restored etomoxir-induced increased permeability to the levels of control cells. Similar results were obtained using blood outgrowth endothelial cells (BOECs), another model of human primary endothelial cell which is derived from peripheral blood [24, 47](Figure 6C), and when CPT1 activity was inhibited with oxfenicine (Figure 6D). Hence, impaired Ca^{2+} homeostasis in CPT1-inhibited cells induces hyperpermeability. Finally, we determined if the increased permeability was dependent on the contribution of FAO to oxidative phosphorylation. To this aim, we used oligomycin, a drug which inhibits oxidative phosphorylation by blocking the ATP synthase. Similar to CPT1A inhibition, ECs treated with oligomycin

had a significantly reduced TEER. Moreover, oligomycin blocked the recovery of the hyperpermeability induced by DCA and pyruvate in etomoxir-treated ECs (Figure 6E).

CPT1A inhibition increases blood vessel leakage in-vivo

To assess the relevance of our findings also in an in-vivo context, we investigated the effects of the acute inhibition of CPT1A on vascular permeability. To this aim we used an established Evans blue-based permeability assay of mature blood vessels [36] and measured the leakage of blood vessels in the mouse ear upon intradermal injection of vehicle, etomoxir or oxfenicine. We chose this system because it allows minimizing indirect heart effects that can be induced by systemic injection of the two drugs [40]. Both etomoxir and oxfenicine induced a dose-dependent increased leakage of Evans blue (Figure 7A,B and Figure S5A,B). Notably, the effects of etomoxir were significantly reduced when co-injected with Gd^{3+} and abrogated with pyruvate and DCA (Figure 7C-F and Figure S5C,D). Mirroring the results observed in-vitro, pharmacological inhibition of CPT1A impairs vascular barrier function and this process is dependent on Ca^{2+} and TCAc activity (Figure 7G).

Discussion

In this work we built up the first predictive model of metabolic fluxes based on high-resolution quantitative proteomic data which unveiled that HUVECs increase FAO and decrease glycolysis when assembled into a fully formed network. While it has been reported that loss of the rate-limiting enzyme for glycolysis, PFKFB3, impairs EC proliferation and migration [4], so far there has been no evidence of endothelial functions altered by blockage of the FAO rate-limiting enzyme CPT1A. By means of established drugs that target CPT1A, gene silencing and global phosphoproteomics, we demonstrate that FAO sustains oxidative phosphorylation and maintains Ca^{2+} homeostasis, and that this is required to maintain adequate permeability of ECs in-vitro and established mouse blood vessels in-vivo.

iMAT is a powerful computational tool to predict human cellular metabolic fluxes integrating GSMM with gene expression data [11, 12]; here we show that this analysis can be successfully extended to the use of protein levels accurately measured by MS-proteomics. We have validated some of the predictions identified in our model, such as increased CPT1A activity and decreased funneling of glucose into glycolysis in

HUVECs assembled into a fully formed network. Moreover, we provide the full list of predicted metabolic reaction fluxes, as resource of other metabolic processes potentially involved in regulating EC behavior to be further investigated.

It has been previously shown that ECs preferentially use glucose as energy source, have modest mitochondria content, and generate only a small amount of energy through mitochondrial metabolism [4, 48]. Accordingly, in our MS metabolomic analysis we have identified only a limited subset of metabolites generated from ^{13}C-labelled palmitate. However, these were reliably quantified and led to discover that ECs increase FAO in conditions other than energetic stress [7]. While future work is needed to address if changes occurring when ECs are assembled into a fully-formed network in-vitro occur also during the maturation process of newly formed blood vessels in-vivo, our work demonstrates that FAO plays a key role in ECs because acute and prolonged CPT1A inhibition impairs several cellular functions. To identify the role of FAO in ECs, we focused on the effects of acute pharmacological inhibition of CPT1A. This approach allows dynamic manipulation and measurement of cell metabolism and signaling, and identifies initial events that lead to the altered EC phenotypes upon prolonged CPT1A inhibition. Of note, etomoxir and oxfenicine are used in clinics or preclinical trials [10], thus extending the relevance of our study to clinical context.

Phosphorylations are dynamic and reversible regulators of protein functions and we reasoned that phosphoproteomics would be excellent to investigate the signaling altered upon short-time FAO inhibition and provide hints on the functional role of CPT1A. This approach pinpointed alterations of the Ca^{2+}/CamKII/AMPK pathway. Calcium is a master regulator of cellular signaling and functions, and abnormal Ca^{2+} homeostasis can determine pathological states [49]. In the vascular context, Ca^{2+} homeostasis is crucial to maintain the barrier function of the blood vessels, and increased intracellular Ca^{2+} in ECs increases cell permeability [46]. For these reasons, we focused our attention on Ca^{2+} and demonstrate that CPT1A activity maintains Ca^{2+} homeostasis and EC permeability. Furthermore, we show that this occurs through the function of CPT1A to fuel TCAc and oxidative phosphorylation (Figure 7G). Thus, our work provides the first link between FAO and Ca^{2+} signaling. However, the detailed mechanism has still to be elucidated. Intriguingly, mitochondria regulate Ca^{2+} homeostasis by buffering cytosolic Ca^{2+} [50] and ECs can store up to 25% of the total cellular Ca^{2+} in the mitochondria [51]. It is therefore tempting to hypothesize

that the altered mitochondrial activity (reduced ATP levels and OCR) induced by FAO inhibition may affect the capability of the mitochondria to buffer Ca^{2+} and that this activates Ca^{2+}-signaling. Another interesting question to be addressed in the future is if the Ca^{2+}/CamKII/AMPK pathway is a functional driver of EC and vascular hyperpermeability observed upon CPT1A inhibition. In support of this hypothesis, it has been previously shown that increased EC permeability in response to thrombin [52] and VEGF [42] is induced through Ca^{2+}/CamKII/AMPK pathway. Moreover, when we compared etomoxir- with thrombin-driven phospho-signaling, which we have recently measured using a similar MS-proteomic approach [24], we observed that more than 50% of the phosphosites upregulated by etomoxir increased phosphorylation levels also upon thrombin stimulation (Table S3). These included proteins involved in Ca^{2+} signaling, such as STIM1 [45], SLC9A1 and ACACA. Finally, our dataset is a potential resource for the identification of other kinases (Figure 4B) and detailed molecular mechanisms (Table S3) that determine the phenotype of FAO-inhibited ECs.

In conclusion, our work highlights the power of using MS-proteomics and metabolic modeling to better understand cell metabolism and unravel its interplay with cell behavior. Here we revealed a central role for CPT1A in ECs. Finally, our results imply that inducing mitochondrial metabolism, including FAO, for example using available drugs such as DCA, could be a promising strategy to act directly on ECs and counteract permeability defects observed in diseases such as cancer, thrombosis and atherosclerosis, and trigger vascular normalization. This study opens therefore new exciting perspectives for the study of FAO in ECs in pathophysiological conditions.

References

1. Goddard, L.M., and Iruela-Arispe, M.L. (2013). Cellular and molecular regulation of vascular permeability. Thromb Haemost *109*, 407-415.
2. Borissoff, J.I., Spronk, H.M., Heeneman, S., and ten Cate, H. (2009). Is thrombin a key player in the 'coagulation-atherogenesis' maze? Cardiovasc Res *82*, 392-403.
3. Jain, R.K. (2005). Normalization of tumor vasculature: an emerging concept in antiangiogenic therapy. Science (New York, N.Y *307*, 58-62.
4. De Bock, K., Georgiadou, M., Schoors, S., Kuchnio, A., Wong, B.W., Cantelmo, A.R., Quaegebeur, A., Ghesquiere, B., Cauwenberghs, S., Eelen, G., et al. (2013). Role of PFKFB3-driven glycolysis in vessel sprouting. Cell *154*, 651-663.

5. Spolarics, Z., Lang, C.H., Bagby, G.J., and Spitzer, J.J. (1991). Glutamine and fatty acid oxidation are the main sources of energy for Kupffer and endothelial cells. Am J Physiol *261*, G185-190.
6. Leighton, B., Curi, R., Hussein, A., and Newsholme, E.A. (1987). Maximum activities of some key enzymes of glycolysis, glutaminolysis, Krebs cycle and fatty acid utilization in bovine pulmonary endothelial cells. FEBS Lett *225*, 93-96.
7. Dagher, Z., Ruderman, N., Tornheim, K., and Ido, Y. (2001). Acute regulation of fatty acid oxidation and amp-activated protein kinase in human umbilical vein endothelial cells. Circulation research *88*, 1276-1282.
8. Schoors, S., De Bock, K., Cantelmo, A.R., Georgiadou, M., Ghesquiere, B., Cauwenberghs, S., Kuchnio, A., Wong, B.W., Quaegebeur, A., Goveia, J., et al. (2014). Partial and transient reduction of glycolysis by PFKFB3 blockade reduces pathological angiogenesis. Cell Metab *19*, 37-48.
9. Sawada, N., Jiang, A., Takizawa, F., Safdar, A., Manika, A., Tesmenitsky, Y., Kang, K.T., Bischoff, J., Kalwa, H., Sartoretto, J.L., et al. (2014). Endothelial PGC-1alpha mediates vascular dysfunction in diabetes. Cell Metab *19*, 246-258.
10. Carracedo, A., Cantley, L.C., and Pandolfi, P.P. (2013). Cancer metabolism: fatty acid oxidation in the limelight. Nat Rev Cancer *13*, 227-232.
11. Shlomi, T., Cabili, M.N., Herrgard, M.J., Palsson, B.O., and Ruppin, E. (2008). Network-based prediction of human tissue-specific metabolism. Nat Biotechnol *26*, 1003-1010.
12. Jerby, L., and Ruppin, E. (2012). Predicting drug targets and biomarkers of cancer via genome-scale metabolic modeling. Clin Cancer Res *18*, 5572-5584.
13. Ong, S.E., Blagoev, B., Kratchmarova, I., Kristensen, D.B., Steen, H., Pandey, A., and Mann, M. (2002). Stable isotope labeling by amino acids in cell culture, SILAC, as a simple and accurate approach to expression proteomics. Mol Cell Proteomics *1*, 376-386.
14. Cox, J., Hein, M.Y., Luber, C.A., Paron, I., Nagaraj, N., and Mann, M. (2014). MaxLFQ allows accurate proteome-wide label-free quantification by delayed normalization and maximal peptide ratio extraction. Mol Cell Proteomics.
15. Lamond, A.I., Uhlen, M., Horning, S., Makarov, A., Robinson, C.V., Serrano, L., Hartl, F.U., Baumeister, W., Werenskiold, A.K., Andersen, J.S., et al. (2012). Advancing cell biology through proteomics in space and time (PROSPECTS). Mol Cell Proteomics *11*, O112 017731.
16. Sengupta, S., Peterson, T.R., and Sabatini, D.M. (2010). Regulation of the mTOR complex 1 pathway by nutrients, growth factors, and stress. Mol Cell *40*, 310-322.
17. Hardie, D.G. (2011). AMP-activated protein kinase: an energy sensor that regulates all aspects of cell function. Genes Dev *25*, 1895-1908.
18. Reid, S., Hernandez-Fernaud, J.R., and Zanivan, S. (2014). In vivo quantitative proteomics for the study of oncometabolism. Methods Enzymol *543*, 235-259.
19. Zanivan, S., Maione, F., Hein, M.Y., Hernandez-Fernaud, J.R., Ostasiewicz, P., Giraudo, E., and Mann, M. (2013). SILAC-based proteomics of human primary endothelial cell morphogenesis unveils tumor angiogenic markers. Mol Cell Proteomics *12*, 3599-3611.
20. Arnaoutova, I., George, J., Kleinman, H.K., and Benton, G. (2009). The endothelial cell tube formation assay on basement membrane turns 20: state of the science and the art. Angiogenesis *12*, 267-274.
21. Wisniewski, J.R., Zougman, A., and Mann, M. (2009). Combination of FASP and StageTip-based fractionation allows in-depth analysis of the hippocampal membrane proteome. J Proteome Res *8*, 5674-5678.
22. Wisniewski, J.R., Zougman, A., Nagaraj, N., and Mann, M. (2009). Universal sample preparation method for proteome analysis. Nature methods *6*, 359-362.
23. Larsen, M.R., Thingholm, T.E., Jensen, O.N., Roepstorff, P., and Jorgensen, T.J. (2005). Highly selective enrichment of phosphorylated peptides from peptide mixtures using titanium dioxide microcolumns. Mol Cell Proteomics *4*, 873-886.
24. van den Biggelaar, M., Hernandez-Fernaud, J.R., van den Eshof, B.L., Neilson, L.J., Meijer, A.B., Mertens, K., and Zanivan, S. (2014). Quantitative phosphoproteomics unveils temporal dynamics of thrombin signaling in human endothelial cells. Blood *123*, e22-36.
25. Rappsilber, J., Ishihama, Y., and Mann, M. (2003). Stop and go extraction tips for matrix-assisted laser desorption/ionization, nanoelectrospray, and LC/MS sample pretreatment in proteomics. Analytical chemistry *75*, 663-670.

26. Cox, J., and Mann, M. (2008). MaxQuant enables high peptide identification rates, individualized p.p.b.-range mass accuracies and proteome-wide protein quantification. Nat Biotechnol *26*, 1367-1372.
27. Cox, J., Neuhauser, N., Michalski, A., Scheltema, R.A., Olsen, J.V., and Mann, M. (2011). Andromeda - a peptide search engine integrated into the MaxQuant environment. J Proteome Res.
28. Sharma, K., D'Souza, R.C., Tyanova, S., Schaab, C., Wisniewski, J.R., Cox, J., and Mann, M. (2014). Ultradeep human phosphoproteome reveals a distinct regulatory nature of tyr and ser/thr-based signaling. Cell Rep *8*, 1583-1594.
29. Horn, H., Schoof, E.M., Kim, J., Robin, X., Miller, M.L., Diella, F., Palma, A., Cesareni, G., Jensen, L.J., and Linding, R. (2014). KinomeXplorer: an integrated platform for kinome biology studies. Nature methods *11*, 603-604.
30. Schwartz, D., and Gygi, S.P. (2005). An iterative statistical approach to the identification of protein phosphorylation motifs from large-scale data sets. Nat Biotechnol *23*, 1391-1398.
31. Keshava Prasad, T.S., Goel, R., Kandasamy, K., Keerthikumar, S., Kumar, S., Mathivanan, S., Telikicherla, D., Raju, R., Shafreen, B., Venugopal, A., et al. (2009). Human Protein Reference Database--2009 update. Nucleic Acids Res *37*, D767-772.
32. Duarte, N.C., Becker, S.A., Jamshidi, N., Thiele, I., Mo, M.L., Vo, T.D., Srivas, R., and Palsson, B.O. (2007). Global reconstruction of the human metabolic network based on genomic and bibliomic data. Proc Natl Acad Sci U S A *104*, 1777-1782.
33. Cox, J., and Mann, M. (2012). 1D and 2D annotation enrichment: a statistical method integrating quantitative proteomics with complementary high-throughput data. BMC Bioinformatics *13 Suppl 16*, S12.
34. Nakatsu, M.N., and Hughes, C.C. (2008). An optimized three-dimensional in vitro model for the analysis of angiogenesis. Methods Enzymol *443*, 65-82.
35. Fiorio Pla, A., Ong, H.L., Cheng, K.T., Brossa, A., Bussolati, B., Lockwich, T., Paria, B., Munaron, L., and Ambudkar, I.S. (2012). TRPV4 mediates tumor-derived endothelial cell migration via arachidonic acid-activated actin remodeling. Oncogene *31*, 200-212.
36. Sun, Z., Li, X., Massena, S., Kutschera, S., Padhan, N., Gualandi, L., Sundvold-Gjerstad, V., Gustafsson, K., Choy, W.W., Zang, G., et al. (2012). VEGFR2 induces c-Src signaling and vascular permeability in vivo via the adaptor protein TSAd. J Exp Med *209*, 1363-1377.
37. Dejana, E., Tournier-Lasserve, E., and Weinstein, B.M. (2009). The control of vascular integrity by endothelial cell junctions: molecular basis and pathological implications. Dev Cell *16*, 209-221.
38. Kashiwagi, S., Tsukada, K., Xu, L., Miyazaki, J., Kozin, S.V., Tyrrell, J.A., Sessa, W.C., Gerweck, L.E., Jain, R.K., and Fukumura, D. (2008). Perivascular nitric oxide gradients normalize tumor vasculature. Nat Med *14*, 255-257.
39. Sato, T.N., Tozawa, Y., Deutsch, U., Wolburg-Buchholz, K., Fujiwara, Y., Gendron-Maguire, M., Gridley, T., Wolburg, H., Risau, W., and Qin, Y. (1995). Distinct roles of the receptor tyrosine kinases Tie-1 and Tie-2 in blood vessel formation. Nature *376*, 70-74.
40. Rupp, H., Zarain-Herzberg, A., and Maisch, B. (2002). The use of partial fatty acid oxidation inhibitors for metabolic therapy of angina pectoris and heart failure. Herz *27*, 621-636.
41. Olsen, J.V., Blagoev, B., Gnad, F., Macek, B., Kumar, C., Mortensen, P., and Mann, M. (2006). Global, in vivo, and site-specific phosphorylation dynamics in signaling networks. Cell *127*, 635-648.
42. Stahmann, N., Woods, A., Spengler, K., Heslegrave, A., Bauer, R., Krause, S., Viollet, B., Carling, D., and Heller, R. (2010). Activation of AMP-activated protein kinase by vascular endothelial growth factor mediates endothelial angiogenesis independently of nitric-oxide synthase. J Biol Chem *285*, 10638-10652.
43. Ha, J., Daniel, S., Broyles, S.S., and Kim, K.H. (1994). Critical phosphorylation sites for acetyl-CoA carboxylase activity. J Biol Chem *269*, 22162-22168.
44. Shinde, A.V., Motiani, R.K., Zhang, X., Abdullaev, I.F., Adam, A.P., Gonzalez-Cobos, J.C., Zhang, W., Matrougui, K., Vincent, P.A., and Trebak, M. (2013). STIM1 controls endothelial barrier function independently of Orai1 and Ca2+ entry. Sci Signal *6*, ra18.
45. Soboloff, J., Rothberg, B.S., Madesh, M., and Gill, D.L. (2012). STIM proteins: dynamic calcium signal transducers. Nat Rev Mol Cell Biol *13*, 549-565.
46. Tiruppathi, C., Minshall, R.D., Paria, B.C., Vogel, S.M., and Malik, A.B. (2002). Role of Ca2+ signaling in the regulation of endothelial permeability. Vascul Pharmacol *39*, 173-185.

47. Martin-Ramirez, J., Hofman, M., van den Biggelaar, M., Hebbel, R.P., and Voorberg, J. (2012). Establishment of outgrowth endothelial cells from peripheral blood. Nat Protoc *7*, 1709-1715.
48. Groschner, L.N., Waldeck-Weiermair, M., Malli, R., and Graier, W.F. (2012). Endothelial mitochondria--less respiration, more integration. Pflugers Arch *464*, 63-76.
49. Berridge, M.J., Bootman, M.D., and Roderick, H.L. (2003). Calcium signalling: dynamics, homeostasis and remodelling. Nat Rev Mol Cell Biol *4*, 517-529.
50. Rizzuto, R., De Stefani, D., Raffaello, A., and Mammucari, C. (2012). Mitochondria as sensors and regulators of calcium signalling. Nat Rev Mol Cell Biol *13*, 566-578.
51. Wood, P.G., and Gillespie, J.I. (1998). Evidence for mitochondrial Ca(2+)-induced Ca2+ release in permeabilised endothelial cells. Biochem Biophys Res Commun *246*, 543-548.
52. Stahmann, N., Woods, A., Carling, D., and Heller, R. (2006). Thrombin activates AMP-activated protein kinase in endothelial cells via a pathway involving Ca2+/calmodulin-dependent protein kinase kinase beta. Mol Cell Biol *26*, 5933-5945.

Acknowledgements

We thank the BAIR facility at the Beatson, the nurses at the Southern General Hospital in Glasgow for the collection of the umbilical cords and Guido Serini for critically reading the manuscript. This work was supported by Cancer Research UK.

Figure legends

Figure 1. ECs remodel their metabolism when assembled into a fully formed vascular network.

(**A**) Workflow showing the model used to study EC morphogenesis, and how high-resolution proteomics has been integrated into the genome scale metabolic model using integrative metabolic analysis tool (iMAT). (**B**) HUVECs decrease proliferation when grown for 24h on matrigel compared to 3h, assessed by EdU incorporation (= % of cells in S phase of the cell cycle). (**C**) Logarithmized LFQ intensity ratio (22h/4h) measured for the cell-cell junction proteins ve-cadherin (CDH5) and plakoglobin (JUP), the tyrosine kinase receptor TIE1, and the endothelial nitric oxide synthase (NOS3), which were found more abundant in HUVECs cultured on matrigel for 22h compared to 4h. Bars represent mean of the LFQ intensity ratio ± SD ($n \geq 3$) as reported in Table S1. (**D**) Predicted flux changes upon morphogenesis for fatty acid oxidation (FAO) and glycolysis reactions. X axis = enzymes that catalyze the reaction. HK = hexokinase; PFK = phosphofructokinase; ALDO = aldolase; LDH = lactate dehydrogenase; PDH = pyruvate dehydrogenase; CPT = carnitine O-palmitoyltransferase; ACADM/S = medium(M)/short(S)-chain specific acyl-CoA

dehydrogenase, mitochondrial; Diff = diffusion octanoyl-CoA. (**E**) Schematic representation of cell metabolism with highlighted the pathways in (D). OxPhos = oxidative phosphorylation. In brackets = reaction ID as in Table S2. (**F**,**G**) Tracing experiment where ECs were cultured for 3h or 22h on matrigel followed by spike-in of $^{13}C_6$-labeled palmitate (F) or $^{13}C_{16}$ glucose (G) and 6h culture. Labeled (%) = % of labeled metabolite (peak area labeled) of the total amount (peak area labeled + peak area unlabeled). Peak area represents the amount of ^{13}C-labeled palmitoyl carnitine or lactate as measured by the mass spectrometer. For the palmitoyl carnitine the labeled (%) could not be measured because the unlabeled palmitoyl-carnitine was not detected by MS. For the lactate, peak area representation allows evaluating the extent of the glycolysis fuelled by extracellular ^{13}C-labeled glucose. Δ Peak area = Extracellular palmitate uptake, which was measured as amount of ^{13}C-labelled palmitate left in the medium at the end of the experiment minus the total amount of ^{13}C-labelled palmitate that was initially spiked-in. Bars = mean ± SD (n=3). (**H**) CPT1A levels (logarithmized LFQ intensity normalized by the average LFQ intensity measured at 4h) in HUVECs cultured on matrigel for 4h or 22h. Bars = Mean ± SD (n=6).

Figure 2. FAO regulates HUVEC functions.

(**A**,**B**) Reduced FAO upon etomoxir treatment (Eto, A) or CPT1A silencing with pool siRNA (siCPT1A, B) in HUVECs measured as ^{14}C-labelled acid soluble metabolites produced from ^{14}C-labeled palmitic acid. CCPM = corrected count per minute. CCPM is expressed as percentage compared to the vehicle-treated cells (Ctl = 100%); siCtl = non-targeting siRNA. (**C**,**D**) Cell proliferation upon etomoxir treatment for the indicated time (C) or CPT1A silencing (bars represent mean ± SD) (D), measured as percentage of cells incorporating EdU. EdU^+ cells are expressed as percentage compared to the control cells (Ctl = 100%). (**E**,**F**) Propidium Iodide (PI) and annexin V (AV) staining of cells grown in the presence of etomoxir for 24h (E) or silenced for CPT1A (F) was measured by FACS. Starv = cells starved overnight in EBM-2. (**G**,**H**) Reduced integrity of the network formed by cells after 24h culture on matrigel in the presence of etomoxir (G) or when silenced for CPT1A (H). (**I**,**J**) Reduced sprouting in 3D-fibrin angiogenesis assay (48h) performed with cells in the presence of etomoxir (I) or silenced for CPT1A (J). P-value according to Mann-Whitney test (n>20 cell-coated beads).

Figure 3. FAO fuels the TCA cycle to generate energy.

(**A**) Decreased total cellular ATP levels induced by 3h etomoxir treatment raised upon pyruvate and DCA treatment, as measured by luciferase activity. Luciferase activity is expressed as percentage compared to the control (Ctl = 100%); bars represent mean ± SEM (n=9). P-value according to Mann-Whitney test. P = pyruvate; DCA = dichloroacetate. (**B**) Decreased phosphorylation levels of Ser293 and Ser300 (when phosphorylated by the pyruvate dehydrogenase kinase, PDHA1 activity is inhibited), as measured by MS in the SILAC phosphoproteomic analysis of HUVECs treated with etomoxir (Table S3). The SILAC ratio was calculated between cells treated with etomoxir and vehicle-treated cells (Ctl). A-C represents three replicate experiments. (**C**) Seahorse measurements of oxygen consumprion rate (OCR) show that etomoxir induces decrease OCR compared to control (Ctl) cells. Replenishment of the TCAc with pyruvate and DCA increases OCR in both, Ctl and etomoxir-treated cells. Arrows indicate the measurements represented in panel (D). Oligo = oligomycin 1µM. Bars represent mean ± SEM (n=20). (**D**) Quantifcation of (C). Bars represent mean ± SEM (n=20). P-value according to Mann-Whitney test.

Figure 4. Phosphoproteomics reveals altered Ca^{2+} signaling upon acute inhibition of CPT1A with etomoxir.

(**A**) Workflow of the SILAC proteomic and phosphoproteomic analysis of HUVECs treated with vehicle (Ctl), etomoxir (Eto) or etomoxir followed by pyruvate (P) and dichloroacetate (DCA) treatment (Eto-P-DCA). Results refer to three SILAC experiments, Exp 1-3, where the SILAC labeling conditions were swapped. (**B**) Predicted active kinases upon etomoxir treatment (NetwroKIN analysis). Numbers in brackets indicate the number of predicted substrates shown in Table S6. (**C**) Linear motifs identified by Motif-X analysis. (**D**) Etomoxir-upregulated phosphorylation sites on proteins involved in Ca^{2+} signaling (literature-based). Bars represent mean ± SD (n≥2).

Figure 5. Acute CPT1A inhibition induces increased Ca^{2+} oscillation freaquency.

(**A**) Representative plot of increased Ca^{2+} oscillation frequency in HUVECs upon etomoxir treatment. Each line represents a single cell. (**B**) Increased frequency of Ca^{2+} oscillations in HUVECs upon etomoxir treatment is restored in the presence of pyruvate and DCA or 100µM gadolinium (Gd^{3+}). (**C**) Representative plot of increased Ca^{2+} oscillation frequency in HUVECs upon oxfenicine treatment. Each line represents a

single cell. (**D**) Increased frequency of Ca^{2+} oscillations in HUVECs upon oxfenicine treatment is restored in the presence of pyruvate and DCA. Bars represent mean ± SEM (n>150). P-value according to Mann-Whitney test.

Figure 6. Acute CPT1A inhibition induces EC hyperpermeability.

(**A**) Decreased trans-endothelial resistance (TEER) (= increased EC permeability) in HUVECs induced by etomoxir is inhibited blocking Ca^{2+} entry pre-treating cells (10 min) with 100µM gadolinium (Gd^{3+}). (**B,C**) Decreased TEER in HUVECs (B) and BOECs (C), induced by etomoxir raises upon pyruvate (P) and dichloroacetate (DCA) treatment. (**D**) Decreased TEER in HUVECs treated with oxfenicine raised upon P and DCA treatment. (**E**) Oligomycin treatment (1µM) decreases TEER in HUVECs and abrogates the effects of P and DCA treatment in etomoxir-treated cells. Bars represent mean ± SEM (n=3).

Figure 7. Acute CPT1A inhibition increases blood vessel leakage.

(**A,B**) Quantification of Evans blue extravasation from the vasculature of the mouse ear following acute etomoxir (A) and oxfenicine (B) treatment at the indicated doses. The permeability was measured as amount of leaked blue/constant area (μm^2). (**C**) Quantification of Evans blue extravasation in (D), (E) and (F). (**D-F**) Representative images showing Evans blue extravasation from the mouse ear vasculature upon acute etomoxir treatment (5 µg) (D), which is inhibited in the presence of pyruvate and DCA (Eto-P-DCA) (E) and gadolinium (Gd^{3+}) (F). (**G**) Schematic overview of FAO function in ECs. Blue arrow indicates that the finding is supported by experiments; red dashed arrow indicates that the mechanisms have still to be determined (hypotheses are discussed in the Discussion). Bars represent mean ± SEM (n≥3).

Patella et al. Figure 1

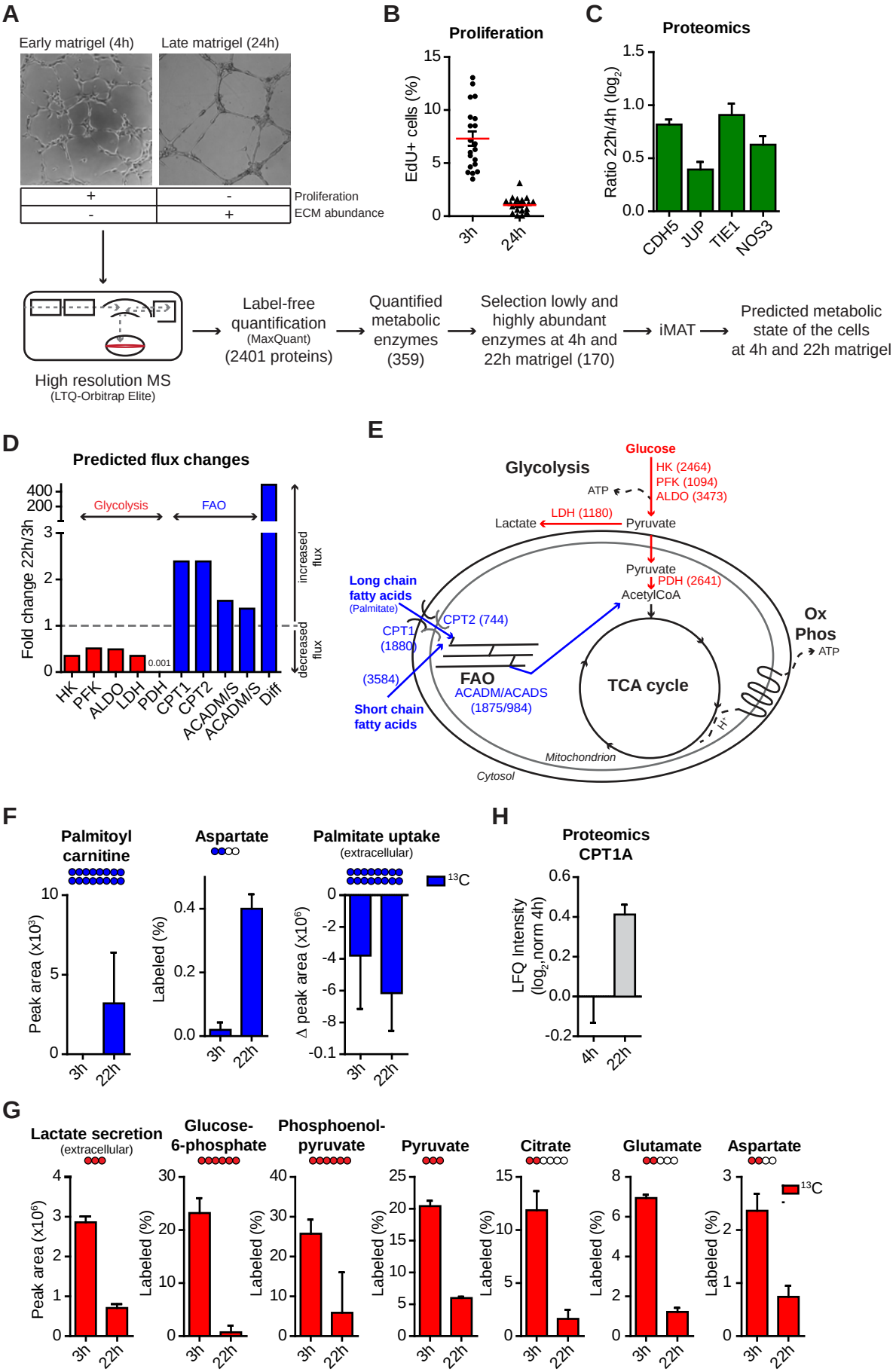

Patella et al. Figure 2

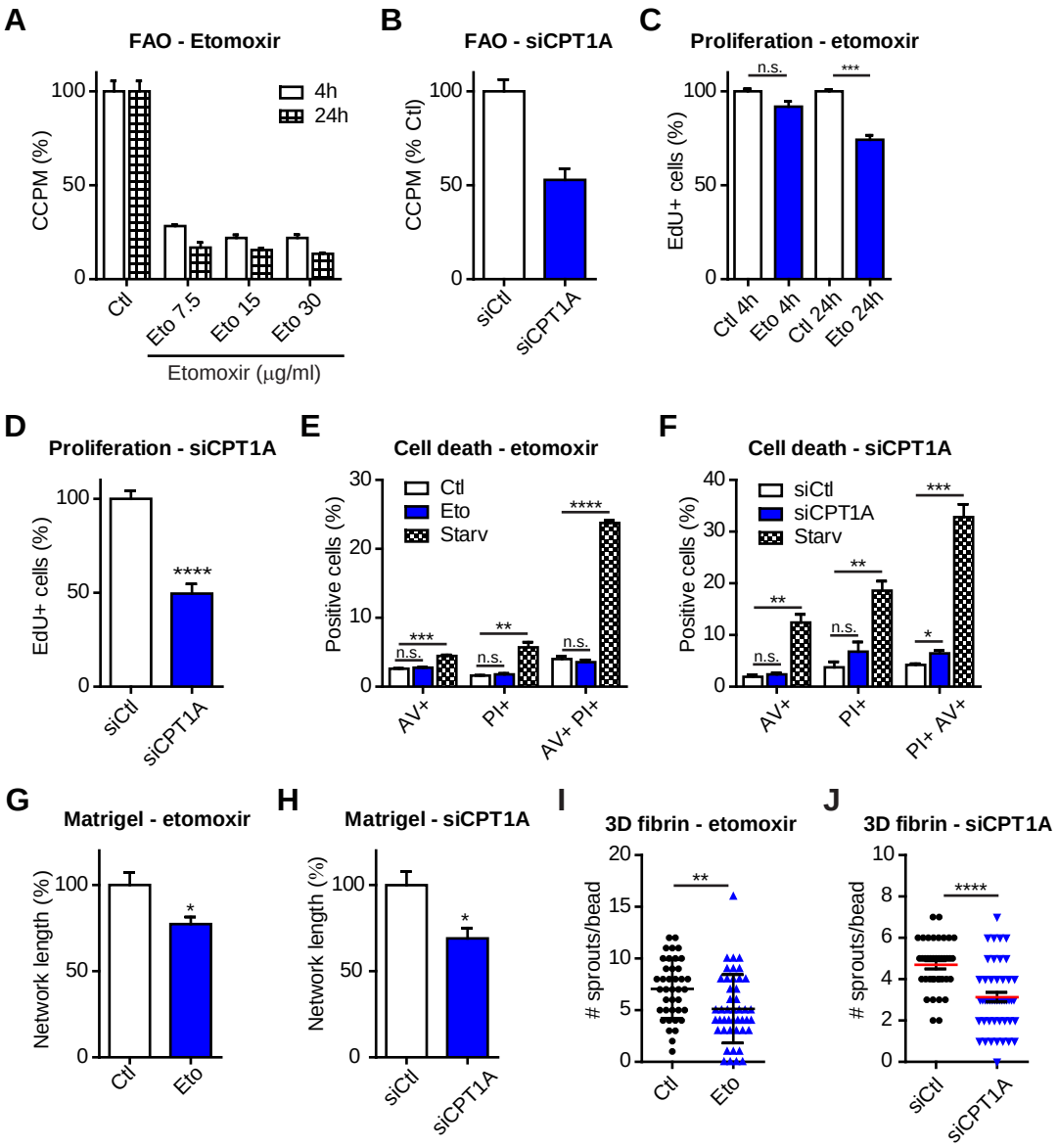

Patella et al. Figure 3

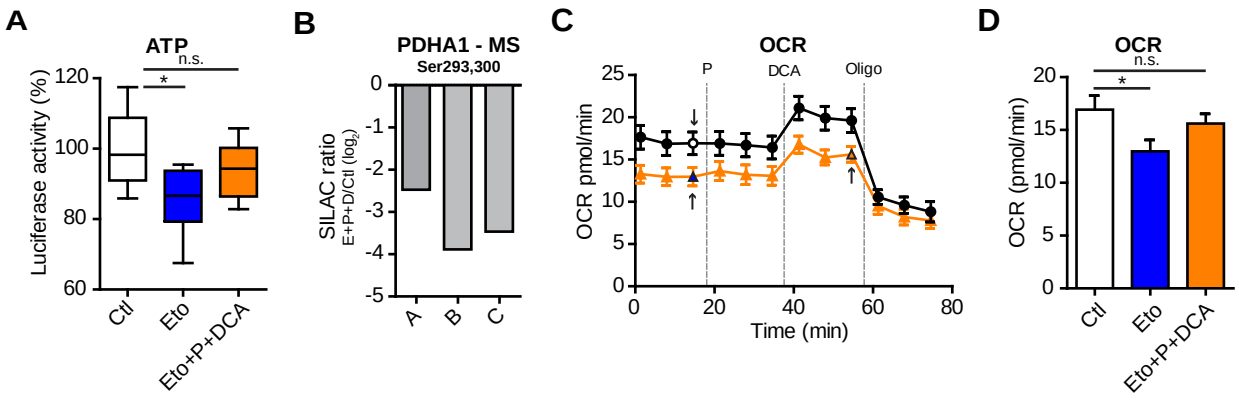

Patella et al. Figure 4

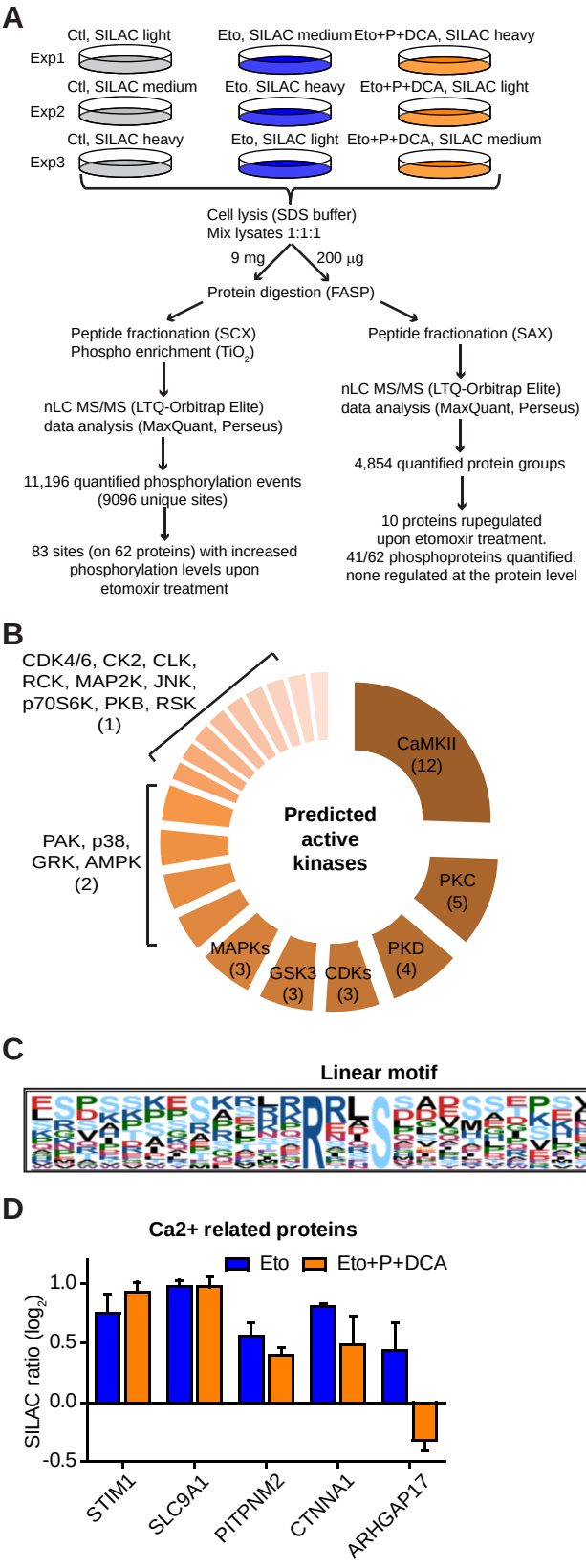

Patella et al. Figure 5

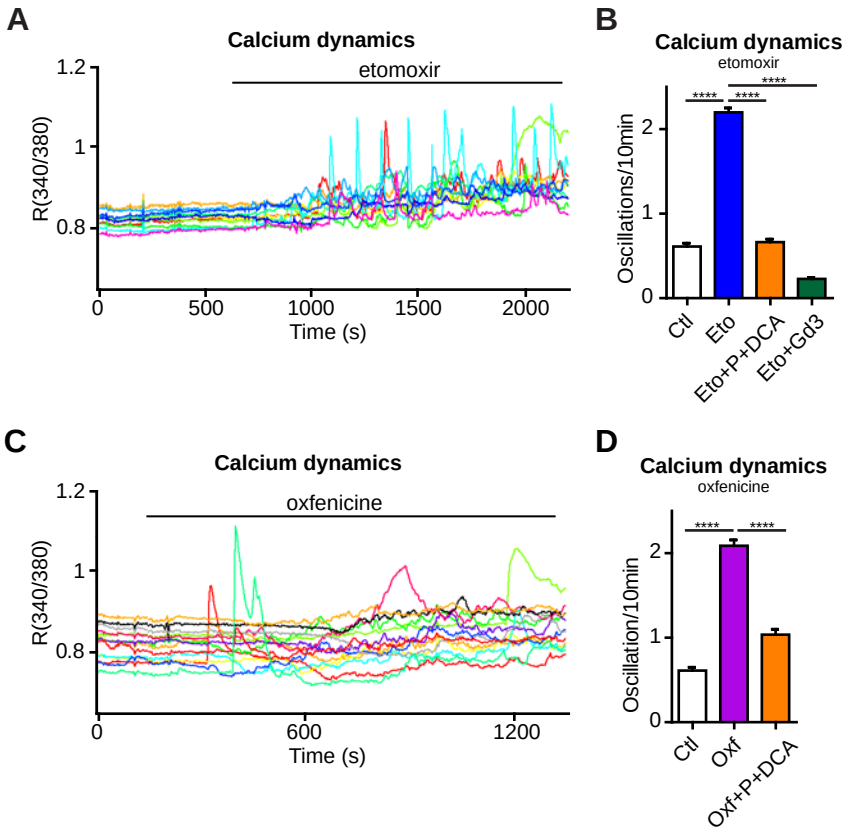

Patella et al. Figure 6

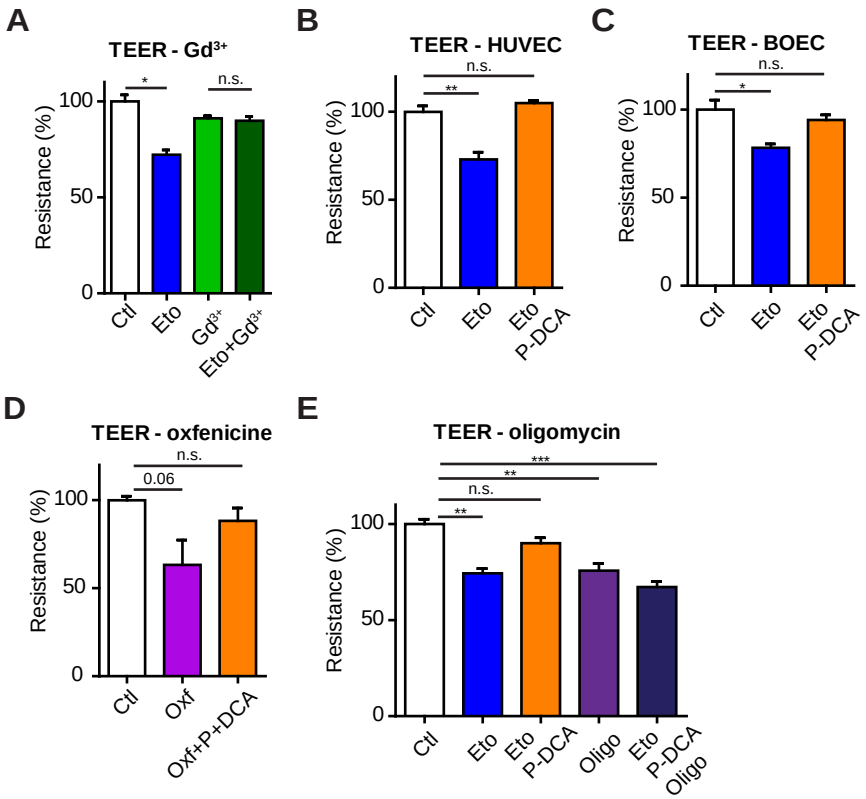

Patella et al. Figure 7

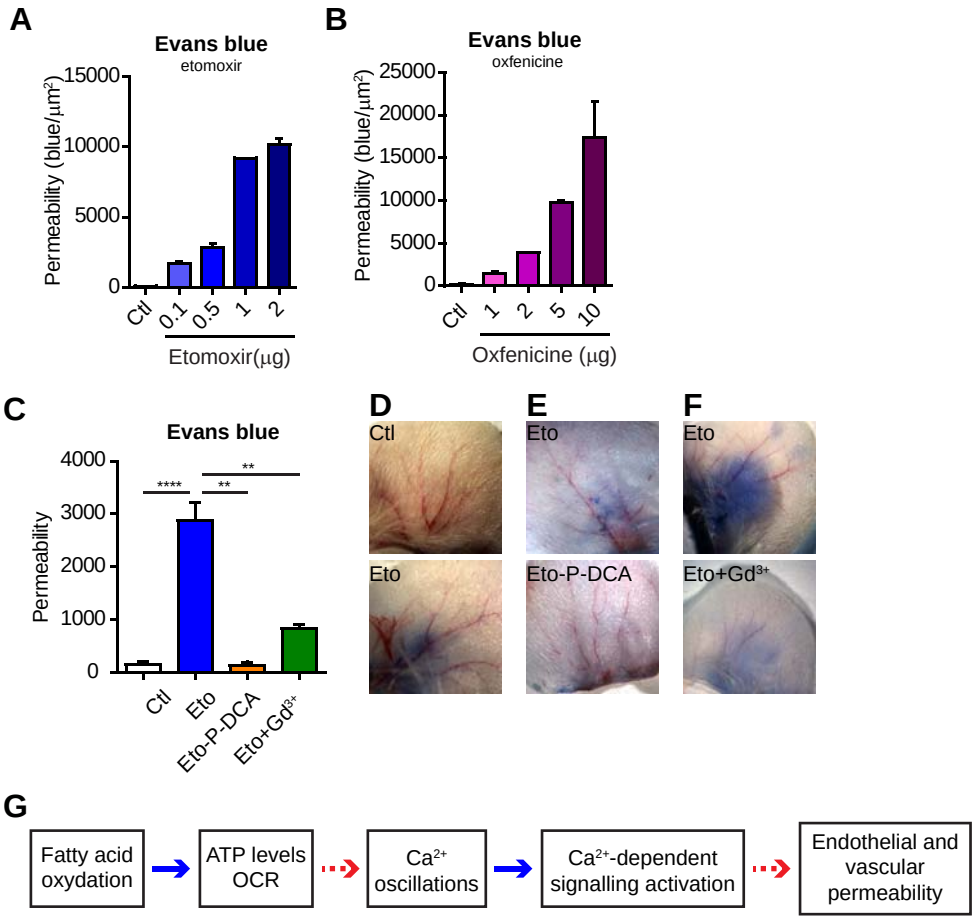

Supplemental Figures and Tables

Table S1. LFQ-based proteome quantification of HUVECs cultured on matrigel for 4h and 22h.

Table S2. Metabolic reactions flux predicted by iMAT after integration of the proteomic data (HUVECs on matrigel for 4h and 22h, Table S1) into GSMM and upon inactivation of CPT1A integrating proteomic data of HUVECs upon morphogenesis (Matrigel 22h, Table S1) into GSMM.

22h vs 4h matrigel: Full list of reactions in the GSMM showing: reaction index (ID) (column A), the metabolic pathway which the reaction belongs to (column B), reaction name (column C), reaction stoichiometric formula (column D), predicted fluxes following ACHR sampling (column E for 4h, and column F for 22h), fold-change between 22h and 4h (column G), and the gene-reaction rules (column H) where genes are indicated by their Entrez ID.

CPT1A inactivation: The full list of reactions in the GSMM is provided. Columns A-D are as above. The predicted average fluxes when CPT1A associated reactions are forced to be active (at their maximal flux as estimated by flux-variability analysis) are given in columns E and when they are inhibited (zero flux) are given in columns F. The fold-changes (flux when CPT1A is inhibited/flux when CPT1A is active) are shown in column G.

Table S3. SILAC phosphoproteome of HUVECs acutely treated with etomoxir and when TCA cycle is replenished with pyruvate and DCA. The table reports the class I phosphorylation sites (with localization probability > 0.75 and score difference > 5) and predicted kinase activity (based on kinase motifs reported in the HPRD database) upon etomoxir treatment.

Phosphoproteome: contains the relative quantification (SILAC ratio) of each phosphorylation sites whether it was quantified in singly, doubly or multiply phosphorylated peptides. This quantitative information is indicated in the "Multiplicity" column as _1, _2, _3 respectively.

Eto up-regulated sites: contains the 83 phosphosites with increased phosphorylation levels upon etomoxir treatment.

M = SILAC medium-labeled; L = SILAC light-labeled; H = SILAC heavy-labeled.

A-C = three replicate experiments.

Table S4. Annotated MS/MS spectra of the phosphorylation sites upregulated upon etomoxir treatment.

Annotated spectra as reported in the Viewer module of MaxQuant.

Table S5. SILAC proteome of HUVECs acutely treated with etomoxir and when TCA cycle is replenished with pyruvate and DCA.

SILAC-based relative quantification of identified protein groups in triplicate experiments. Ratios are reported as $\log_2$ values.

Table S6. NetworKIN output

Figure S1. HUVECs increase FAO when assembled into a fully formed network.

(**A**) Three time point results of tracing experiment where ECs were grown for 3h, 22h (results as in Figure 1) or 30h on matrigel followed by spike-in of $^{13}C_{16}$-labelled palmitate followed by additional 6h in culture. Y axis = Labeled (%) = % of labeled metabolite of the total amount (labeled + unlabeled). Δ Peak area = palmitate uptake based on the quantification of the extracellular palmitate. Tracing experiment was performed also at 30h to increase the robustness of the data obtained at 22h. Indeed, due to the low flux rate of FAO in ECs, only few labeled-metabolites could be measured by MS. (**B**) Measured FAO, by means of $^{14}CO_2$ produced from ^{14}C-labeled palmitic acid, in HUVECs grown on gelatin-coated dish for 4h and 22h. CCPM = corrected count per minute. CCPM is expressed as percentage compared to the 4h adhesion cells (4h = 100%). Bars represent mean +/- SEM (n=5). (**C**) Proliferation of HUVECs grown on culture dish for 24h or 8 days (8d) at confluence (medium was changed every second day). Percentage of cells incorporating EdU during 2h was measured. EdU^+ cells are expressed as percentage compared to the control cells (Ctl = 100%). (**D**) Measured FAO, by means of $^{14}CO_2$ produced from ^{14}C-labeled palmitic acid, in HUVECs grown on culture dish for 24h or 8 days (8d) at confluence. CCPM is expressed as percentage compared to cells grown for 24h (24h = 100%). Bars = Mean +/- SEM (n=4).

Figure S2. Effects of CPT1A inhibition in HUVECs.

(**A**) Efficiency of CPT1A silencing (72h after transfection) in HUVECs transfected with a pool of siRNA specific for CPT1A (siCPT1A). Bars represent the mean of five experiments (including those used to measure the FAO in Figure 2A) +/- SD. The efficiency is measured as % of remaining protein compared to cells transfected with a non-targeting siRNAs (siCtl = 100%) as measured by western blot and quantified using Licor software. On the right a representative western blot. Vinculin was used as loading control. (**B-D**) Western blot which shows the efficient silencing of CPT1A (48h after transfection) compared to siCtl, using two independent siRNA (#1 and #2) or a pool of siRNA. Cells silenced with the siRNA were used for the EdU incorporation experiment in Figure 2D (B), cell death analysis in Figure 2F (C), and matrigel assay in panel (E,F) and Figure 2G and TEER in Figure S4E (D). β-tubulin and vinculin were used as loading control. (**E**) Representative bright field images which show the reduced integrity of the HUVEC network formed in the presence of etomoxir or when silenced for CPT1A compared to their respective controls. (**F**) Reduced network length measured when HUVECs were cultured on matrigel for 24h in the presence of etomoxir or when silenced for CPT1A compared to their respective controls. The network length is expressed as percentage compared to the siCtl cells (siCtl = 100%). P-values according to two-tailed paired t-test (n>3). (**G**) HUVEC proliferation upon mitomycin C treatment at the indicated concentrations (bars represent single measurement) measured by means of 2h EdU incorporation. (**H**) Reduced integrity of the network formed by HUVECs after 24h culture on matrigel in the presence of etomoxir. The network was not disrupted in the presence of mitomycin C. (**I**) Western blot which shows the efficient silencing of CPT1A (48h after transfection), compared to siCtl, using two independent siRNA (#1 and #2) or a pool of siRNA. Silenced cells were used for the three dimension (3D)-fibrin assay in panel (J) and Figure 2J. β-tubulin was used as loading control. (**J**) Reduced number of sprouting HUVECs during 3D-fibrin angiogenesis assay performed with HUVECs transfected with siCtl or two independent siRNA for siCPT1A. The number of sprouts was measured after two days culture in fibrin gel. P-value according to Mann-Whitney test (n>20 cell-coated beads). (**K**) Oxfenicine treatment for 7h at the indicated concentrations reduces FAO in HUVECs, measured as ^{14}C-labelled acid soluble metabolites produced from ^{14}C-labeled palmitic acid. CCPM = corrected count per minute. Ctl = vehicle-treated cells. CCPM is expressed as percentage compared to the vehicle-treated cells (Ctl = 100%). Bars = Mean +/- SEM (n=6). (**L**) Decreased total cellular ATP levels induced by 3h treatment with oxfenicine at the indicated concentrations, measured by luciferase activity. Luciferase activity

is expressed as percentage compared to the vehicle-treated cells (Ctl = 100%). Whiskers plot, min to max. P-value according to Mann-Whitney test (n≥10). (**M**) Decreased oxygen consumption rate (OCR) induced by 3h treatment with 2.5mM oxfenicine (Oxf). Bars = Mean +/- SEM. P-value according to Mann-Whitney test (n>100).

Figure S3. Etomoxir induces phosphorylation of the AMPK substrate ACACA

(**A**) Kinases predicted to be active upon etomoxir treatment, based on kinase motif enrichment analysis done with Perseus (Fisher exact test, 2% FDR). (**B**) Increased phosphorylation levels of Ser80 of the acetyl-CoA carboxylase (ACACA) induced by etomoxir (Eto), and pyruvate (P) and dichloroacetate (DCA) treatments, as measured by MS in the SILAC phosphoproteomic analysis of HUVECs treated with etomoxir (Table S3). The SILAC ratio was calculated between cells treated with the indicated drug and vehicle-treated cells (Ctl). (**C**) Three dimensional (3D) visualization of a representative MS spectrum of SILAC triplet used for the quantification of the phosphorylated Ser80 of ACACA in HUVECs treated with the indicated stimuli. (**D**) Annotated MS/MS spectrum (from the Viewer module of MaxQuant) obtained from the fragmentation of the peptide shown in (C). (**E**) Western blot showing that increased levels of ACACA phosphorylation at Ser80 upon etomoxir treatment are reduced when cells are treated with 10µM Gd^{3+}. Vinculin was used as loading control. The panel at the bottom shows the quantification of the western blot using Licor software.

Figure S4. Effects of CPT1A inhibition on Ca^{2+} oscillation frequency and TEER.

(**A**) Increased Ca^{2+} oscillations in HUVECs upon etomoxir treatment are inhibited when cells are pre-treated with Gd^{3+}, which blocks extracellular Ca^{2+} entry. Each line represents a single cell. (**B**) Western blot which shows the efficient silencing of CPT1A (48h after transfection), compared to siCtl, using two independent siRNA (#1 and #2) or a pool of siRNA. Actin was used as loading control. Cells were used for the experiment in (C). (**C**) Calcium oscillations measured in HUVECs siCtl or siCPT1A treated or not with etomoxir. Bars show mean +/ SEM (n>100 cells). (**D, E**) Decreased trans-endothelial resistance (TEER) (= increased EC permeability) in HUVECs induced by 24h treatment with etomoxir (D) or silencing CPT1A (72h after transfection) (E). Bars represent mean ± SEM (n=3). (**F, G**) Decreased TEER in HUVECs treated

for 15min with 1 unit/ml of thrombin (F) or with 1nM $VEGF_{165}$ for the indicate time (G). Bars represent mean ± SEM (n=3).

Figure S5. Effects of CPT1A inhibition on blood vessel leakage in-vivo.

(**A,B**) Representative images (see Figure 7 A,B) showing dose-dependent Evans blue extravasation from the vasculature of the mouse ear following acute etomoxir (A)and oxfenicine (B) treatment. (**C**) Representative images showing Evans blue extravasation from the vasculature of the mouse ear injected with gadolinium (Gd^{3+}) only or with etomoxir in the presence or absence of Gd^{3+}. (**D**) Quantification of (C). The permeability was measured as amount of leaked blue/constant area (μm^2). For Figure 7, the permeability measured for the gadolinium treatment only (average of 4 mice) was subtracted to the permeability measured upon treatment with etomoxir + gadolinium. Bars represent mean +/- SEM (n=3). P-values according to two-tailed unpaired t-test.

Patella et al. Figure S5

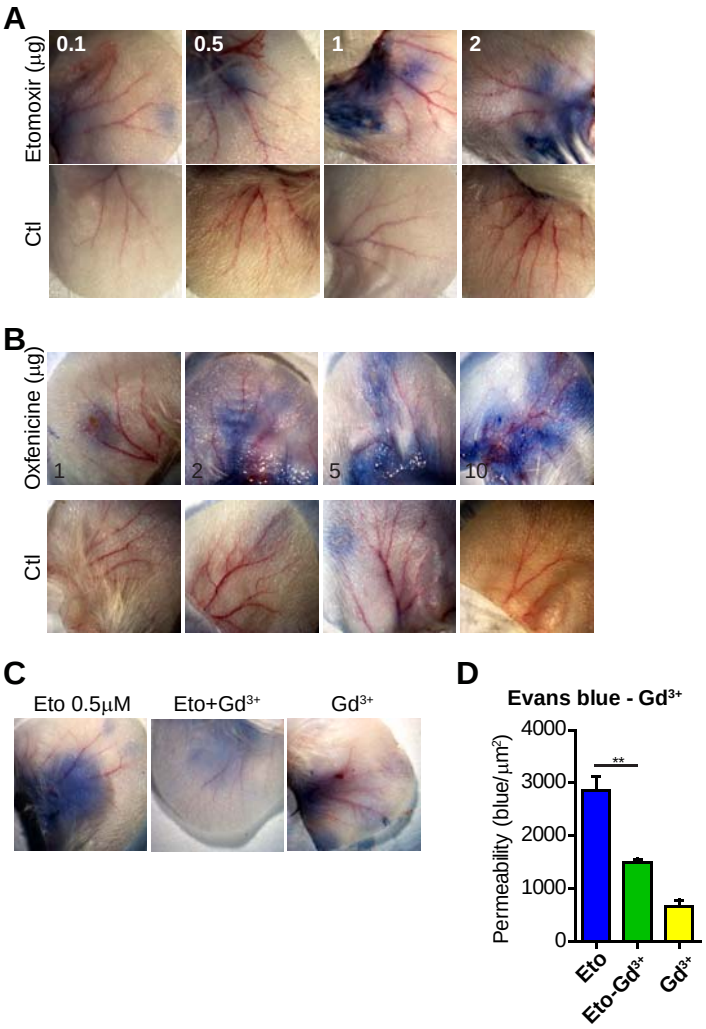

Patella et al. Figure S4

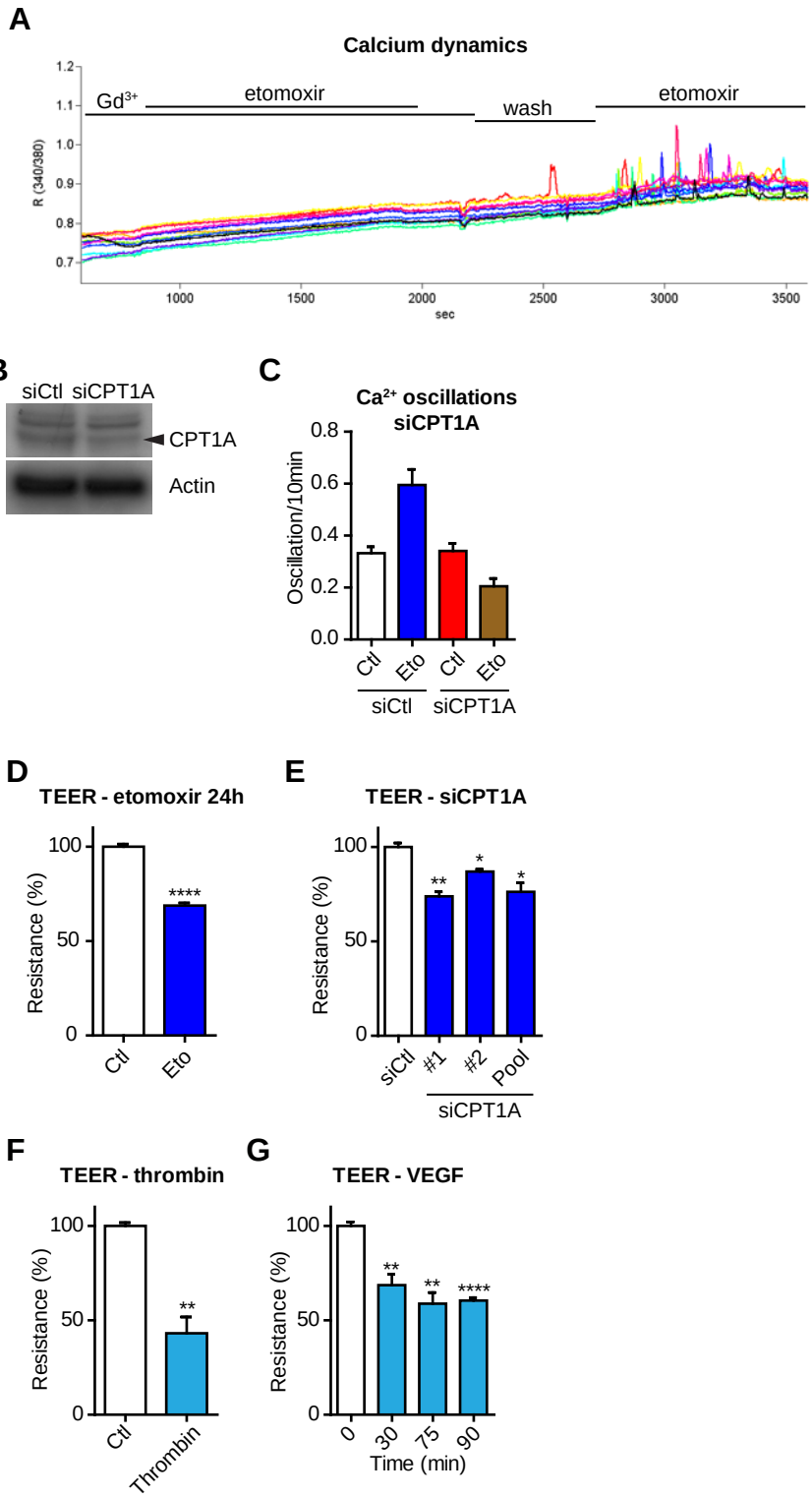

Patella et al. Figure S3

A

Predicted active kinases

Kinase motif	Enrichment score	Predicted substrates
AMP-activated protein kinase	4.4798	9
PKC epsilon kinase	3.2534	13
PAK2 kinase	3.1677	12
Calmodulin-dependent protein kinase II	1.7718	30

B

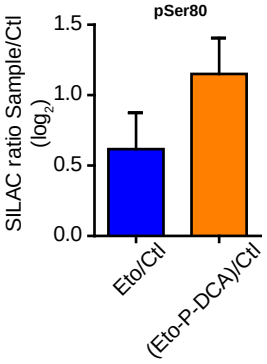

C

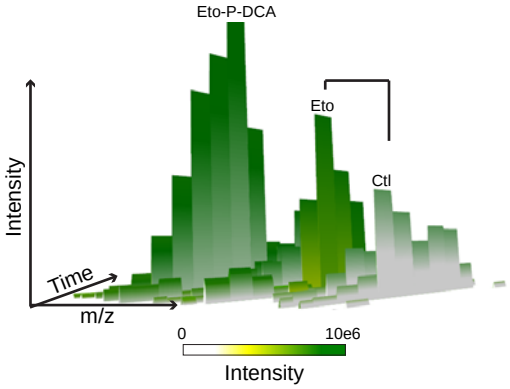

D

MS/MS annotated spectra for phosphorylated Ser80 of ACACA

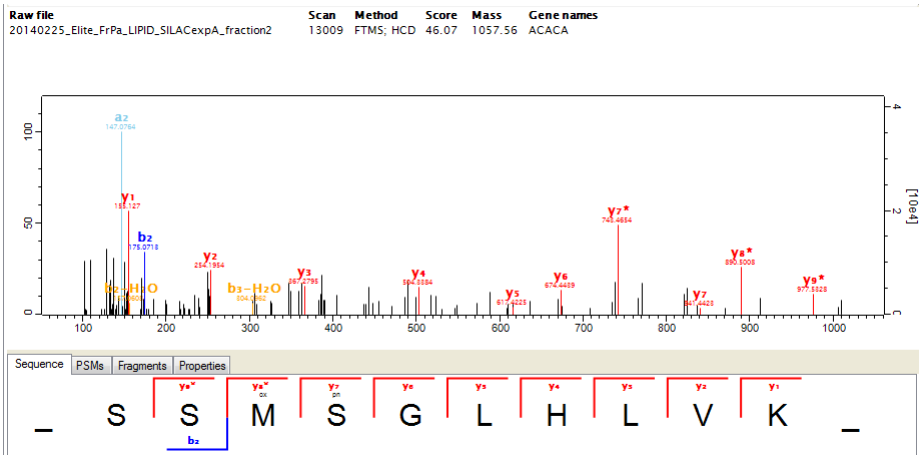

E

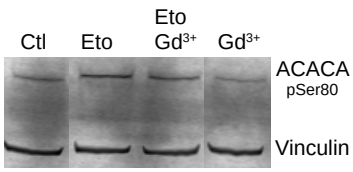

WB quantification

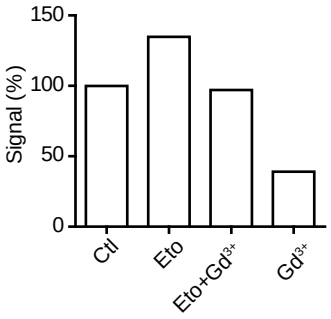

Patella et al. Figure S2

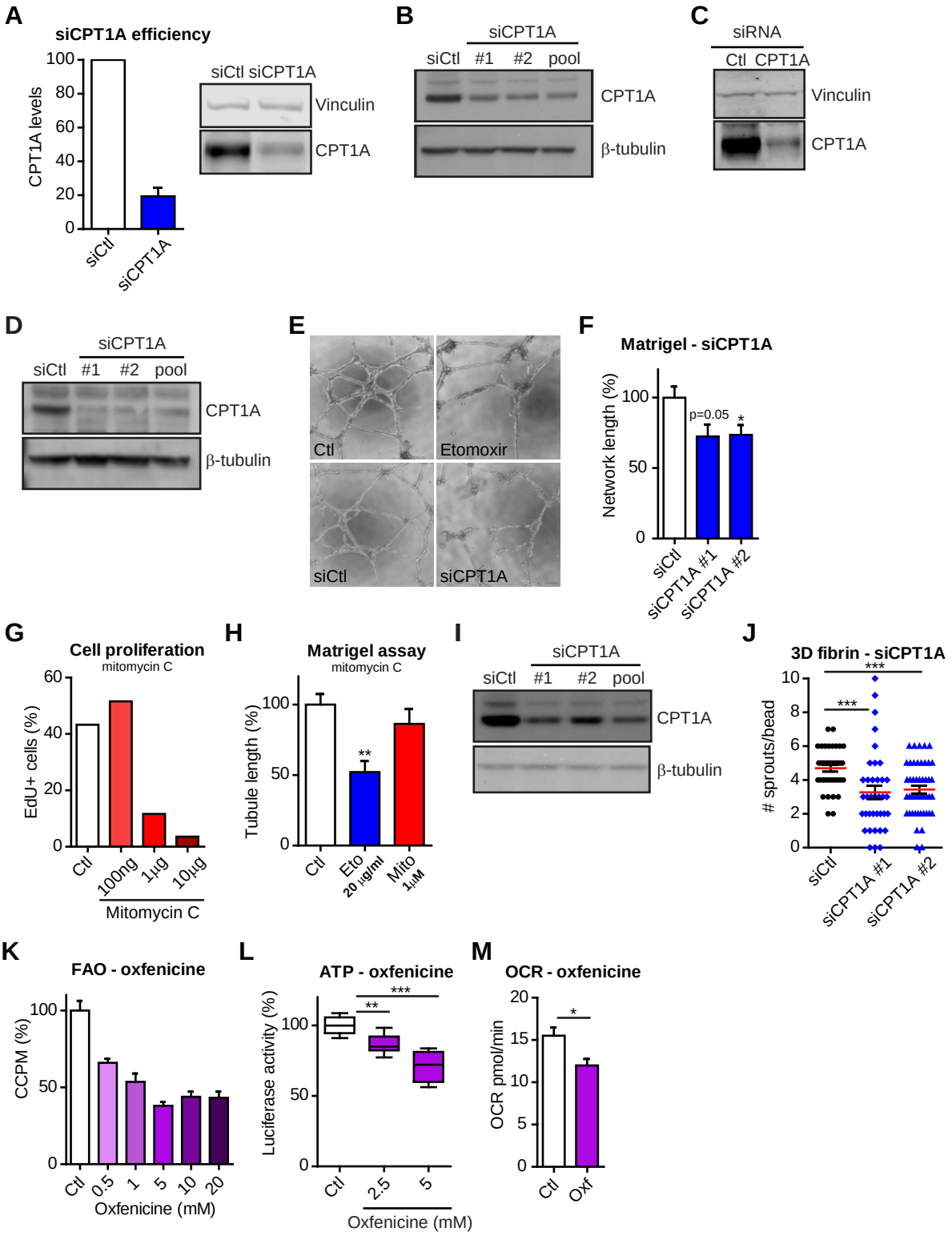

Patella et al. Figure S1